E.O. Paton Electric Welding Institute of the National Academy of Sciences of Ukraine

International Scientific-Technical and Production Journal

The Paton WELDING JOURNAL

Issue
09
2020

Published Monthly Since 2000

English Translation of the Monthly «Avtomatychne Zvaryuvannya»
(Avtomaticheskaya Svarka/Automatic Welding) Journal Published in Ukrainian and Russian Since 1948

Founders
E.O. Paton Electric Welding Institute
International Association «Welding»
Publisher
International Association «Welding»
Translators
A.O. Fomin, I.M. Kutianova
Editor
N.G. Khomenko
Electron galley
D.I. Sereda, T.Yu. Snegiryova
Address
E.O. Paton Electric Welding Institute,
International Association «Welding»
11 Kazymyr Malevych Str. (former Bozhenko),
03150, Kyiv, Ukraine
Tel.:/Fax: (38044) 200 82 77
E-mail: journal@paton.kiev.ua
www://patonpublishinghouse.com/eng/journals/tpwj

State Registration Certificate
KV 4790 of 09.01.2001
ISSN 0957-798X
DOI: http://dx.doi.org/10.37434/tpwj
Subscriptions
12 issues per year, back issues available.
$384, subscriptions for the printed (hard copy) version,
air postage and packaging included.
$312, subscriptions for the electronic version
(sending issues of Journal in pdf format
or providing access to IP addresses).
Institutions with current subscriptions on printed version
can purchase online access to the electronic versions
of any back issues that they have not subscribed to.
Issues of the Journal (more than two years old)
are available at a substantially reduced price.

CONTENTS

SCIENTIFIC AND TECHNICAL

INDUSTRIAL

In Memory of Borys Evgenovych Paton

National Academy of Sciences of Ukraine, and the E.O. Paton Electric Welding Institute with deep sorrow inform that on August 19, 2020 the world and Ukrainian science suffered a great loss: the heart of academician Borys Evgenovych Paton stopped in 102nd year of his life. A prominent Ukrainian scientist in the field of metallurgy, technology of metals, electric welding and materials science, organizer of science, state and public figure, B.E. Paton was President of the National Academy of Sciences of Ukraine, Director of the E.O. Paton Electric Welding Institute of the NAS of Ukraine, twice hero of Socialist Labour, first Hero of Ukraine.

B.E. Paton was born on November 27, 1918 in Kiev in the family of Evgen Oscarovych Paton, Professor of the Kiev Polytechnic Institute.

His engineering and scientific activity began in 1942 at the Electric Welding Institute, which then was stationed in the territory of «Uralvagonzavod» in Nyzhny Tahil during the evacuation period. Since that time B.E. Paton worked for 11 years together with his father, who was head of the Institute. These were the years of his formation as a scientist and researcher, and later leader of a large science-production team. He carried on and brilliantly developed the activity started by E.O. Paton, together with whom he created the world-renowned Paton scientific school, and for 67 years he headed the science and technology complex widely known all over the world — the E.O. Paton Electric Welding Institute of the NAS of Ukraine.

B.E. Paton received world-wide recognition due to his multifaceted and extremely fruitful scientific and engineering activity, his desire to focus fundamental scientific research on solving actual problems of progress of science and technology. By his works he laid a foundation for arc welding, in particular theory of automatic machines for arc welding, which was then developed by many specialists in the field of automatic control of welding processes.

B.E. Paton headed research in the field of welding power sources, development of the processes of arc, electroslag, flash-butt, electron beam and many other kinds of welding and related technologies; performance of a large package of fundamental and applied studies in the field of static and cyclic strength of welded joints, their brittle and fatigue fracture resistance, and low-temperature performance. Systems of diagnostics of welded structures, of which higher safe operation requirements are made, were introduced for the first time in Ukraine. B.E. Paton led the research on application of the electroslag process to improve the quality of metals and alloys, resulting in formation of a fundamentally new field of metallurgy — electroslag remelting and casting. Technologies developed under his leadership, are successfully used on the ground, under the water and in space. B.E. Paton also proposed applying the welding methods for joining live tissues.

For many years B.E. Paton as editor-in-chief, supervised publication of leading journals in the field of welding and related technologies — «Avtomatychne Zvaryuvannya», «Suchasna Elektrometalurhiya» and «Tekhnichna Diahnostyka ta Neruinivnyi Kontrol» that allowed sharing with the world scientific-technical community the information on research results and new developments of the Electric Welding Institute, promoting realization of more than 150 licenses in foreign countries.

In 1962 B.E. Paton was elected President of the Academy of Sciences of Ukr.SSR (now — National Academy of Sciences of Ukraine). Deep understanding of the role of science in society, its goals and objectives, high international authority of the scientist, his devotion to science, inexhaustible energy and high moral qualities, intense social-political activity, experience of leading large scientific teams became the decisive arguments in B.E. Paton's election to this position. Since that time he headed this leading scientific organization of Ukraine for 58 years.

In the responsible position of President of the NAS of Ukraine his talent of organizer of science was revealed even more. B.E. Paton was involved in development of a new structure of the Academy of Sciences, its new Statute, aimed at the most rational use of scientific staff and means, focusing their efforts on solution of the most important fundamental and applied scientific problems that are important for the country's economy, founding dozens of new institutes and establishments that developed and deepened the studies in priority fields of science.

B.E. Paton's outstanding abilities as a leader, scientist and organizer were revealed during the dramatic days of the accident at Chornobyl NPP. The staff of many Institutes of the Academy, and its Presidium began working on liquidation of the consequences of this catastrophe from the very first days.

During the years of independence of Ukraine, B.E. Paton did a lot for preservation and enhancing of the potential of national science, deploying new scientific areas, required for building an independent European state, its economy, scientific-technical, educational, socio-cultural sectors, strengthening the country's defense.

B.E. Paton made a significant contribution into development of international scientific cooperation of Ukraine, incorporation of national science into the European and global scientific space. By his initiative an International Association of the Academies of Sciences (IAAS) was established in 1993 that united the national academies of 15 European and Asian countries. B.E. Paton was the permanent President of this Association for almost a quarter of a century.

B.E. Paton was elected several times to the higher bodies of state power of the Soviet Union and Ukraine. He was the head and member of many important committees and commissions. Occupying high positions B.E. Paton worked fruitfully with a deep feeling of personal responsibility before the state, the people and his own consciousness.

B.E. Paton continued working until the last days of his life. His life's path is an example of devotion to his favourite cause, science and Ukraine. All those who were fortunate to communicate with B.E. Paton, knew him as an extremely creative personality, wise, deeply honest and well-wishing person with fantastic energy, desire to work, keep analytical mind, kind humour and high humanism.

Scientist recognized all over the world, an example of researcher, outstanding organizer of science, true son of the Ukrainian people — the bright memory of Borys Evgenovych Paton will live forever in the hearts of all those who knew him and worked with him.

https://doi.org/10.37434/tpwj2020.09.01

NUMERICAL METHODOLOGY OF PREDICTION OF THE RELIABILITY AND RESIDUAL LIFE OF WELDED PIPELINE ELEMENTS WITH CORROSION-EROSION DEFECTS

O.S. Milenin, O.A. Velykoivanenko, G.O. Rozynka and **N.I. Pivtorak**
E.O. Paton Electric Welding Institute of the NAS of Ukraine
11 Kazymyr Malevych Str., 03150, Kyiv, Ukraine. E-mail: office@paton.kiev.ua

A set of procedures, mathematical models and tools for their finite-element realization were developed to solve typical practical tasks of expert analysis of the technological condition and residual safe operating life of welded elements of the main and technological pipelines with defects of corrosion-erosion metal loss detected during diagnostics. In order to lower the conservativeness of analysis, the interrelated processes of thermal deformation at assembly and repair welding, as well as initiation and propagation of subcritical damage of the defective structure material in the ductile mode in operation under complicated temperature-force conditions of external impact, were taken into account. Procedures of statistical analysis of fracture susceptibility of welded pipelines were developed on the base of Weibull and Monte-Carlo methods, and adequacy of the developed computational methods was confirmed. Peculiarities of the effect of welding on the reliability and serviceability of the main and technological pipelines with detected defects of corrosion-erosion metal loss were determined, in order to develop minimally conservative recommendations as to the possibility of safe operation of the pipelines. 18 Ref., 2 Tables, 12 Figures.

Keywords: pipeline, defect of corrosion-erosion metal loss, welded joint, limit state, reliability, fracture probability, ductile fracture

Determination of residual strength and serviceability of pipeline elements (PE) with detected defectiveness is a typical task in the complex of measures on analysis of the actual technical condition and ensuring reliable operation. In particular, for the main and technological pipelines in long-term service a typical phenomenon is accumulation of metal discontinuity defects, which lower their load-carrying capacity of the metal right up to emergency condition. The most wide-spread defects are surface thinning of the pipe wall. Their appearance is the result of structure interaction with the aggressive environment, or negative impact of the transported product. Assessment of admissibility of isolated defects of corrosion-erosion metal loss is regulated by a range of local and foreign normative documents, the generality of which requires significant conservatism. In particular, a typical engineering approach is an essential simplification or ignoring the features of the PE stress-strain state (SSS) in the area of assembly or repair welds in the case of presence of a wall thinning defect on its periphery. This is associated with the complexity of description of the processes of interaction of different types of stresses (residual and in the raiser zone) and appropriate development of subcritical fracture of pipe material, that, in its turn determines the limit state of the defective PE.

In order to determine the limit state of welded structural elements under complex external impact and to solve the related applied problems, one of the modern tendencies in the world research practice is development of methods of numerical finite element prediction of spatial multiphysical processes, which determine initiation and development of material fracture. For the above problem of expert analysis of the reliability of welded PE with local metal losses, a goal was set in this study to develop a complex methodology of numerical prediction of residual SSS in the area of assembly (repair) welding, modeling the simultaneous development of stresses, strains, subcritical damage and to define the respective criteria of the limit state and reliability parameters.

Depending on design conditions of a specific PE operation, it was necessary to take into account different factors of impact on fracture susceptibility of a structure. As regards pipelines with revealed 3D defects of corrosion-erosion metal loss, the main mechanism of subcritical material damage is considered to be the ductile mechanism, which consists in initiation and development of material porosity of certain volume concentration f at plastic flow of metal under

O.S. Milenin — https://orcid.org/0000-0002-9465-7710 the impact of external static or cyclic loading [1, 2]. Thus, numerical tracing of the stress-strain and damage state of a defective PE should take into account the features of external operational impact on the pipe material, in particular, on the kinetics of irreversible deformations that cause initiation and propagation of ductile fracture pores.

At determination of residual SSS in the area of assembly permanent joints, it is necessary to take into account both the impact of welding process parameters proper, and temperature dependencies of the main properties of the pipe material. For this purpose, numerical prediction of temperature field kinetics was performed in this study by solving a nonstationary equation of heat conduction. The thus obtained development of spatially distributed temperatures and the change of structural composition determine formation and subsequent redistribution of stresses and strains in structures that, in its turn, determines the features of limit state under operation conditions.

Modeling of the kinetics of SSS and subcritical damage was conducted within the finite-element definition of the boundary problem of nonstationary thermoplasticity and ductile fracture. So, the increment of deformation tensor in a specific finite element (FE) in welding and subsequent operation, allowing for presence of ductile fracture micropores was determined in keeping with the following expression [3]:

$$d\varepsilon_{ij} = d\varepsilon_{ij}^{e} + d\varepsilon_{ij}^{p} + d\varepsilon_{ij}^{c} + \delta_{ij}\left(d\varepsilon_{T} + df/3\right), \qquad (1)$$

where $d\varepsilon_{ij}^{e}$, $d\varepsilon_{ij}^{p}$, $d\varepsilon_{ij}^{c}$, δ_{ij}, $d\varepsilon_T$, $\delta_{ij}\cdot df/3$ are the components of increments of tensor of strains due to elastic deformation mechanism, deformations of instantaneous plasticity, creep, kinetics of nonuniform temperature field and porosity, respectively, $(i, j) = \{r, b, z\}$ (Figure 1).

Increments of strain tensor were presented in the form of superposition of increment of the respective components [4, 5]:

$$\begin{gathered}\Delta\varepsilon_{ij} = \left[\Psi + \Omega\left(\sigma_i^*, T\right)\Delta\tau\right]\left(\sigma_{ij} - \delta_{ij}\sigma\right) + \\ +\delta_{ij}\left(K\sigma + \Delta\varepsilon_T + \Delta f/3\right) - \\ -\left[\frac{1}{2G} + \Omega\left(\sigma_i^*, T\right)\Delta\tau\right]\left(\sigma_{ij} - \delta_{ij}\sigma\right)^* - \left(K\sigma\right)^*,\end{gathered} \qquad (2)$$

where «*» symbol refers the respective variable to the previous tracing step; G is the shear modulus; $\Omega(\sigma_i, T) = A_c \exp\left(\frac{G_c}{T + 273}\right)\cdot\sigma_i^{n_c}$ is the creep function; n_c, A_c, G_c are the constants; Ψ — is the material state function that determines the condition of plastic flow

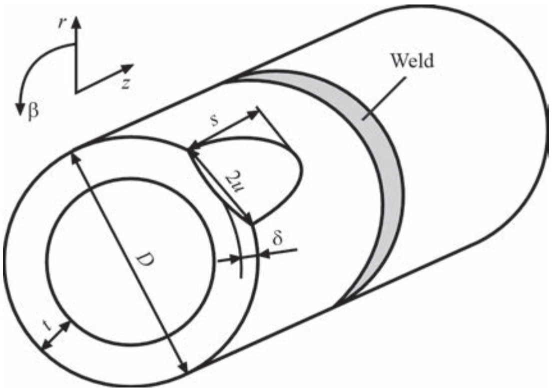

Figure 1. Scheme of a pipeline element with local defect of metal loss on the outer surface in a cylindrical system of coordinates

of metal in keeping with Gurson–Tvergaard–Needleman model [6]:

$$\begin{gathered}\Psi = \frac{1}{2G} + \Omega\left(\sigma_i^*, T\right)\Delta\tau, \\ \text{if } \sigma_i < \sigma_s = \sigma_T \times \\ \times\sqrt{1 + \left(q_3 f'\right)^2 - 2q_1 f' \cosh\left(q_2 \frac{3\sigma}{2\sigma_T}\right)}, \\ \Psi > \frac{1}{2G} + \Omega\left(\sigma_i^*, T\right)\Delta\tau, \text{ if } \sigma_i = \sigma_s, \\ \sigma_i > \sigma_s \text{ state is inadmissible.}\end{gathered} \qquad (3)$$

Determination of function Ψ is performed by iteration at each step of numerical tracing. Additional nonlinearity by the subcritical damage at the change of the external force factor F is solved by the following iteration process by function Ψ_k [7]:

$$F = \begin{cases} F + dF, \text{ if } f_0 K_1 \exp\left(K_2 \frac{\sigma}{\sigma_i}\right) d\varepsilon_i^p = \\ = \Psi_i \le \Psi_i^0 \approx 10^{-5}; \\ F, \text{if } \Psi_i > \Psi_i^0, \end{cases} \qquad (4)$$

where F is the system of force loads that act on the structure; dF is the increment of force loads during numerical tracing.

Strain hardening of the metal influences the shape of Mises flow surface which, depending on the intensity of accumulated plastic deformations, is usually considered in the following form [8]:

$$\begin{gathered}\sigma_T = \sigma_T^0\left[1 + c_1 \ln\left(\frac{\dot\varepsilon^p}{\dot\varepsilon_0}\right) + c_2\left\{\ln\left(\frac{\dot\varepsilon^p}{\dot\varepsilon_0}\right)\right\}^2\right] \times \\ \times\left[1 + \left(\frac{\varepsilon^p}{\varepsilon_0}\right)\right]^m\end{gathered} \qquad (5)$$

where $c_1 = 2.149\cdot10^{-3}$; $c_2 = 9.112\cdot10^{-2}$; $\varepsilon_0 = 1.540\cdot10^{-4}$, $m = 0.14$ are the constants; the dot over the variable denotes time differentiation.

If it is necessary to take into account the change of plastic deformation direction (for instance, at variable static loading, that causes alternating plastic deformation cycle), the following model of kinematic hardening of the material was used [9]:

$$\sqrt{\frac{3}{2}\left(\sigma_{ij}-\delta_{ij}\sigma-\bar{X}\right)\left(\sigma_{ij}-\delta_{ij}\sigma-\bar{X}\right)}- -\sigma'_{\mathrm{y}}\left(f'\right)\left[1+\left(\varepsilon^{p}/\varepsilon_{0}\right)\right]^{M}\le 0, \tag{6}$$

where $\bar{X}$ is the shear tensor; $\sigma'_{\mathrm{y}}\left(f'\right)$ is the current true yield limit of the damaged material, respectively (5); M, ε_0 are the material constants.

In order to predict ductile fracture initiation at plastic flow of the material of pipelines and pressure vessels from typical steels and alloys, modified Johnson–Cook criterion was used in nonisothermal cases, in keeping with which initial porosity of concentration f_0 develops in a certain metal volume, provided the following condition is fulfilled [10]

$$\chi_{\hat{e}}=\int\frac{\mathrm{d}\varepsilon_i^p}{\varepsilon_c\left(T\right)}>1, \tag{7}$$

where $\mathrm{d}\varepsilon_i^p=\sqrt{2}\big/3\cdot\sqrt{\mathrm{d}\varepsilon_{ij}^p\cdot\mathrm{d}\varepsilon_{ij}^p}$ is the intensity of increment of total plastic deformations (instantaneous plasticity and creep); $\varepsilon_c(T)$ is the critical value of plastic deformations.

Further increase of concentration of ductile fracture pores during plastic deformation of metal, in particular at static or cyclic loading in service, corresponds to modified Rice–Tracey law [11]. As the criterion of microscopic fracture initiation we proposed a numerical criterion of brittle-ductile fracture, namely satisfying one of the three conditions: plastic instability of porous material, taking into account its limited deformability by Mackenzie condition, critical development of pores and microcleavage S_K [12].

Definition of the limit state of a PE with a defect of local metal loss on the base of deterministic criteria cannot completely reflect the fracture susceptibility of a structure, as it considers fracture in the most critical point. In addition, indeterminateness of expert analysis that can be due to incompleteness of input data or inaccuracy of experimental measurements, requires respective increase of the conservativeness of the conclusions about PE technical condition. One of the alternative approaches that allow formally taking these factors into account, is application of integral statistical theories of strength. In particular, typical approaches to analysis of SSS of critical structures in terms of their fracture susceptibility, are based on Weibull's statistical theory of strength [13]. It envisages that damage initiation probability p is the function of the stressed state and it can be expressed using three-parameter Weibull distribution (σ-procedure). For the postulated problem of prediction of strength and operability of a steel or aluminium pipeline with revealed corrosion-erosion defects, it is formulated as follows:

$$p=1-\exp\left[-\int_S\left(\frac{\sigma_1-A_\sigma}{B_\sigma}\right)^{\eta_\sigma}\frac{\mathrm{d}S}{S_0}\right],\left(\sigma_1>A_\sigma\right), \tag{8}$$

where σ_1 is the principal stress field; S is the pipe cross-sectional area; S_0 is the scale factor constant; A_σ, B_σ, η_σ are the Weibull parameters.

Applicability of σ-procedure (8) is limited by the nature of subcritical damage of the material being considered, namely: if the structure does not lose its operability at plastic flow of metal up to reaching the limit state, the failure probability will be almost unchanged, accordingly, due to slight changes of stresses, whereas fracture probability will become higher. For instance, it is known that sufficient accumulation of creep deformations in the pipes at high-temperature operation leads to initiation and accumulation of subcritical porosity. However, no respective increase of stresses is observed here. Moreover, relaxation of stresses of a certain kind is observed (for instance, residual stresses in the welding zone). Thus, it can be concluded that models of (8) type are suitable for structures, the limit state of which is determined by brittle or ductile-brittle mechanisms of macrofracture (materials, embrittled as a result of radiation exposure or hydrogen saturation, etc.).

As the limit state of a pipeline with the detected metal loss depends mainly on ductile macrofracture (particularly, for ductile metals or in high-temperature operation), an alternative to (8) are Weibull models for probability assessment based on analysis of the structure deformed state (ε-procedure) in the following form [14]:

$$p=1-\exp\left[-\int_S\left(\frac{\varepsilon_i-A_\varepsilon}{B_\varepsilon}\right)^{\eta_\varepsilon}\frac{\mathrm{d}S}{S_0}\right],\left(\varepsilon_i>A_\varepsilon\right), \tag{9}$$

where ε_i is the deformation intensity, derived at finite element analysis; A_ε; B_ε, η_ε are the Weibull parameters.

In particular, for pipes from typical steels a series of numerical studies of the limit state, depending on the material properties and size of the semi-elliptical surface defect was performed (initial data for computations are as follows: $D\times t$ = 1420×20 mm, E = = 210 GPa, v = 0.3, σ_{y} = 300–600 MPa, f_0 = 0.01, S_K = = 1000 MPa, ε_c = 0.01). Solving the inverse problem showed that the dependencies of the conservative val-

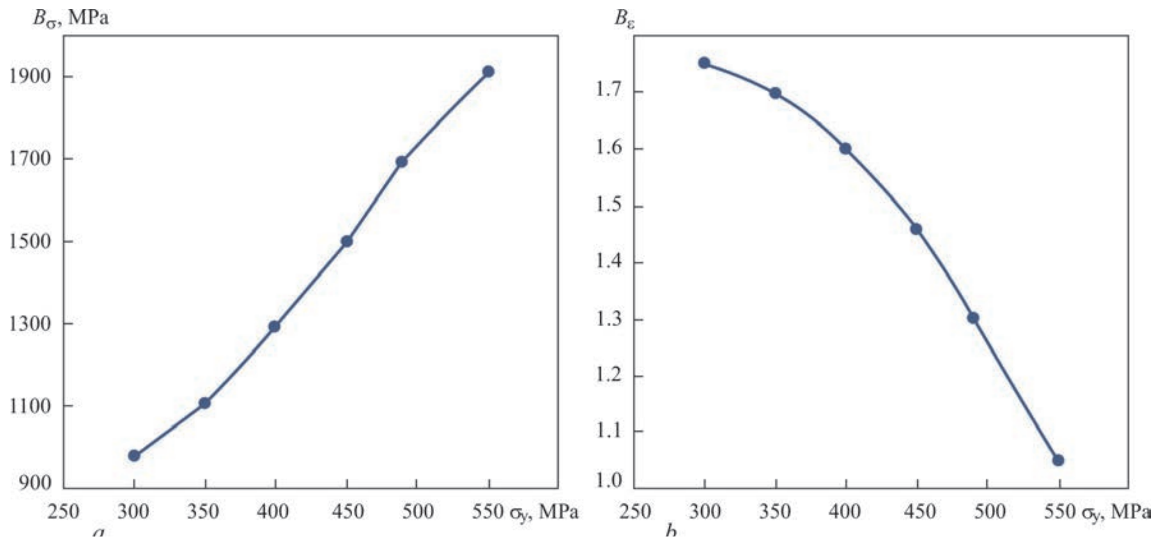

Figure 2. Dependencies of a conservative value of Weibull parameter B_σ (*a*) and B_ε (*b*) on yield limit σ_y of defective PE material (steel)

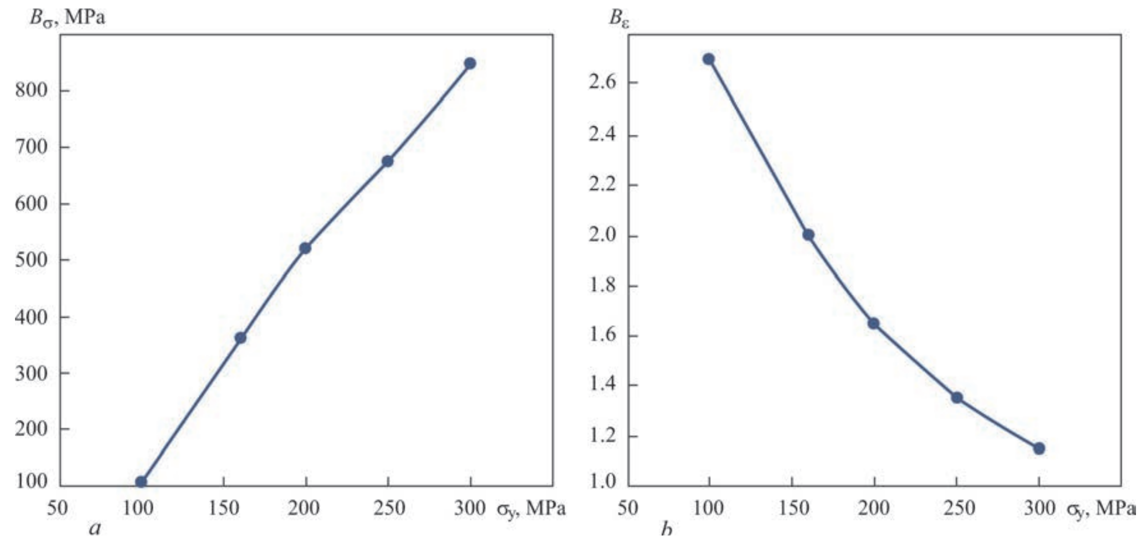

Figure 3. Dependencies of conservative value of Weibull parameter B_σ (*a*) and B_ε (*b*) on yield limit σ_y of defective PE material (aluminium alloys)

ues of Weibull B_σ and B_ε parameters on the yield limit σ_y of pipe steel are quasilinear (Figure 2) and only slightly depend on the size of the defect (range of the considered defect sizes in keeping with Figure 1 — δ = 3–17 mm, 2*s* = 20–200 mm; 2*u* = 20–200 mm). Similar results were obtained for aluminium alloys of different strength (Figure 3).

In order to determine the effect of the scale factor, which is taken into account in the methodology of probabilistic integral analysis of stresses and strains (8)–(9) using S_0 parameter, statistic testing for uniaxial tension of 165×20 mm samples of different thickness (6 and 10 mm) from aluminium alloy AMg6 was conducted. Thinner samples were made from the same plate 10 mm thick by grinding off; permanent butt joint was produced by arc welding. As shown in Figure 4, 10 mm samples have consistently lower level of limit stresses, and fracture susceptibility is described by three-parameter Weibull function (A_σ = 240 MPa; B_σ = 250 MPa; η_σ = 4), here S_0 corresponds to a value of 0.25 mm^2 for both the cases). This confirms prior conclusions that Weibull parameters in (8)–(9) are the

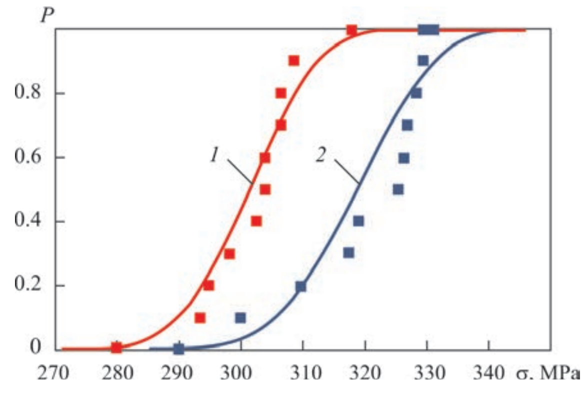

Figure 4. Determination of the impact of the scale factor (sample thickness) on fracture probability of welded samples from AMg6 aluminium alloy in keeping with theoretical calculation (solid line) and by the statistical laboratory testing (■): *1* — 10 mm thick samples, *2* — 6

material functions, and integration by the cross-section adequately takes the scale factor into account.

For the case of high-temperature operation of pipelines with detected defects of metal loss (for instance, erosion), fracture probability can be assessed using only the ε-procedure, taking into account the kinetics of creep deformation accumulation. As the material properties and its deformation susceptibility by the creep mechanism depend on temperature, temperature dependence of Weibull coefficients is to be expected. So, for typical steels 15Kh2NMFA and 10GN2MFA, which are widely used for manufacture of bodies and technological pipelines of NPP and TPP, the regularities of limit state formation under the conditions of simultaneous action of internal pressure and high temperature were studied in the case of an element of technological pipeline with a semi-elliptical defect of wall thinning; PE $Dxt = 300\times15$ mm. Coefficients of creep functions are as follows: 15Kh2NMFA — $n_c = 5.0$; $G_c = -101069$ °C; $A_c = \exp(69{,}40)$; 10GN2MFA — $n_c = 4.2$; $G_c = -61955$ °C; $A_c = \exp(34,\ 78)$ [15].

Derived by finite-element computation, distribution of deformations in the wall of a pipeline with a semi-elliptical defect of local thinning allowed solving the inverse problem of the limit state. This allowed determination of functional dependencies of B_ε parameter on material type and operating temperature. As shown in Figure 5, for 15Kh2NMFA and 10G2MFA steels temperature dependencies of B_ε are quasilinear for the selected temperature range and correspond to the range of values from 5.9 to 7.0. Here, the change of defect size only slightly affects the values of Weibull parameters.

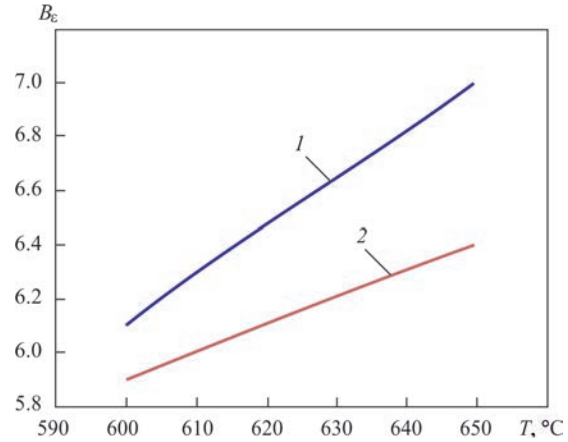

Figure 5. Dependencies of Weibull parameter B_ε of 10GN2MFA (*1*) and 15Kh2NMFA (*2*) steels on temperature

It is known that the statistical theories of computation are based on the assumption of availability of indeterminateness of certain input data or physical processes. Statistical Weibull's theory of strength deals with macroscopic characteristics of the state of material (stresses, strains) as characteristics of its microfracture susceptibility by the respective statistical description. Another typical factor of indeterminateness at analysis of the technical condition of structures in long-term service is the natural spatial scatter of material properties. Formal description of this phenomenon was performed using an algorithm based on Monte-Carlo method [16], within which it is assumed that pipeline fracture probability p at certain internal pressure P is determined by the frequency of achieving the limit state within a representative sample of equally possible combinations of pipe material properties, i.e.:

$$p(P) = N_p/N_r, \tag{10}$$

where N_p is the number of tests, at which the structure reached the limit state, at pressures lower than or equal to P, N_r is the total number of tests within the representative sample.

For formal description of spatial nonuniformity of such material properties as yield limit and Young's modulus, it is common to use the normal distribution, i.e. the probability density of X characteristic (assume a concrete value $X_{ijk}(i, j, k = r, \beta, z)$ can be presented in the following form:

$$\frac{\partial p}{\partial X_{ijk}} = \frac{1}{\beta_X\sqrt{2\pi}}\cdot\exp\left[-\frac{\left(X_{ijk}-\alpha_X\right)^2}{2\beta_X^2}\right], \quad i,\ j,\ k = r,\ \beta,\ z), \tag{11}$$

where α_X, β_X are the coefficients of normal distribution for X characteristic.

As regards different parameters of material fracture resistance, the Weibull distribution law is often used. Therefore, in the considered problem certain value Y in a point with coordinates (i, j, k) takes a specific value Y_{ijk} in keeping with the following relationship:

$$Y_{ijk} = \left[-\ln\left(1-RND\right)\right]^{\frac{1}{\eta_Y}}\left(B_Y - A_Y\right) + A_Y, \quad (i,\ j,\ k = r,\ \beta,\ z), \tag{12}$$

where A_Y, B_Y, η_Y are the Weibull coefficients for Y characteristic; RND is an arbitrary number from the following range [0;1].

Validation procedure of the developed models for determination of limit state of PE with a wall thinning defect consists in comparison of limit pressure P_{max}, obtained within the numerical study, with the available experimental data [17] on failure pressure P_{exp} that are extensively used, in particular, in development of normative documents. For steel pipes of different strength classes calculations allowed précising the input parameters of the models and confirming the applicability of the developed approaches for PE of

Table 1. Comparison of the results of numerical computations of limit pressure $P_{\max}$ in defective pipeline elements with the results of experimental testing P_{exp} from international data bases (steel pipes of different strength classes) [17]

t, mm	D, mm	δ, mm	$2s$, mm	$2u$, mm	σ_y, MPa	Strength class	P_{exp}, MPa	P_{max}, MPa	Error, %
4.83	275	2.11	157.5	43.1	350.6	X42	12.62	13.80	9.35
5.00	274	2.16	124.5	43.1	350.6	X42	13.35	14.15	5.99
4.93	274	1.60	45.7	43.0	350.6	X42	14.99	16.40	9.41
4.88	273	2.18	101.6	42.9	350.6	X42	15.18	14.15	6.79
8.64	324	0.00	0.0	0.0	356.4	X46	24.44	25.15	2.91
8.64	324	0.00	0.0	0.0	356.4	X46	24.52	25.15	2.57
8.53	324	0.00	0.0	0.0	356.4	X46	25.01	25.15	0.56
8.51	324	0.00	0.0	0.0	356.4	X46	25.06	25.15	0.36
9.37	864	4.62	91.4	135.7	356.4	X46	9.17	8.35	8.94
9.47	864	3.00	185.4	135.7	356.4	X46	10.56	11.20	6.06
8.43	324	0.00	0.00	0.00	356.4	X46	23.27	25.15	8.08
8.74	324	0.00	0.00	0.00	356.4	X46	23.92	25.25	5.56
8.61	324	3.30	144.8	50.8	356.4	X46	23.93	22.60	5.56
8.64	323	2.16	63.5	50.8	356.4	X46	24.37	26.50	8.74
8.64	323	2.69	61.0	50.8	356.4	X46	25.23	25.20	0.12
5.26	273	1.73	139.7	42.9	402.5	X52	18.06	17.75	1.72
5.74	507	3.02	132.1	79.6	462.3	X55	10.73	10.25	4.47
17.50	762	8.75	200.0	50.0	464.5	X65	9.17	8.35	8.94
17.50	762	8.75	200.0	100.0	464.5	X65	10.56	11.20	6.06
17.50	762	4.38	200.0	50.0	464.5	X65	10.73	10.25	4.47

different typesizes, and also confirming the satisfactory accuracy of the developed procedures (Table 1).

As regards aluminium PE with local geometric anomalies of corrosion-erosion type, validation was also conducted by comparing the results of numerical prediction of the limit pressure in cylindrical samples from AA 6082 alloy with the data base of laboratory tests (Table 2) [18]. As shown by the results of comparison of the computational and experimental data, the error of numerical prediction of limit pressure is not more than 10 % that is sufficient for the majority of practical tasks.

Proceeding from the developed approaches, we studied the effect of assembly welding on the limit state of PE with local metal loss in typical cases of defective sections of the main and technological pipelines. We considered a steel element of the main pipeline ($D = 1420$ mm, $t = 20$ mm) with an isolated defect of local wall thinning of a semi-elliptical shape on the pipe outer surface ($2s \times 2u \times \delta = 20 \times 20 \times 5$ mm). Presence of a circular weld leads to formation of a residual SSS in the assembly weld area and a change in the susceptibility to ductile fracture, as a result of presence of stress stiffness gradient $r_{st} = \sigma/\sigma_i$ (Figure 6). It should be noted that the stiffness of the structure stressed state is one of the factors that determine fracture resistance under the conditions of developed plastic flow of metal under the impact of external loading. Here, the strongest impact of local inhomogeneity of r_{st} in the area of the weld is observed at the first stages of plastic flow of PE metal under the impact of internal pressure, as a significant development of plastic deformation causes a certain homogenizing of the stressed state.

Thus, in case of presence in the area of a circular assembly weld of a local geometric anomaly in the form of surface metal loss, two sites of intensive development of subcritical metal damage at increase of internal pressure can be singled out: weld and HAZ with higher stiffness of the stressed state and geo-

Table 2. Comparison of the results of numerical computations of limit pressure in defective aluminium pipeline elements with the data of laboratory tests [18]

t, mm	D, mm	δ, mm	$2s$, mm	$2u$, mm	P_{exp}, MPa	P_{max}, MPa	Error, %
3.1750	145.542	1.6002	38.1508	9.525	10.5494	10.5	0.47
3.2512	145.694	1.6764	38.0492	38.0492	13.1695	11.9	9.64
2.8448	145.898	0.508	40.2336	10.1092	14.8243	14.5	2.19
2.8448	142.850	2.0066	38.2016	10.0076	7.23975	7.30	0.83
3.1496	137.871	2.413	12.1412	3.9878	14.4795	13.2	8.84
3.1242	137.820	2.540	6.1214	9.652	15.6861	16.6	5.83
3.1242	137.820	2.2606	59.6392	10.2616	6.55025	6.50	0.77
3.1496	137.871	2.3876	12.319	363.499	8.9635	9.40	4.87
6.2992	145.694	5.3594	53.4924	9.8298	11.7215	11.6	1.04
6.2484	145.593	4.699	13.7668	9.779	22.7535	24.1	5.92

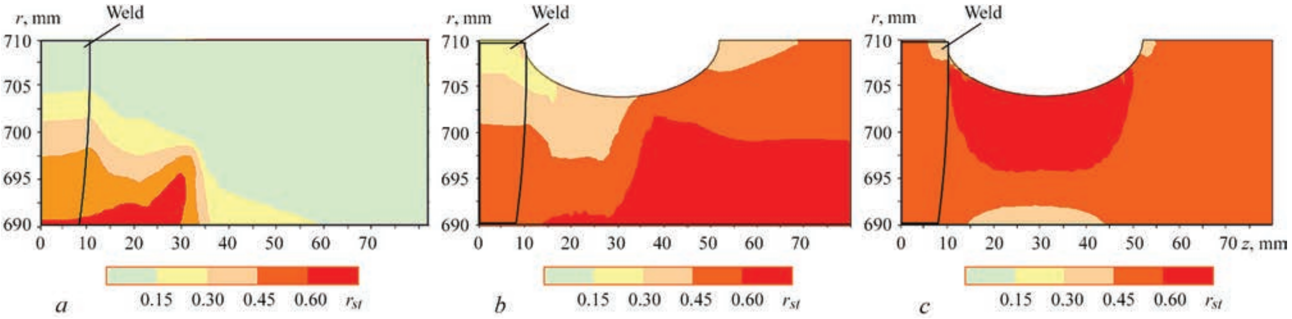

Figure 6. Distribution of stress stiffness r_{st} in the pipeline cross-section ($D \times t$ = 1420×20 mm, X65) with external corrosion defect ($2s \times 2u \times \delta$ = 40×20×5 mm) in the circular weld area at internal pressure P: *a* — after welding; *b* — 7.5 MPa; *c* —at limit pressure of 22.8 MPa

metrical stress raiser proper (Figure 7). As a close location (smaller than the defect length) of the weld and metal loss, a common field of subcritical damage forms between them that has a negative impact on the pipeline load-carrying capacity, as it is the site of potential initiation of a macrodefect.

In case of PE high-temperature operation, presence of a local stress raiser in the form of surface

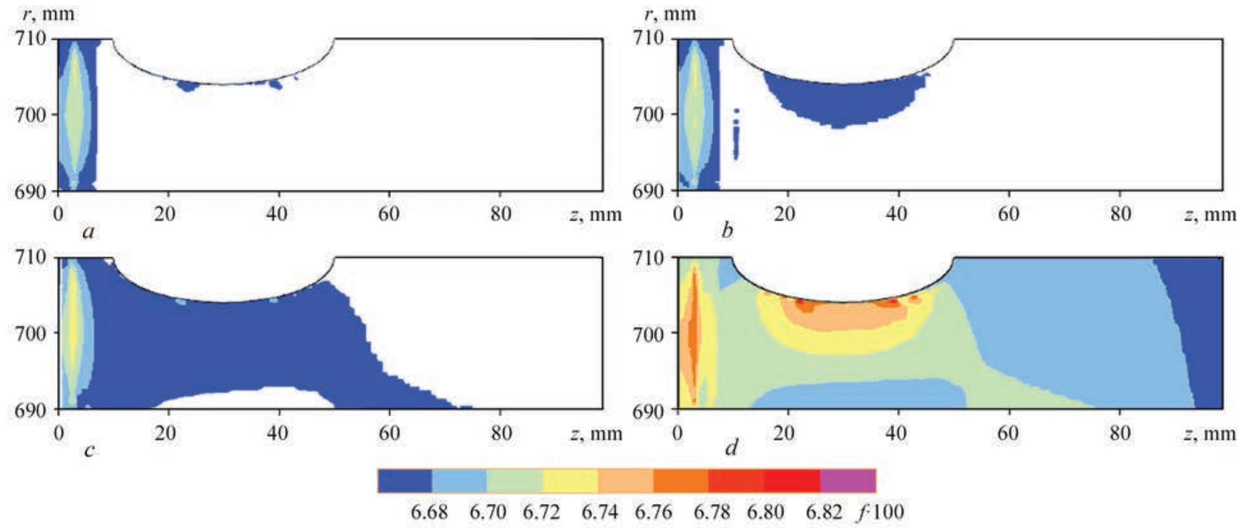

Figure 7. Distribution of the field of volume concentration f of ductile fracture pores in the cross-section of pipeline element ($D \times t$ = = 1420×20 mm, X65) with local metal loss at the periphery of a circular weld at different values of external pressure P: *a* — 16.5 MPa; *b* — 17.0; *c* — 20.0

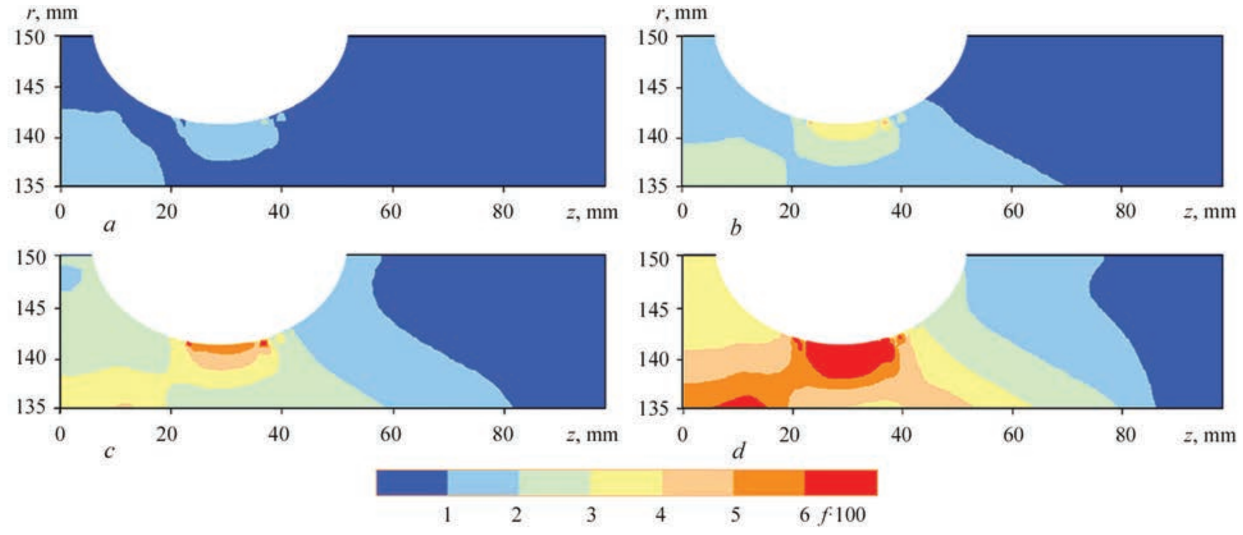

Figure 8. Distribution of the field of volume concentration f of ductile fracture pores in the cross-section of pipeline element wall ($D \times t$ = 300×15 mm, 10GN2MFA) with local metal loss at the periphery of a circular weld at different time τ of high-temperature operation (T = 650 °C, P = 13 MPa): *a* — 400 s; *b* — 800 s; *c* — 1200 s; *d* — 1500 s

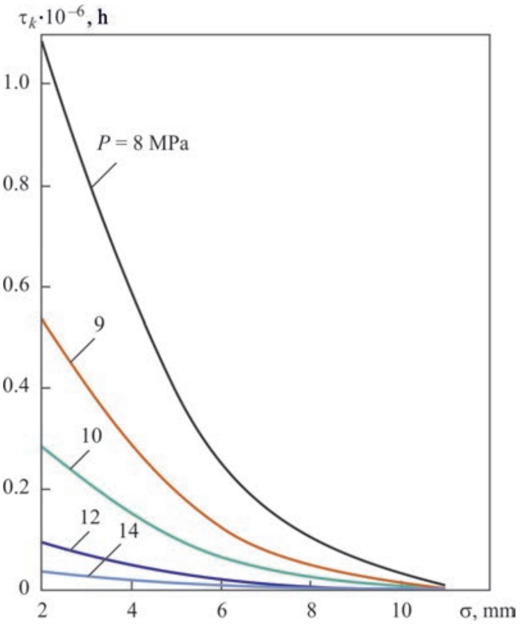

Figure 9. Dependencies of time to macroscopic fracture of pipeline element τ_k ($D \times t$ =300×15 mm, 10GN2MFA) on the depth of thinning defect δ in the area of an assembly weld at different values of internal pressure P (defect length $2s$ = 30 mm)

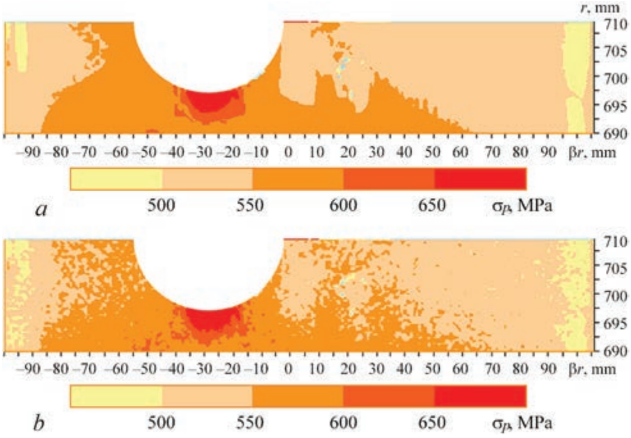

Figure 11. Distribution of residual equivalent stresses in a pipeline ($D \times t$ = 1420×20 mm, X65 steel) with external corrosion defect ($2s \times 2u \times \delta$ = 55×40×10 mm) at limit external pressure: *a* — traditional calculation with constant material properties; *b* — computation by Monte-Carlo algorithm

geometrical anomaly has a fundamentally different impact on PE state. So, in the case of an element of process pipeline from 10GN2MFA steel ($D \times t$ = = 300×15 mm) with semi-elliptical local wall thinning ($2s \times 2u \times \delta$ = 40×40×7 mm) on the pipe outer surface it was shown that the defect presence causes similar regularities of subcritical damage accumulation in high-temperature operation (T = 625 °C, P = = 13 MPa). However, the main deformation mechanism here is high-temperature creep (Figure 8). So, at the start of operation the spatial distribution of concentration of ductile fracture pores is characterized by two local maximums, namely near the defects and in the weld area. Further development of creep deformations causes an increase and combining of these two areas of subcritical damage, that determines the limit state of the welded pipeline. It should be noted that a characteristic feature of PE fracture during material creep is relaxation of post-welding stresses, as a result of accumulation of irreversible creep deformations that gradually lowers the growth rate of ductile fracture pores in the weld area.

Assessment of admissibility of a defect of local thinning of pipeline wall for the case of low-temperature operation differs essentially from the one which concerns the conditions of force impact at high temperatures: corrosion-erosion defect, which at analysis of static strength belongs to admissible ones and slightly lowers PE load-carrying capacity in a certain range of internal pressure values, during the operation period leads to damage accumulation and further macroscopic fracture of the structure that should be taken into account at substantiation of the residual service life of critical PE. Effect of the dimensions of the defect of local thinning of pipeline wall for the period up to macroscopic fracture of pipeline element, τ_k, that was studied by numerical modeling in the case

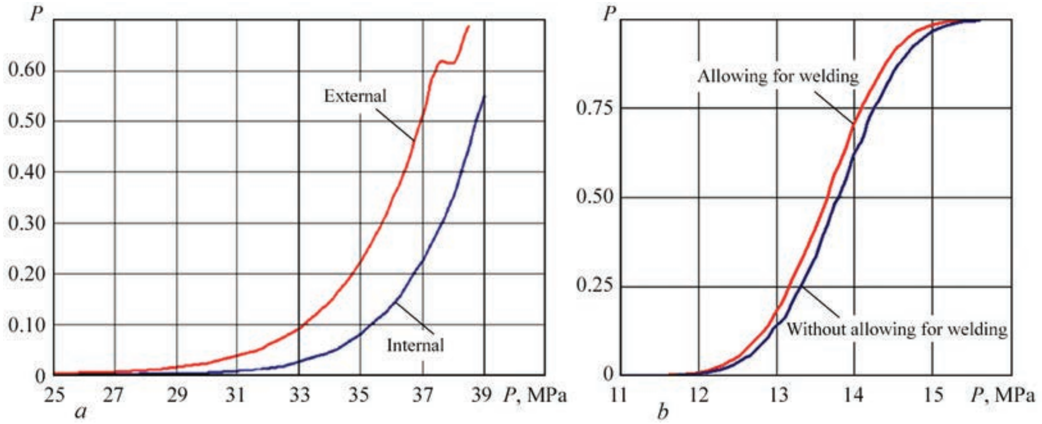

Figure 10. Effect of the surface of thinning defect location ($2s \times 2u \times \delta$ = 100×80×9 mm, $D \times t$ = 530×18 mm, X65) — (*a*) and presence of a circular weld ($2s \times 2u \times \delta$ = 50×50×5 mm, $D \times t$ = 530×10 mm, AMg6) — (*b*) on PE fracture probability p at different values of internal pressure P

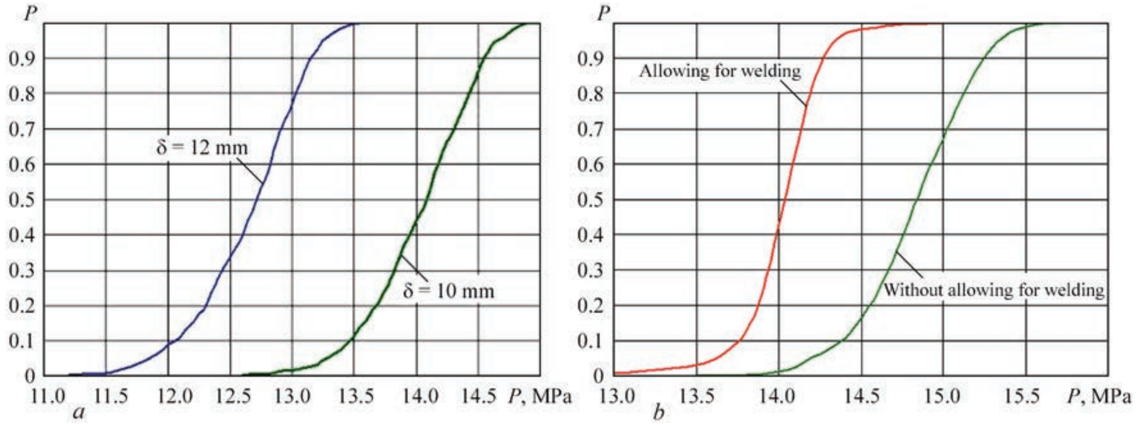

Figure 12. Dependencies of pipeline fracture probability p ($D \times t$ = 1420×20 mm, X65) with external corrosion defect ($2s \times 2u \times \delta$ = 20×20×10 mm) on internal pressure P, taking into account stochastic nonuniformity of properties: *a* — for different values of defect depth δ; *b* —– taking into account the presence of a weld at the defect periphery

of PE with defects of different depth δ (T = 650 °C, P = 13 MPa), is of a pronounced non-linear nature (Figure 9). This is related to multifactoriality of the processes of elasto-plastic deformation and fracture of a pipeline with certain residual post-welding SSS.

Results of finite-element computation of SSS of a pipeline with the detected corrosion-erosion defects enable numerical prediction of PE fracture probability within the Weibull theory (8)–(9). Here, not only spatial distribution of the fields of stresses (strains), interaction of the fields of stresses of the first and second kind, but also actual characteristics of ductile fracture resistance of the material are taken into account. So, application of 3D models of the stress-strain and damage states of PE with a 3D defect of local wall thinning allow with minimum conservatism taking into account the features of actual geometry of the structure, in particular, defect location surface (Figure 10, *a*). Moreover, it is thus possible to perform quantitative analysis of the impact of assembly welding at different stages of loading by internal pressure right up to the limit state (Figure 10, *b*).

For numerical analysis of the impact of stochastic nature of distribution of the properties of the studied defective PE material on the current SSS and limit state, it was assumed that the spatial scatter is demonstrated by the material yield limit (by the normal law, α = 408 MPa, β = 10.34 MPa), critical deformation of initiation of ductile fracture pores (by Weibull distribution, $A_\varepsilon = 0.001$, $B_\varepsilon = 0.0061$, $\eta_\varepsilon = 4$), initial concentration of ductile fracture pores (by Weibull distribution, $A_f = 0.0001$, $B_f = 0.000397$, $\eta_f = 2$). Presence of a defect in the area of a circular assembly weld under the conditions of operational loading by internal pressure only slightly affects the nature of the change of current and limit SSS, because of scatter of PE material properties (Figure 11).

Thus, we can conclude that despite the nonuniform properties of the material, the nature of interaction of residual stresses in the welding area and of operational stresses (taking into account the geometrical stress raiser) remains the same, as in traditional modeling, within the models of a uniform continuous medium. The nonuniformity the most significantly affects the macrofracture initiation and onset of the limit state of the structure: appearance of weaker regions in atypical zones leads to lower breaking pressure, or, contrarily, to strengthening of the weakest regions, and strengthens the load-carrying capacity of the structure.

Application of direct Monte-Carlo methods, alongside the respective finite-element solution of multiphysical problems of limit state determination, allows evaluation of the impact of typical parameters of the actual state of pipeline defective sections on their reliability, taking into account the indeterminateness of spatial distribution of structure material properties. In particular, it is known that defect depth has the greatest impact on the load-carrying capacity of PE with a defect of local corrosion-erosion thinning. For the above case of PE with a detected thinning defect, the fracture probability, depending on internal pressure at different values of defect depth, is shown in Figure 12, *a*. Increase of defect depth causes a shifting of $p(P)$ curve at preservation of similarity. It is explained by that this range of variation of the radial defect size does not cause a change in the fracture mechanism.

Presence of a defect in the area of assembly weld has an additional negative effect on the load-carrying capacity of the pipeline defective area that is due to intensification of the growth of ductile fracture pores in the areas of higher stiffness of the stressed state. This is quantitatively described by the respective probabilistic curves, the example of which is given in Figure 12, *b*. From these data one can see that the weld presence changes the susceptibility of a defective PE to fracture under the impact of internal pressure: in addition to the anticipated shifting of $p(P)$ curve relative to the case of an unwelded pipe, the slope of the probabilistic fracture curve decreases in the presence of the weld.

Conclusions

1. A set of mathematical models was developed for prediction of simultaneous processes of thermal deformation and subcritical fracture of metal of welded elements of the main and technological pipelines and pressure vessels with detected defects of local corrosion-erosion metal loss under the conditions of welding and further operation. A satisfactory accuracy of numerical determination of limit pressure in PE with surface defects is shown.

2. Based on the results of numerical studies of limit state of typical pipeline elements with surface metal losses near the areas of assembly or repair welding it is shown that the interaction of these two anomalies of the structure consists in formation of a common area of subcritical fracture by the ductile mechanism, which is the zone of potential formation of a macroscopic defect and violation of pipe integrity. For the case of high-temperature operation of pipelines this effect is more significant, due to additional deformation of metal by the creep mechanism.

3. Procedures were developed for numerical determination of fracture probability of welded pipeline elements with detected surface defects of local corrosion-erosion loss of metal based on the statistical Weibull theory of strength and direct Monte-Carlo method. As regards pipe steels of different strength classes, as well as aluminium alloys, values of Weibull coefficients as a function of material properties, were derived.

4. By the results of numerical studies of the impact of spatial nonuniformity of PE properties on fracture probability it is shown that, despite the nonuniformity of material properties the nature of interaction of residual stresses in the welding area and operating stresses (taking into account the geometrical stress raiser) remains the same as at traditional modeling within the models of uniform continuous medium.

1. Lemaitre, J., Desmorat, R. (2005) *Engineering damage mechanics*. Ductile, Creep, Fatigue and Brittle Failures. Berlin, Springer-Verlag. https://doi.org/10.1007/b138882.
2. de Geus, T.W.J., Peerlings, R.H.J., Geers, M.G.D. (2015) Microstructural modeling of ductile fracture initiation in multiphase materials. *Engineering Fracture Mechanics*, **147**, 318–330. https://doi.org/10.1016/j.engfracmech.2015.04.010.
3. Makhnenko, V.I. (2013) Problems of examination of modern critical welded structures. *The Paton Welding J.*, **5**, 21–28.
4. Wei, Y., Zhang, L., Au, F.T.K. et al. (2016) Thermal creep and relaxation of prestressing steel. *Construction and Building Materials*, **128**, 118–127. https://doi.org/10.1016/j.conbuildmat.2016.10.068.
5. Velikoivanenko, E., Milenin, A., Popov, A. et al. (2019) Methods of numerical forecasting of the working performance of welded structures on computers of hybrid architecture. *Cybernetics and Systems Analysis*, 55(**1**), 117–127. https://doi.org/10.1007/s10559-019-00117-8.
6. Xue, L. (2007) Damage accumulation and fracture initiation in uncracked ductile solids subject to triaxial loading. *Int. J. of Solids and Structures*, **44**, 5163–5181. https://doi.org/10.1016/j.ijsolstr.2006.12.026.
7. Milenin, A.S., Velikoivanenko, E.A., Rozynka, G.F., Pivtorak, N.I. (2016) Simulation of subcritical damage of metal in welded pipeline elements at low-cycle loading. *Tekh. Diagnost. i Nerazrush. Kontrol*, **4**, 14–20. https://doi.org/10.15407/tdnk2016.04.03.
8. Jones, N. (2012) *Structural Impact*. Second edition. Cambridge University Press. https://doi.org/10.1017/CBO9780511624285
9. Lemaitre, J., Chaboche, J.-L. (1990) *Mechanics of Solid Materials*. Cambridge University Press. https://doi.org/10.1017/CBO9781139167970.
10. Milenin, A.S., Velikoivanenko, E.A., Rozynka, G.F., Pivtorak, N.I. (2013) Simulation of processes of initiation and propagation of ductile fracture pores in welded structures. *The Paton Welding J.*, **9**, 26–31.
11. Chen, Z., Butcher, C. (2013) *Micromechanics Modelling of Ductile Fracture*. Springer Netherlands. https://doi.org/10.1007/978-94-007-6098-1.
12. Milenin, O. (2017) Numerical prediction of the current and limiting states of pipelines with detected flaws of corrosion wall thinning. *J. of Hydrocarbon Power Engineering*, 4(**1**), 26–37.
13. Lindquist, E.S. (1994) Strength of materials and the Weibull distribution. *Probabilistic Engineering Mechanics*, 9(**3**), 191–194. https://doi.org/10.1016/0266-8920(94)90004-3.
14. Milenin, A., Velikoivanenko, E., Rozynka, G., Pivtorak, N. (2019) Probabilistic procedure for numerical assessment of corroded pipeline strength and operability. *Int. J. of Pressure Vessels and Piping*, **171**, 60–68. https://doi.org/10.1016/j.ijpvp.2019.02.003.
15. Makhnenko, V.I. (2016) *Safe operating life of welded joints and assemblies of modern structures*. Kiev, Naukova Dumka [in Russian].
16. Lawless, J.F. (2002) *Statistical Models and Methods for Lifetime Data*. John Wiley & Sons, Inc., Floboken, New Jersey. https://doi.org/10.1002/9781118033005.
17. Cronin, D. (2000) *Assessment of Corrosion Defects in Pipelines*. PhD thesis. University of Waterloo.
18. Kitching, R., Zarrabi, K. (1982) Limit and burst pressures for cylindrical shells with part-through slots. *Int. J. of Pressure Vessels and Piping*, 10(**4**), 235–270. https://doi.org/10.1016/0308-0161(82)90035-7

Received 19.08.2020

https://doi.org/10.37434/tpwj2020.09.02

IMPACT OF THERMAL CYCLES OF WELDING ON FORMATION OF THE STRUCTURE AND PROPERTIES OF CORROSION-RESISTANT STEEL 06G2BDP

A.V. Zavdoveev[1], **V.D. Poznyakov**[1], **S.L. Zhdanov**[1], **M. Rogante**[2], **A.O. Maksymenko**[1], **O.G. Sineok**[1] and **A.M. Gerasymenko**[1]
[1]E.O. Paton Electric Welding Institute of the NAS of Ukraine
11 Kazymyr Malevych Str., 03150, Kyiv, Ukraine. E-mail: office@paton.kiev.ua
[2]Rogante Engineering Office
62012 Civitanova Marche, Italy

High-strength low-alloy steels with high service properties, in particular, resistance to atmospheric corrosion, become ever wider applied in mechanical and industrial engineering. Their application allows not only reducing specific weight of metal structures, but also increasing their reliability and operating life. In view of that, on the base of steel 06G2B, steel 06G2BDP with higher corrosion resistance was developed. In order to improve its corrosion resistance, copper and phosphorus content in the steel was increased. The work deals with the issue of the impact of thermal cycles of welding on mechanical properties and structure of HAZ metal in welded joints of atmospheric-resistant steel 06G2BDP. It is shown that as to the values of static strength, ductility and impact toughness steel 06G2BDP is not inferior to steel 06G2B, and is superior to steel 10KhSND. Its application is rational as an alternative to the above-mentioned steels in fabrication of modem metal structures by gas-shielded manual and mechanized arc welding in the range of HAZ metal cooling rates specified for them. 13 Ref., 2 Tables, 4 Figures.

Keywords: corrosion-resistant steel, thermal cycle of welding, heat-affected zone, structure, properties

High-strength low-alloy steels with high service characteristics: strength, toughness, resistance to atmospheric corrosion are becoming ever more widely used in mechanical engineering and industrial construction, in particular, in bridge construction. Their use allows not only reducing specific weight of metal structures, but also increasing their reliability and operating life. The results of the inspection of state of the metal structures of bridges with steel main and transverse beams and a steel reinforced concrete roadway show that the main type of their damages is a reduction in the cross-sectional sizes of girths and beam walls as as result of corrosion, which significantly reduces bearing capacity and serviceability of bridges [1]. The combination of sometimes inefficient design and technological solutions coupled with the use of conventional construction steels in bridges in the former times strengthen and accelerate the corrosion processes in the structure [2].

A large number of research works was devoted to corrosion resistance of low-alloy steels in atmospheric conditions. In particular, they indicate that limited atmospheric-resistant low-alloy steels contain elements which under the influence of the ordinary atmosphere, form a film of corrosion products on the surface, which has protective properties. The steels of this type were developed in the USA and were originally used in the bodies of railway cars. In the 1960s, such steels began to be used in other structures, such as steel reinforced concrete bridges [3].

The influence of the chemical composition on the rate of atmospheric corrosion of the metal was considered in many works [4–6]. It was found that an increased content of copper, phosphorus, chromium, as well as nickel and molybdenum improves the resistance of steel to atmospheric corrosion [4]. In ASTM G101 the index is presented, by which it is possible to judge about the resistance of steel to atmospheric corrosion: $I = 26.01\,\mathrm{Cu} + 3.88\,\mathrm{Ni} + 1.20\,\mathrm{Cr} + 1.49\,\mathrm{Si} + 17.28\mathrm{P} - 7.29\,\mathrm{CuNi} - 9.10\,\mathrm{NiP} - 33.39\,\mathrm{Cu}$.

The scale of application of weather-resistant steels in bridge structures in different countries is different. In Germany and France such bridges are rare, while in Italy and Great Britain their number is the largest. In the USA and Japan about 50 % of metal and combined bridges are made of weather-resistant steels [7–9].

In Ukraine, during the last fifteen years, steels 06GB, 06G2B and 10KhSND were introduced and successfully used in the construction of critical welded structures. Sparsely-alloyed steels of high strength and cold resistance differ favorably from steels, which are usually used in the manufacture of domestic metal structures. Steels of this class belong to the steels with carbonitride strengthening. They are low-carbon (C = 0.04–0.08 %) and sparsely-alloyed, at the same time having bal-

A.V. Zavdoveev — https://orcid.org/0000-0003-2811-0765, V.D. Poznyako — https://orcid.org/0000-0001-8581-3526,
S.L. Zhdanov — https://orcid.org/0000-0003-3570-895X, M. Rogante — https://orcid.org/0000-0002-6846-0826

Table 1. Chemical composition of steels, wt.%

Steel	C	Si	Mn	P	S	Al	Cr	Mo	Ni	Cu	Nb	Ti
06G2BDP	0.08	0.35	1.4	0.05	0.012	0.02	0.30	0.02	0.30	0.3	0.03	0.02
06G2B	0.08	0.25	1.3	0.025	0.01	0.02	–	0.1	–	0.3	–	–
10KhSND	≤0.12	0.8	0.8	0.03	0.035	–	0.6	–	0.5	0.4	–	–

anced mechanical and technological properties [10–12]. Corten A and Corten B differ from foreign steels in their lower content of such elements as nickel, chromium and molybdenum. At present, these steels were successfully used in the construction of a number of critical objects, such as blast furnace at the Kryvyi Rih ore-mine combine, oil storage tanks with a capacity of 50000 and 75000 m^3, separate elements of bridge structures through the entrance to the harbor of Podilsk bridge transition.

Taking into account the interest of bridge builders in the use of weather-resistant rolled metal for girder structures, on the basis of steel 06G2B, steel 06G2BDP with a high resistance to corrosion was created [13]. To improve a corrosion resistance in steel, the content of copper and phosphorus is increased. As is mentioned above, phosphorus improves strength as well as atmospheric corrosion resistance, especially in contact with copper. At the same time, the deformation properties of steel are deteriorated. In addition, it is known that an increased content of phosphorus in steel can reduce its cold resistance and deteriorate the weldability. Therefore, the aim of this work was to study the impact of thermal welding cycles on the mechanical properties and structure of the HAZ metal of welded joints of steel 06G2BDP.

Procedure of investigations. As the object of investigation the steels were selected, the chemical composition and mechanical properties of which are given in Table 1 and Table 2.

In accordance with GOST 9.911–89 and GOST 9.908–85 in the laboratory conditions of the E.O. Paton Electric Welding Institute, comparative investigations of corrosion resistance of the proposed steel and rolled steels 10KhSND and 06G2B were performed, which are widely used in bridge construction. The standard GOST 9.911–89 regulates the method of comparative accelerated corrosion tests of low-alloy steels which are applied without the protection against atmospheric corrosion. This method of investigations can also be used to obtain comparative data on corrosion resistance of carbon and low-alloy steels used with protective coatings. The essence of the method is to accelerate the corrosion process of formation of protective layers of corrosion products on the steel surface. Acceleration of the corrosion process is achieved by increasing the relative humidity of air and temperature under the action of sulfur dioxide, periodic condensation of moisture, as well as alternating wetting of the specimens surface with electrolyte and its subsequent drying.

The specimens of investigated steels in the amount of not less than 3 pcs (100×50×1.5 mm) were compared with the specimens of the reference steel. In this study, as a reference the specimens of 10KhSND steel were used. The tests were performed cyclically with periodic changes of the first and second stages of the cycle. The duration of one cycle is 168 h. The total duration of the tests is 7 cycles (1176 h). The first stage of the cycle proceeds as follows: in the atmosphere of SO_2 at a temperature of 40 °C for 7 h and then at a temperature of 20 °C for 64 h. The second stage of the cycle proceeds as follows: periodic immersion of the specimens in the solution of $5\cdot10^{-6}$ mol/l of a sulfuric acid for 97 h (10 min in the solution and 50 min in air, including at air flow at a temperature of 60 °C) in the installation «corrosion wheel».

The values of corrosion and corrosion resistance were determined according to GOST 9.908–85. As the main value of a continuous corrosion a decrease in mass per unit area of the specimens and the rate of loss of mass of the specimens was accepted.

The dependence of mechanical properties on the cooling rate of the HAZ metal in the temperature range of 600–500 °C was studied using the model specimens of the size 120×12×12 mm, which were heated and cooled in accordance with the thermal cycles of arc welding in the specialized equipment MCR-75. The heat treatment process was as follows. Initially, the specimens were heated to the temperature of 1200–1300 °C, which are characteristic of the area of overheating of HAZ of welded joints. The heating rate of the specimens was 150–170 °C/s, which corresponds to the conditions of heating the metal in the heat-affected-zone during arc welding processes. At this temperature, the specimens were kept for approximately 2 s, and then forcibly cooled. To provide different cooling rates of the heated specimens, the conditions of their cooling were changed. Thus, to provide cooling rates in the range from 3.0 to 7.5 °C/s, the specimens were cooled by cooling the copper clamps of the installation with running water of different flow intensity. Higher cooling rates were achieved as a result of additional blowing of the specimens with inert gas, which allowed regulating $w_{6/5}$ from 8.0 to 20.0 °C/s by changing intensity of gas flow. The heating-cooling rate of the specimens was controlled by a chromel-alumel thermocouple with a diameter of 0.5 mm.

Table 2. Mechanical properties of steels

Steel	σ_y, MPa	σ_t, MPa	δ_5, %	KCV^{-40}
06G2BDP	608	684	22	355
06G2B	490	590	20	98
10KhSND	390	530–660	19	29

From each batch of heat-treated model specimens, standard specimens were manufactured to perform mechanical tests and determination of impact toughness of the HAZ metal. For static tensile tests, the specimens of type II (3 specimens for each cooling rate) and for impact bending the specimens of type IX were manufactured in accordance with GOST 6996–96. The impact toughness was determined when testing Charpy specimens with a sharp notch at the testing temperatures of 20, –20 and –40 °C. According to the results of the tests, the effect of cooling rate on the change of the following indices of the HAZ metal was evaluated: static strength (σ_y and σ_t, MPa); ductility (δ_5 and ψ, %) and toughness (KCV J/cm^2).

Metallographic examinations were performed using a microscope «Neophot-32», the microhardness of separate structural components and the integral hardness of the metal was measured in the durometer M-400 of the LECO Company at the loads of 100 g ($HV_{0.1}$) and 10 kg (HV_{10}). The specimens for investigations were prepared by the standard method using diamond pastes of different dispersion, the detection of microstructure was performed by chemical etching in 4 % alcoholic solution of nitric acid.

Results and discussion. According to the thermokinetic decay diagrams of supercooled austenite, steels 06G2B and 06G2BDP under normal cooling conditions have mainly a bainitic structure. However, steel 10KhSND has a ferritic-pearlitic structure, which causes lower mechanical properties as compared to steels 06G2B and 06G2BDP. Under the conditions of accelerated cooling rates typical for the thermal cycle of welding, the structure of steel 06G2B in a quite wide range of cooling rates of the HAZ metal remains predominantly bainitic. At the same time, for steel 06G2BDP, due to additional alloying with phosphorus and copper, the area of bainitic transformation is slightly shifted, which is reflected in a greater tendency to bainite formation and, as a consequence, increased mechanical properties as compared to steel 06G2B. For steel 10KhSND the formation of pearlitic-bainitic structure at the cooling rates corresponding to the thermal cycle of welding is characteristic. This fact negatively affects the characteristics of cold resistance of this steel.

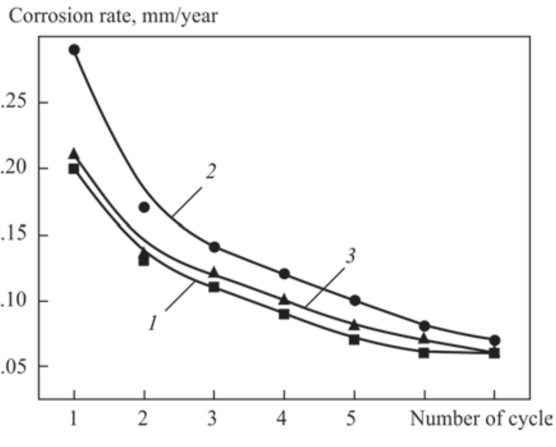

Figure 1. Change of corrosion rate of steel in the course of tests: *1* — 06G2BDP; *2* — 10KhSND; *3* — 06G2B

According to the results of the tests on corrosion resistance, it was found that its values for the investigated steel 06G2BDP are 20 % higher than in steel 10KhSND, and not inferior to steel 06G2B. This is evidenced by the data on the change in the corrosion rate shown in Figure 1, especially in the first cycles of investigations.

The results of metallographic examinations indicate that due to heat treatment in the form of hardening and tempering, in the studied steel 06G2BDP ferritic-carbide structure is formed (Figure 2, *a*) with a grain size of about 4–20 μm and a hardness HV206. This, in turn, provides high indices of static strength $\sigma_y > 600$ and $\sigma_t > 690$ MPa, ductility $\delta_5 > 21$ % and $\psi > 72$ % and impact toughness of the HAZ metal of steel 06G2BDP, which significantly exceed the normative values and similar indices of steel 10KhSND.

The dependences, characterizing changes in the indices of static strength and ductility in the simulated HAZ metal of steel 06G2BDP under the effect of thermal welding cycle are shown in Figure 3. For comparison, the given results of tests of the HAZ metal of steel 06G2B and 10KhSND are given.

The results of the carried out investigations indicate that at the cooling rate $w_{6/5} = 3$ °C/s in the temperature range of 600–500 °C, the yield strength of the HAZ metal decreases as compared to the initial state, namely $\sigma_{0.2}$ from 608 to 490 MPa, with an increase of $w_{6/5}$ to 14 °C/s, the yield strength increases to 544 MPa and up to 565 MPa at $w_{6/5} = 23$ °C/s. The static tensile strength σ_t decreases slightly to 657 MPa at $w_{6/5} = 3$ °C/s, and then it increases to 710 MPa at $w_{6/5} = 25$ °C/s. At the same time, the ductile properties of the simulated HAZ metal as compared to the initial state are changed insignificantly (changes do not exceed 5 %). A similar trend in terms of changes in the mentioned mechanical properties is characteristic also to the HAZ metal of steel 06G2B and 10KhSND, but the absolute values of these indices are lower.

During tests of specimens with a sharp V-shaped notch for impact bending, it was found that the impact toughness of the HAZ metal of steel 06G2BDP decreases relatively to the base metal (Figure 4). The most significant decrease in KCV values is observed in the specimens that were cooled at a rate of $w_{6/5} = 3$ °C/s (from 355 to 86 J/cm^2 at a test temperature of 20 °C, and from 316 to 10 J/cm^2 at a temperature of –40 °C). With an increase in the cooling rate to 14 °C/s, the values of impact toughness of the HAZ metal grow significantly to 270 J/cm^2 at the test temperature of 20 °C and only to 31 J/cm^2 at the test temperature of the specimens being –40 °C. A further increase in the cooling rate $w_{6/5}$ to 23 °C/s leads to a decrease in the impact toughness of the specimens tested at a temperature of 20 °C to $KCV^{20} = 180$ J/cm^2, at that time continued growing slightly and reached the values of KCV^{-40} = 35 J/cm^2.

It should be noted that the values of mechanical properties and impact toughness of the HAZ metal of steel 06G2B, on the base of which the corrosion-resistant steel 06G2BDP was developed, are almost on the same level with it. Regarding the values of impact toughness of the HAZ metal of the model specimens in steel 10KhSND a significant difference in their behavior under the action of thermal welding cycles can be distinguished as compared to sparsely-alloyed steels 06G2B and 06G2BDP. Namely, *KCV* values of the HAZ metal of the mentioned steel during the tests at the temperatures of 20 and –40 °C react weakly to changes in the cooling rate. This is evidenced by the fact that the impact toughness of the specimens of steel 10KhSND, which were tested at a temperature of 20 °C, are in the range of 55–75 J/cm^2, and at a temperature of –40 °C it is 14–22 J/cm^2.

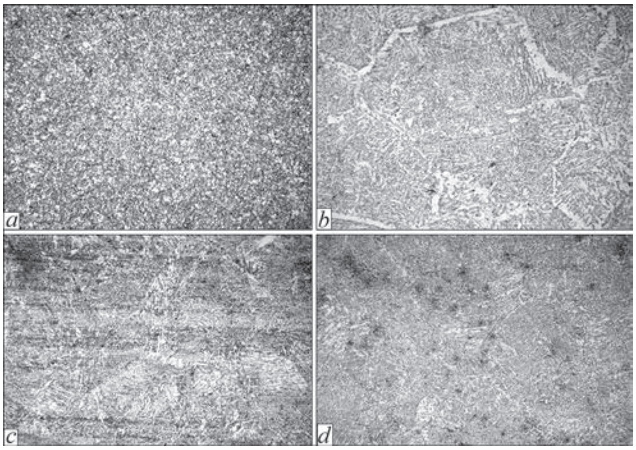

Figure 2. Microstructure (×200) of steel 06G2BDP depending on the value of cooling rate $w_{6/5}$: *a* — base metal; *b* — 3; *c* — 14; *d* — 23 °C/s

Changes in the mechanical properties of the HAZ metal of steel 06G2BDP are predetermined by different structural transformations in the range of the investigated cooling rates. This is evidenced by the results of metallographic examinations. Metallographic examinations established that in the area of overheating in the HAZ metal of steel 06G2BDP at a cooling rate $w_{6/5}$ = 3 °C/s, a structure formed consisting of a ferritic-pearlitic mixture with ferrite fringes (Figure 2, *b*), the average grain size is of the order of 300 μm. The hardness of such metal is *HV* 270. When $w_{6/5}$ rises to 14 °C/s, an equilibrium bainite structure is formed with 70 % content of upper bainite and 30 % of lower one. The grain size decreases and is equal to 100 μm, and hardness increases to *HV* 303.

At a further increase in the cooling rate to $w_{6/5}$ = = 23 °C/s in the simulated HAZ metal, a structure is formed consisting of a mixture of upper (30 %) and lower bainite (70 %). Due to that, the hardness of the metal ranges from *HV* 232 to *HV* 340, which, in turn, leads to an increase in the values of its static strength. The grain size is reduced to 70 μm.

It is shown that a decrease in the static strength and impact toughness of the HAZ metal of steel 06G2BDP at the cooling rate $w_{6/5}$ = 3 °C/s is predetermined by a significant grain growth (to 300 μm) and the formation of ferritic-pearlitic structure with fringes. An increase

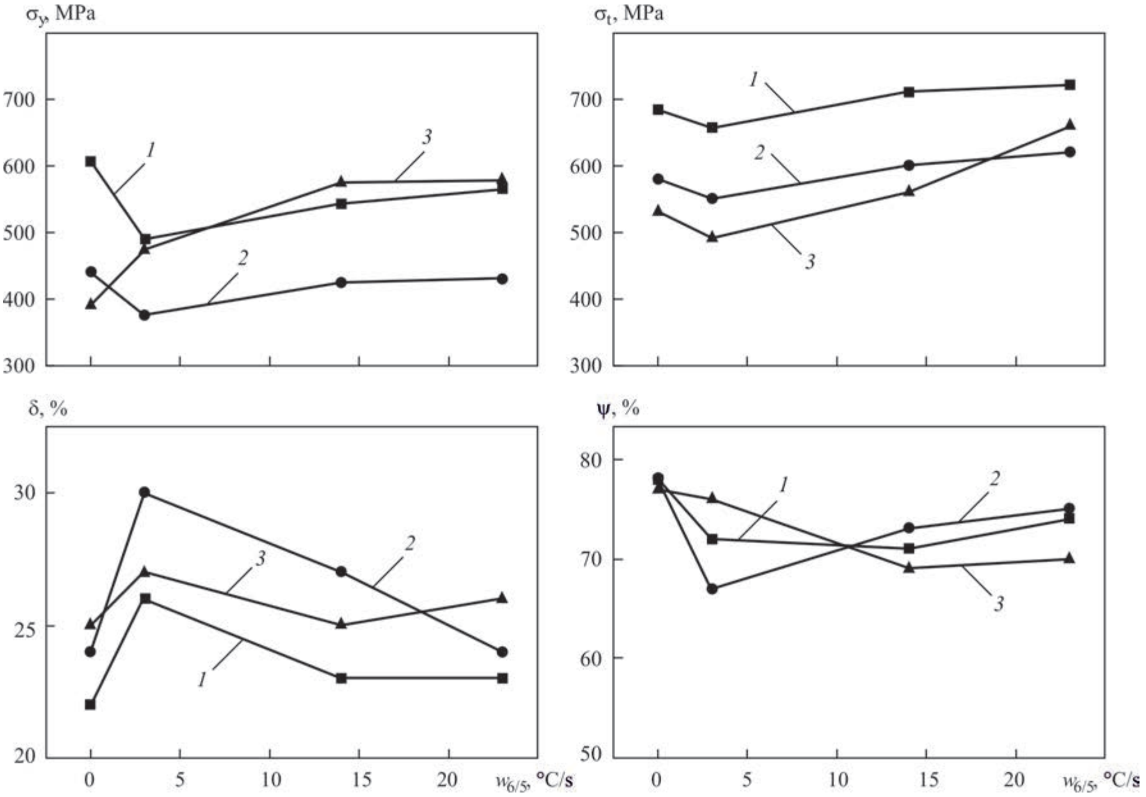

Figure 3. Mechanical properties of HAZ metal of the investigated steels depending on the value of cooling rate $w_{6/5}$: *1* — 06G2BDP; *2* — 06G2B; *3* — 10KhSND

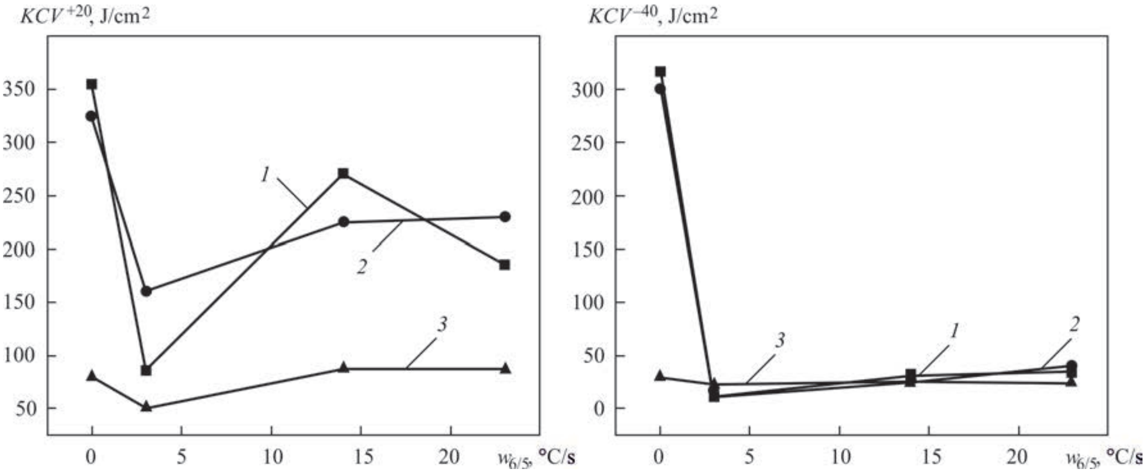

Figure 4. Impact toughness of the investigated steels depending on the value of cooling rate $w_{6/5}$: *1* — 06G2BDP; *2* — 06G2B; *3* — 10KhSND

in the cooling rate $w_{6/5}$ to 14 °C/s leads to a decrease in the average grain size to 100 μm, an increase in the specific share of upper bainite to 70 % and, as a consequence, to an increase in the values of static strength. However, the values of cold resistance (impact toughness at negative temperatures) are at the lower limit of admissibility. The latter fact is explained by a high content of upper bainite (30 %) in the produced structure.

Thus, taking into account the data obtained from the tests for corrosion resistance, steel 06G2BDP has higher characterisitcs than other investigated steels. Considering also that as to the values of static strength, ductility and toughness, steel 06G2BDP is not inferior to steel 06G2B and is superior to steel 10KhSND, its use is appropriate as an alternative to the mentioned steels in the manufacture of modern metal structures by gas-shielded manual arc and mechanized welding in the range of cooling rates of the HAZ metal typical to them.

Conclusions

The carried out investigations of the impact of thermal welding cycles on the structure and properties of steel 06G2BDP showed the following:

- at the cooling rate of the simulated HAZ metal $w_{6/5}$ = 3 °C/s (typical for submerged-arc welding processes), it is observed that the yield strength significantly decreases to 490 MPa and impact toughness drops to the values that do not meet the requirements of EuroNorm standards (less than 34 J/cm^2), which is predetermined by a significant increase in the grain size of the structure produced under such cooling conditions;
- it is possible to increase the value of static strength and impact toughness by the growth of the minimum cooling rate of the simulated HAZ metal $w_{6/5}$ to 14 °C/s. In this case, a structure with a grain size of about 100 μm is formed in the HAZ metal.

It was established that the optimal combination of the mechanical properties and structure can be achieved at the cooling rate of the HAZ metal of welded joints $w_{6/5}$ in the range from 14 to 23 °C/s.

The authors express their gratitude for assistance in carrying out the experiments to Dr. of Tech. Sci. Kostin V.A., Cand. of Tech. Sci. Olekseenko T.O. and Eng. Zhukov V.A.

1. Shymanovskyi, O.V. (2020) *Essays on problems of out of class bridges*. Kyiv, Stal [in Ukrainian].
2. Kovtunenko, V.A., Sineok, A.G., Gerasimenko, A.M., Zadorozhny, V.A. (2005) Typical damages of welded metal structures of bridges. *The Paton Welding J.*, **10**, 27–32.
3. Konyukhov, A.D. (1995) *Corrosion and reliability of railway equipment*. Moscow, Transport [in Russian].
4. Konyukhov, A.D. (2006) Rolled stock with improved properties for more effective bridge structures. *Stal*, **1**, 74–76 [in Russian].
5. Konyukhov, A.D., Ruvinskaya, E.M. (2002) Bridge spans from atmospheric-resistant steel. *Zashchita Metallov*, **1**, 89–95 [in Russian].
6. Zhang, B., Chen, W., Xu, J. (2018) Mechanical behavior of prefabricated composite box girders with corrugated steel webs under static loads. *J. of Bridge Engineering*, **1**, 23(10).
7. Wu, J., Yang, D., Su, Q. (2019) Inspection and evaluation strategy for uncoated weathering steel bridges. In:IOP Conference Series: *Materials Sci. and Engin.*, 677(**2**), 22–23. IOP Publishing.
8. Kovtunenko, V.A., Gerasimenko, A.M., Petruchenko, A.A. et al. (2007) Steel roll stock of improved atmosphere resistance for welded building structures. In: *Dorogy i Mosty, NDI*, **7**, 297–304 [in Russian].
9. Kovtunenko, V.A., Gerasimenko, A.M. Sineok, A.G. (2004) High-strength sparsely-alloyed steel 06G2B ≥ 440 MPa for bridge building. *Avtomobilni Dorogy i Dorozhnie Budivnytsvo*, **69**, 106–113 [in Russian].
10. Kovtunenko, V.A., Gerasimenko, A.M., Gotsulyak, A.A. (2006) Selection of steel for critical building welded structures. *The Paton Welding J.*, **11**, 27–31.
11. Sineok, A.G., Gerasimenko, A.M., Ryabokon, V.D. et al. (2014) Atmospheric-resistant rolled stock of c355–500 strength class for bridge metal structures. *Mosty i Tonneli: Teoriya, Issledovaniya, Praktika*, **5**, 83–91 [in Russian].

Received 26.08.2020

https://doi.org/10.37434/tpwj2020.09.03

FATIGUE LIFE OF SPECIMENS AFTER WEAR-RESISTANT, MANUFACTURING AND REPAIR SURFACING

I.O. Ryabtsev[1], **V.V. Knysh**[1], **A.A. Babinets**[1], **S.O. Solovej**[1] and **V.M. Demenkov**[2]
[1]E.O. Paton Electric Welding Institute of the NAS of Ukraine
11 Kazymyr Malevych Str., 03150, Kyiv, Ukraine. E-mail: office@paton.kiev.ua
[2]State Company «State Scientific and Technical Center for Nuclear and Radiation Safety»
35−37 Vasyl Stus Str., 03142, Kyiv, Ukraine. E-mail: vm_demenkov@sstc.com.ua

Cyclic fatigue life of specimens surfaced by flux-cored wire PP-Np-25Kh5FMS that provides a deposited metal of the type of tool semi-heat-resistant steel was studied. Design of the deposited specimens and procedure of their testing simulated the operating conditions of mill rolls, for surfacing of which flux-cored wire PP-Np-25Kh5FMS is widely used. Cyclic fatigue life of the specimens directly after surfacing, as well as the effectiveness of application of repair surfacing were evaluated to increase the residual cyclic fatigue life of the specimens, in which preliminary testing revealed fatigue cracks in the deposited wear-resistant layer. The numerical method was used to determine the stress-strain state and calculate the stress intensity factor on the front of a nonthrough corner fatigue crack that propagated in a specimen of 40Kh steel with a wear-resistant deposited layer at a three-point zero-to-load cyclic loading. It is shown that the maximum values of the stress intensity factor along the crack front are located at approximately 1 mm distance from the vertical side face in the deepest point of the crack front and during fracture they reach the value of 52−64 MPa√m. During investigations it was shown that application of repair surfacing to the products with fatigue cracks after their long-term service does not result in a significant extension of their cyclic fatigue life after repair. This is related to the fact that after long-term service the defect-free layer of the deposited metal has a considerable level of accumulated fatigue damages. That is why performance of repair of the product region damaged by a fatigue crack, is not effective without a complete removal of the deposited metal layer. The results obtained in this work will be further used as base ones during performance of comparative assessment of the impact of surfacing technique and technology, as well as surfacing materials, on the fatigue life of specimens. 17 Ref., 3 Tables, 9 Figures.

Keywords: arc surfacing, manufacturing surfacing, repair surfacing, fatigue, fatigue life, fatigue cracks, stress intensity factor

In metallurgy and mechanical engineering, tools and equipment for hot deformation of metals and alloys are widely used, which are exposed to cyclic mechanical and thermal loads during service. The examples of such heavy-loaded parts are different mill rolls, MCCB rollers, etc. Therefore, the problem of evaluation of fatigue life of such parts becomes particularly acute when it is necessary to evaluate the parts restored by different methods, including the methods of electric arc surfacing. [1−5].

Such parts have already passed a certain period of service and have exhausted a part of their life, specified during their designing and manufacture. After a series of subsequent repairs by surfacing methods, as a result of a nonuniform temperature distribution along the cross-section of a part, unfavorable residual tensile stresses are often formed in it [6-8]. In addition, the more times it was subjected to repairs and, accordingly, a bigger number of deposited layers it has the higher the probability of defects in the deposited metal in the form of lacks of fusion, slags, pores, etc. [4−10].

The most dangerous zones of mill rolls, in which cracks may appear, are the central areas, displaced from the axis of the roll towards variable total stresses having non-zero amplitude [5]. Also, an increased probability of crack formation and their higher growth rate are resulted by a decrease in the coefficient of asymmetry of the cycle and a significant range of the stress intensity factor (SIF) in the zone of the edge effect [5].

During service, all these factors negatively affect the overall fatigue life, which can lead to appearance and propagation of mechanical and fatigue cracks and, as a consequence, to the emergency fracture of parts.

Therefore, when developing the technology of repair surfacing of such parts, it is necessary to carefully evaluate the impact of preliminary service, chemical composition and properties of surfacing materials, as well as technological parameters of the arc surfacing process on the residual life of a restored part.

The aim of the work is to establish the fatigue life of the deposided specimens after manufacturing and repair surfacing, as well as to evaluate the impact of

I.O. Ryabtsev — https://orcid.org/0000-0001-7180-7782, V.V. Knysh — https://orcid.org/0000-0003-1289-4462
A.A. Babinets — https://orcid.org/0000-0003-4432-8879, S.O. Solovej — https://orcid.org/0000-0002-1126-5536
V.M. Demenkov — https://orcid.org/0000-0002-2000-0783

Table 1. Chemical composition of base and deposited metals, wt.% [11]

Grade of steel	C	Mn	Si	Cr	V	Mo	S	P
40Kh	0.36–0.40	0.5–0.8	0.17–0.37	0.8–1.1	–	–	≤0.035	≤0.035
PP-Np-25Kh5FMS*	0.20–0.32	0.5–1.0	0.80–1.30	4.6–5.8	0.2–0.6	0.9–1.5	≤0.04	≤0.04
4Kh5MFS**	0.32–0.40	0.2–0.5	0.90–1.20	4.5–5.5	0.3–0.5	1.2–1.5	≤0.04	≤0.04

Table 2. Mechanical properties of base and deposited metals [11]

Grade of steel	Mechanical properties (after normalization)					
	Conditional yield strength $\sigma_{0.2}$, MPa	Tensile strength σ_t, MPa	Relative elongation after rupture δ, %	Relative reduction in area after rupture ψ,%	Impact toughness *KCU*, J/cm^2, for specimens at t = 20 °C	Hardness
40Kh	345	590	12.5	52	7.5	*HB* 174–217
4Kh5MFS**	1570	1710	12	54	51	*HRC* 48–50

Notes to Tables 1 and 2:

*Presented mass fraction of elements in the deposited metal.

**In the literature there is no data on mechanical properties of metal deposited by the wire PP-Np-25Kh5FMS. Therefore, the data are presented for its analogue, which as to its chemical composition and properties is the closest to steel 4Kh5MFS.

the developed technology of repair surfacing on the overall life of a part.

Materials and methods of investigations. The choice of the type of base and deposited metal was grounded on the analysis of data from the technical literature: as the base metal in mill rolls, usually medium- and high-carbon non-alloyed or low-alloyed structural steels of such grades as 45, 50, 40 Kh, 50 Kh, 50KhN etc. are used. For surfacing of the working wear-resistant layer of mill rolls and other similar parts, electrode materials are most often used, such as heat-resistant or semi-heat-resistant steels, which provide producing a deposited layer. Such materials include flux-cored wires of grades PP-Np-25Kh5FMS, PP-Np-35V9Kh3SF, PP-Np-30Kh4V2M2FS, etc. [1, 3, 5].

Based on these data, for investigations as the base metal, steel 40Kh was chosen in the work. For surfacing the working layer, the flux-cored wire PP-Np-25Kh5FMS was used, which is widely applied in surfacing of mill rolls [8]. The chemical composition and mechanical properties of the materials used in the work are given in Tables 1 and 2.

At present, there is no single standardized procedure for fatigue tests of multilayer deposited specimens aimed at establishing their cyclic fatigue life. Most researchers use their own developed procedures that simulate the shape and features of specific parts the best [6, 10, 12, 13]. Taking into account a wide variety of parts operated under conditions of fatigue loading, such approach provides more reliable results. However, the abovementioned procedures do not allow evaluating the influence of surfacing materials and geometric dimensions of deposited specimens on their fatigue life. The authors [14, 15] proposed a procedure that allows correcting these drawbacks and can be successfully used for comparative evaluation of fatigue life of deposited parts, clearly demonstrating the influence of chemical composition of surfacing materials, deposited layers and surfacing scheme on the cyclic fatigue life of specimens.

The shape and dimensions of the deposited specimens for fatigue tests, the technology of their manufacture, as well as the testing procedure itself were chosen based on the calculations, recommendations and results of preliminary tests, which are given in [14, 15]. The tests according to this procedure reproduce the force loads, typical for mill rolls with a certain assumption, and in the course of tests allow carrying out a visual evaluation of the rate of fatigue crack propagation.

Taking into account the fact, that the authors of this work planned to carry out comprehensive investigations of fatigue life of parts deposited by different technologies using different materials of the main and intermediate layers. Therefore, to carry out a comparative evaluation of fatigue life of specimens after manufacturing and repair surfacing the developed procedure [14, 15] was used, having the improvements described below.

According to the surfacing technology described in [14, 15], 3 series of specimens were manufactured, 3 specimens in each series.

The first series of specimens was tested for fatigue until their complete fracture. The fatigue investigations were performed in the test servohydraulic machine URS-20 at three-point bending with a cycle asymmetry $R_\sigma = 0$ and a frequency of 5 Hz at a regular loading. The maximum stresses of the cycle were 500 MPa, and the distance between the supports was 250 mm.

On the second series of specimens cyclic crack resistance was evaluated. To initiate the propagation of a fatigue crack in the deposited metal in the center of the specimen (in the area of maximum applied stresses) a V-shaped notch with a depth of 1.0–1.5 mm with a radius of 0.25 mm was performed. After that, at a three-point cyclic bending with the maximum level of

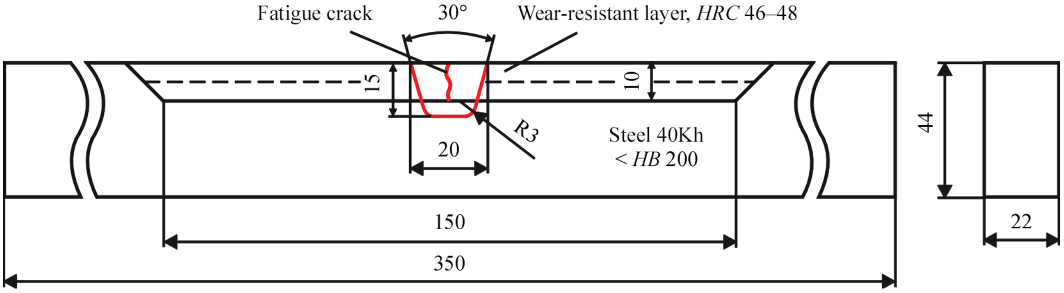

Figure 1. Scheme of preparation of metal damaged by fatigue cracks

applied stresses in the cross-section of the specimen of 300 MPa, a fatigue crack was grown until a length of 1 mm on one of the side faces. As a result, the produced notch with a crack was taken as the initial fatigue crack in the test specimen, which was then used to study the kinetics of fatigue fracture. When conducting fatigue tests for cyclic crack resistance, the length of a fatigue crack, which propagated on the side face of the specimen, was measured using an optical microscope with a graduating mark of 0.01 mm. The tests were performed until a complete fracture of the specimens.

In addition, for the specimens applying the numerical method based on the finite-element method (FEM), the stress-strain state was determined and the SIF was calculated on the crack front. The SIF is the main parameter of crack resistance and represents a quantitative evaluation of the stress field at the stage of arising fracture near the crack tip. The stress field at the crack tip has a singularity of the form $1/\sqrt{r}$, where r is the distance from the crack tip to the point where stresses are considered [16].

Determination of these characteristics for specimens made applying the abovementioned technology, and for the specimens made later by other technologies, will allow carrying out a comparative evaluation of their cyclic crack resistance, where the values obtained in this work will act as basic values.

On the specimens of the third series the efficiency of repair surfacing was investigated to increase the residual cyclic fatigue life of specimens, having fatigue cracks in the deposited wear-resistant layer. The specimens were tested for fatigue at a three-point bending with the asymmetry of the cycle $R_\sigma = 0$ until the formation of a fatigue crack with a depth of 10–12 mm (when the crack passed through the deposited layers and deepened into the base metal) (Figure 1). After that, repair was carried out applying arc surfacing methods, which consisted of a complete mechanical removal of a fatigue crack, the metal around it and the subsequent filling of the formed groove (Figure 2).

The depth and width of the groove, as well as the lateral radii were selected according to the maximum length of fatigue cracks, as well as according to practical recommendations to produce a quality deposided joint under the flux layer for the corresponding metal thickness. The development of such sizes and shape allows preventing jamming of the slag crust, which could result in the formation of slags, which, in turn, can reduce mechanical properties of the deposited metal, acting as stress concentrators.

After mechanical treatment, the specimens with a groove for repair surfacing (Figure 2, *a*) were collected in a package (3 pcs), laying by two technological inserts between the specimens with a thickness of 3 mm each. From both free edges, to the specimens run-on plates were attached (Figure 2, *b*).

Before surfacing, preliminary heating of packages of billets to 250–300 °C was carried out. After that, automatic arc surfacing of the wear-resistant layer was performed using the flux-cored wire PP-Np-25Kh5FMS with a diameter of 1.8 mm under the flux AN-26P.

The surfacing mode for all the specimens was the same: $I = 220–250$ A; $U = 26–28$ V; $v = 18$ m/h; overlap of the beads ≈ 50 %. After surfacing, the speci-

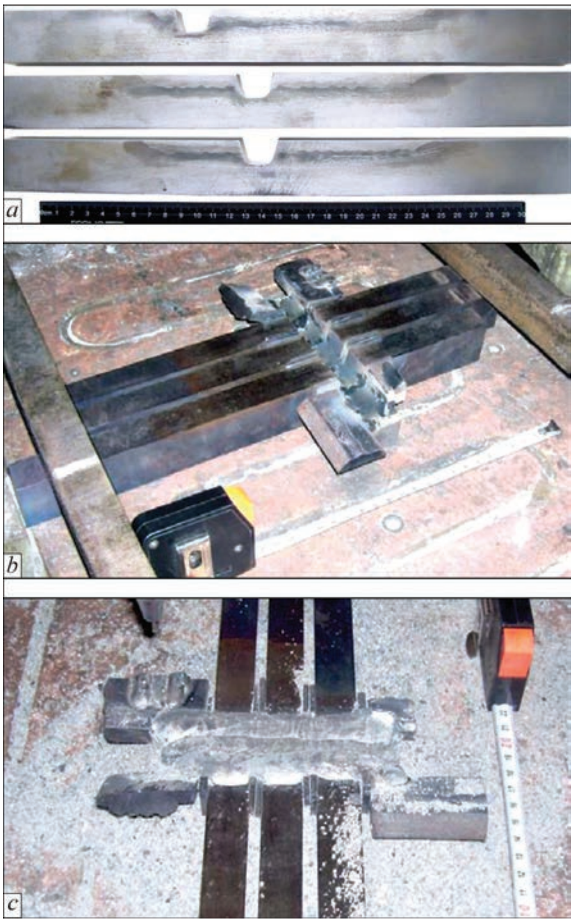

Figure 2. Appearance of billets with preparation for repair surfacing (*a*), assembled into a package before (*b*) and after repair surfacing (*c*)

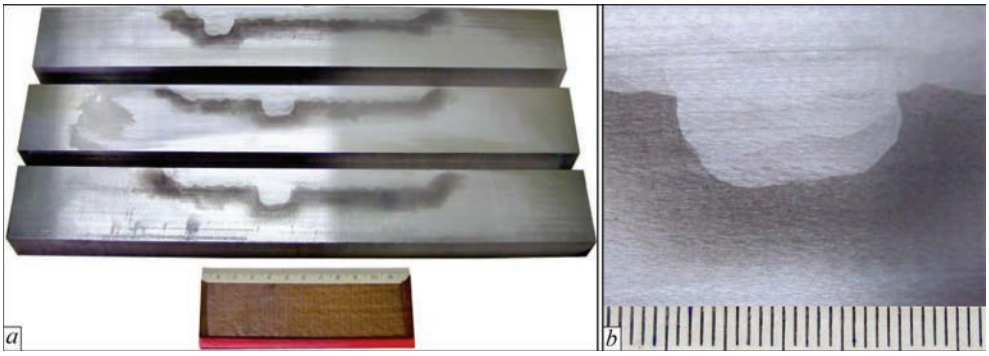

Figure 3. Appearance of specimens after grinding (*a*) and area of repair surfacing (*b*)

mens were placed in a thermal oven heated to 250 °C for slow cooling together with it. Such measures were aimed at reducing residual stresses in the deposited specimens and the probability of cracking.

After a complete cooling, the package of repaired specimens was cut with the help of abrasive discs on technological inserts into separate specimens, which were finally treated by grinding on four sides (Figure 3) and again were installed in the test machine.

Before the fatigue test, in the specimens repaired by surfacing, residual stresses were measured by the nondestructive acoustic method using a portable ultrasonic stress control device [17]. Ultrasonic quartz sensors of longitudinal and shear waves with a measurement base of 7×7 mm were used.

Discussion of results. The fatigue tests of the first series of specimens showed that their cyclic fatigue life before fracture at maximum applied stresses of 500 MPa is in the range from 560800 to 1420100 cycles of stress changes.

A preliminary visual inspection of the specimens with ×10 magnification showed that fatigue cracks mainly appear near the fusion zone of two adjacent beads, which can be explained by an increase in the level of chemical and structural heterogeneity in that zone [5]. In this case, a crack usually propagates almost rectilinearly, parallel to the direction of the applied load with small lateral branches. Moreover, it is noted that in the «channel» of the crack some bends and short tears are observed (Figure 4). Subsequently, the areas of metal with fatigue cracks were cut out and microsections were made. The investigations of microsections showed that fatigue cracks are mainly formed and propagated near the zones of overlaps of adjacent deposited beads, propagating in the direction of the axes of dendrites formation (Figure 5).

Therefore, it was found that the type and the nature of formation and further propagation of fatigue cracks depends on the technique and technology of surfacing, in particular, on the step during surfacing of adjacent beads. Moreover, the fusion line of the base and deposited metals, as well as the nature of the fusion line of separate beads and layers play an important role in the process of fatigue fracture of deposited parts, because cracks mostly propagate either along the fusion boundary of separate beads, or directly near this boundary, where the zone of chemical and structural heterogeneity is probably located, which negatively affects the fatigue life.

On the specimens of the second series during experimental investigations of crack resistance, the dependence of fatigue crack (depth) propagation on the corresponding number of cycles of variable load *N* was determined. After initiation, all fatigue cracks propagated as non-through (corner) ones from one of the edges of the specimen. Therefore, in addition to the crack depth along the vertical side face of the spec-

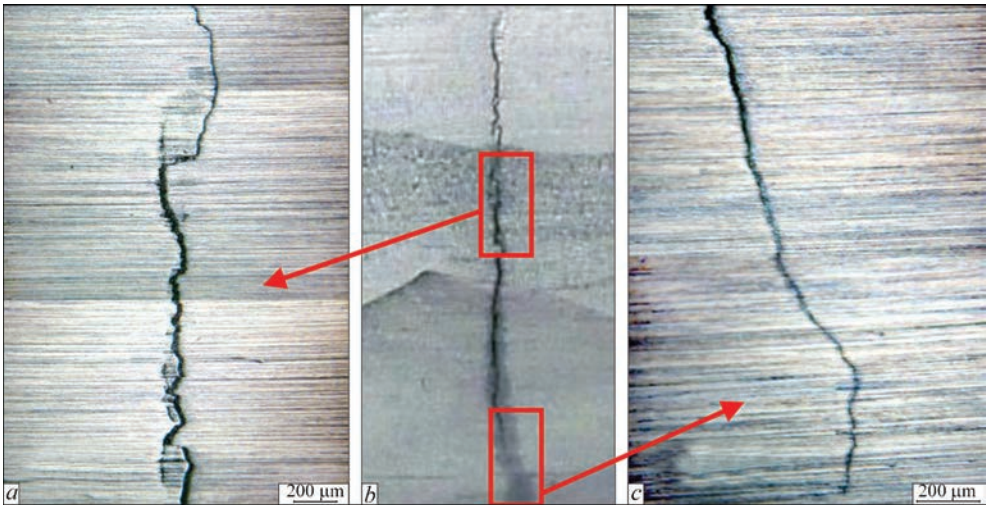

Figure 4. Nature of propagation of fatigue cracks in deposited specimens

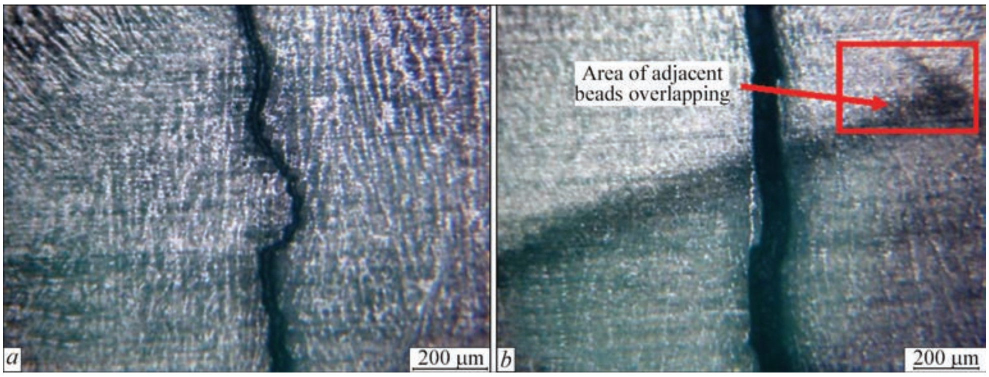

Figure 5. Nature of propagation of fatigue cracks in deposited metal. Magnification ×50

imen, the crack length at the bottom of the V-shaped notch was also measured using a caliper with a graduating mark of 0.1 mm. The fracture of the specimens during three-point cyclic bending with a maximum level of applied stresses of 300 MPa occurred when the cracks reached the dimensions (depth×length): 23.6×16.4, 12×14 and 14×16 mm.

Using numerical method based on FEM, the stress-strain state (Figure 6) was determined and calculation of SIF along the crack front (Figure 7) was carried out. Figure 6 shows the stress-strain state in the model specimen at the beginning of fatigue fracture (crack size of 6×4 mm, Figure 6, *a*) and when the crack reaches its critical value 23.6×16.4 (Figure 6, *b*).

Figure 7 shows the data of change in SIF values along the crack front (zero value on the abscissa axis corresponds to the beginning of the crack on the vertical side face of the specimen) as the corner crack propagates in the two specimens of the second series. The construction of a finite-element model of the specimen and the subsequent SIF calculations were performed by means of the software package ANSYS Workbench 2019R3. The calculation CE-grid consisted of 20 nodal hexagonal elements and of 15 nodal prismatic elements directly along the crack front. In the area of the crack front, a grid with a concentric arrangement of elements was built, which consisted of 16 layers of elements in the radial and 48 layers in the circumferential directions, which uniformly surrounded the crack front. This allowed solving the problem of fracture mechanics with the required accuracy.

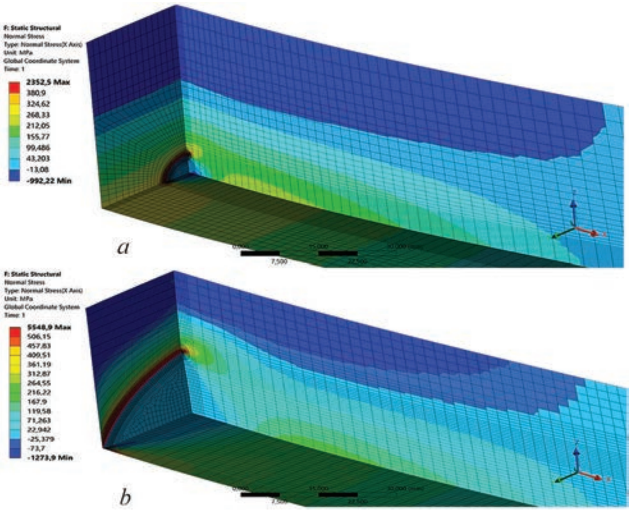

Figure 6. Results of calculation of stress-strain state for cracks with the sizes of 6×4 (*a*) and 23.6×16.4 mm (*b*)

It was established that the maximum values of SIF along the crack front are at a distance of about 1 mm from the vertical side face at the deepest point of the crack front and during fracture they reach the value of 52–64 MPa√m.

On the specimens of the third series, after performing repair surfacing, residual stresses were measured by nondestructive ultrasonic method using the de-

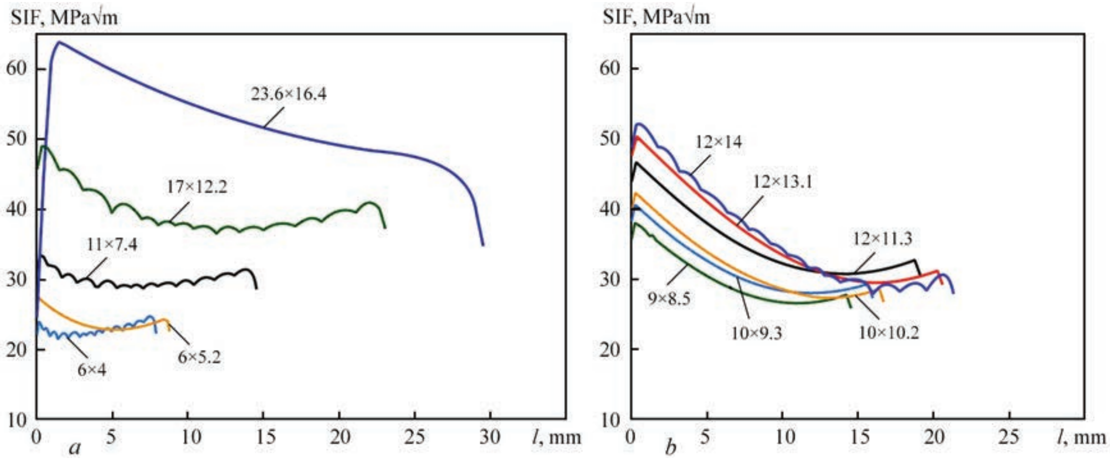

Figure 7. Values of SIF on the crack front as it propagates in the first (*a*) and the second (*b*) specimens of the second series

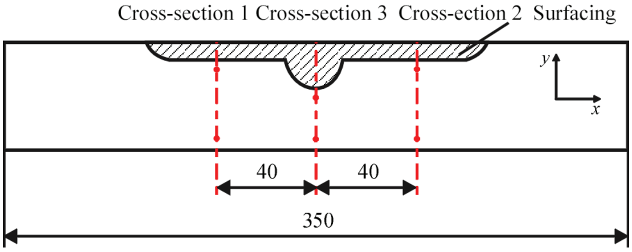

Figure 8. Schematic representation of places of measuring residual stresses in the specimen after repair surfacing

veloped technology. Schematic representation of the places of measurement of residual stresses is given in Figure 8, and diagrams of the distribution of residual stresses are in Figure 9. The measurements of residual stresses oriented along and across the specimen were performed from the fusion line (determined by the macrostructure) deep into the metal. The values of residual stresses given on the diagrams are averaged over the thickness of the specimen.

The use of ultrasonic quartz sensors of longitudinal and shear waves with a measurement base of 7×7 mm did not allow performing the measurement of stresses closer than 2.5 mm to the fusion line. However, the study of residual fields σ_x oriented along the specimen (coincide in direction with the applied operating stresses during tests of the specimens on fatigue) showed that the zone of residual tensile stresses after repair surfacing does not exceed 6–7 mm from the fusion line deep into the base metal. The maximum residual tensile stresses σ_x are located directly in the area of repair surfacing and amount to about 120 MPa at a distance of 2.5 mm from the fusion line (Figure 9, *b*). In the course of moving away from the place of repair surfacing, the residual tensile stresses σ_x at a distance of 2.5 mm from the fusion line are reduced to 40–80 MPa (Figure 9, *a*, *c*). Starting from a distance of 6–7 mm from the fusion line deep into the metal, a zone of residual compressive stresses is formed, which reach the values of up to −60– −80 MPa. These data will also be used as a basis for further comparative investigations of fatigue life of specimens deposited by other technologies.

After measuring the residual stresses, the specimens of the third series were subjected to fatigue tests. The results of fatigue tests of specimens of the third series before and after repair surfacing are given in Table 3.

A preliminary fatigue crack initiation in the specimen No.8 (Table 3) occurred inside the specimen at a distance of 8 mm from the surface (near the fusion line with the base metal) as a result of a lack of fusion between the beads. At the same time, elimination of fatigue cracks by repair surfacing, the occurrence of which is caused by casual technological defects in a preliminary deposited layer, does not lead to a decrease in life as compared to defect-free surfacing. After repair surfacing, the initiation and propagation of fatigue cracks in all specimens of the third series took place at a far distance from the place of repair. Fatigue tests of the specimens of the third series showed that a total cyclic fatigue life of the specimens at maximum applied stresses of 500 MPa is in the range from 1154000 to 1651700 cycles of stress changes.

It is also shown (specimen No.9, Table 3) that application of repair surfacing to the products with fatigue cracks after their long service does not lead to a significant increase in cyclic fatigue life after repair.

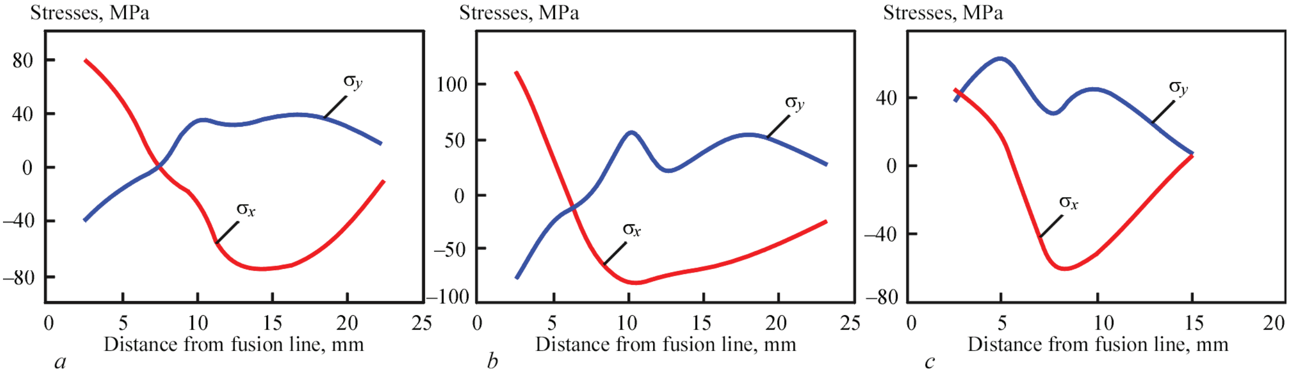

Figure 9. Distribution of residual stresses oriented along σ_x and across σ_y of the specimen after repair surfacing in the cross-section 1 (*a*), cross-section 2 (*b*) and cross-section 3 (*c*)

Table 3. Results of fatigue tests of specimens of the third series

Number of specimen	Maximum cycle stresses, MPa	Cyclic fatigue life before formation of a crack of 10 mm, cycles	Cyclic fatigue life after repair surfacing, cycles	Total cyclic fatigue life, cycles
7	500	688700	963000	1651700
8	500	132800*	1021200	1154000
9	500	1381800	128000	1509800
*Defect in the form of lack of fusion between the beads.				

This is associated with the fact that after long-term service, the defect-free layer of deposited metal has a significant level of accumulated fatigue damages and that is the reason why repairing of the area of a product damaged by a fatigue crack is inefficient without a complete removal of the deposited metal layer. Therefore, repairing products after long-term service in order to significantly increase the overall life, it is recommended to remove not only the metal around the revealed fatigue cracks, but the whole deposited layer to the depth of the revealed fatigue cracks with a subsequent restoration surfacing.

Conclusions

1. Design of the deposited specimens and procedure of comparative investigations of their fatigue life were improved, as well as the basic fatigue characteristics of the deposited specimen, simulating the design of mill rolls, were established.

2. It was established that the type and the nature of formation and further propagation of fatigue cracks in the deposited specimens depend on the technique and technology of surfacing, in particular, on the step during surfacing of adjacent beads. In addition, the fusion line of the base and deposited metals, as well as the nature of the fusion line of particular beads and layers plays an important role in the process of fatigue fracture of deposited parts, because cracks mostly propagate either along the fusion boundary of separate beads, or directly near this boundary, where, probably, the zone of chemical and structural heterogeneity is located, which negatively affects the fatigue life.

3. Using the numerical method based on FEM, the SIF values were determined along the front of the non-through corner fatigue crack, which propagated in a prismatic model specimen of 40Kh steel with a wear-resistant deposited metal layer at a three-point repeating cyclic bending. It was established that the maximum values of SIF along the crack front are located at a distance of about 1 mm from the vertical side face at the deepest point of the crack front and during fracture they reach the value of 52−64 MPa√m.

4. It was experimentally established that at the early stages of service of a product the elimination of fatigue cracks by repair surfacing, the appearance of which is caused by random technological defects in the preliminary deposited layer, does not lead to a decrease in the life as compared to defect-free surfacing.

5. It was shown that application of repair surfacing to the products with fatigue cracks after their long-term service does not lead to a significant increase in the cyclic fatigue life after repair. This is associated with the fact that after long-term service, the defect-free layer of deposited metal has a significant level of accumulated fatigue damages. Therefore, the repair of a product damaged by a fatigue crack without a complete removal of the deposited metal layer is not effective enough.

1. Gao, F., Zhou, J., Zhou, J. et al. (2017) Microstructure and properties of surfacing layers of dies manufactured by bimetal-gradient-layer surfacing technology before and after service. *The Int. J. Adv. Manuf. Technol.*, **88**, 1289–1297. doi:10.1007/s00170-016-8679-0
2. Zhang, J., Zhou, J., Tao, Y. et al. (2015) The microstructure and properties change of dies manufactured by bimetal-gradient-layer surfacing technology. *Ibid.*, **80**, 1807–1814. doi:10.1007/s00170-015-7170-7
3. Ahn, D.-G. (2013) Hardfacing technologies for improvement of wear characteristics of hot working tools: A review. *Int. J. of Precision Engineering and Manufacturing*, 14(**7**), 1271–1283. doi:10.1007/s12541-013-0174-z
4. Jhavar, S., Paul, C.P., Jain, N.K. (2013) Causes of failure and repairing options for dies and molds: A review. *Engineering Failure Analysis*, **34**, 519–535. DOI: 10.1016/j.engfailanal.2013.09.006
5. 5. Du, Toit, M., Van, Niekerk J. (2010) Improving the life of continuous casting rolls through submerged arc cladding with nitrogen-alloyed martensitic stainless steel. *Welding in the World*, 54(**11–12**), 342–349. doi:10.1007/bf03266748
6. Shao, C., Cui, H., Lu, F., Li, Z. (2019) Quantitative relationship between weld defect characteristic and fatigue crack initiation life for high-cycle fatigue property. *Int. J. of Fatigue*, **123**, 238–247. doi:10.1016/j.ijfatigue.2019.02.028
7. 7. Korotkov, V.A. (2017) More efficient surfacing. *Russian Engineering Research*, **37**, 701–703. doi:10.3103/S1068798X17080093
8. Rjabcev, I.A., Senchenkov, I.K., Turyk, Je.V. (2015) *Surfacing. Materials, technologies, mathematical modeling*. Gliwice, Wydawnictwo politechniki slaskiej [in Russian].
9. Liu, H., Yang, S., Xie, C. et al. (2018) Mechanisms of fatigue crack initiation and propagation in 6005A CMT welded joint. *J. of Alloys and Compounds*, **741**, 188–196. doi:10.1016/j.jallcom.2017.12.374
10. Zerbst, U., Madia, M., Beier, H. T. (2017) Fatigue strength and life determination of weldments based on fracture mechanics. *Procedia Structural Integrity*, **7**, 407–414. doi:10.1016/j.prostr.2017.11.106
11. Oberg, E. et al. (1996) *Machinery's Handbook* (25th ed.), Industrial Press Inc.
12. Zhang, D., Liu, Y., Yin, Y. (2016) Preparation of plasma cladding gradient wear-resistant layer and study on its impact fatigue properties. *J. Thermal Spray Technol.*, **25**, 535–545. doi:10.1007/s11666-015-0370-8
13. Ganesh, P., Moitra, A., Tiwari, P. et al. (2010) Fracture behavior of laser-clad joint of Stellite 21 on AISI 316L stainless steel. *Mater. Sci. & Engin.*, 527 (**16–17**), 3748–3756. doi:10.1016/j.msea.2010.03.017
14. Babinets, A.A., Ryabtsev, I.A. (2016) Fatigue life of multilayer hard-faced specimens. *Welding Int.*, 30(**4**), 305–309. https://doi.org/10.1080/01431161.2015.1058004
15. 15. Ryabtsev, I.A., Knysh, V.V., Babinets, A.A. et al. (2019) Methods and specimens for comparative investigations of fatigue resistance of parts with multilayer surfacing. *The Paton Welding J.*, **2**, 29–34. https://doi.org/10.15407/tpwj2019.02.05
16. Murakami, Yu. (1990) *Reference book on stress intensity coefficients*. In: 2 Vol. Moscow, Mir [in Russian].
17. (2004) *Device for control of mechanical stresses and strains in solid media*. Pat. UA 71637 C2 [in Ukrainian].

Received 24.07.2020

https://doi.org/10.37434/tpwj2020.09.04

EFFECT OF LOCAL HEAT TREATMENT ON MECHANICAL PROPERTIES OF WELDED JOINTS OF INTERMETALLIC OF TiAl SYSTEM PRODUCED BY ELECTRON BEAM WELDING

L.M. Lobanov, E.A. Asnis, N.V. Piskun, E.L. Vrzhyzhevskyi and **L.M. Radchenko**
E.O. Paton Electric Welding Institute of the NAS of Ukraine
11 Kazymyr Malevych Str., 03150, Kyiv, Ukraine. E-mail: office@paton.kiev.ua

Welded joints of intermetallic β-stabilized alloy TiAl–Ti–44Al–5Nb–3Cr–1.5Zr (at.%) were investigated. Intermetallic billets of 3 and 10 mm thickness were welded by electron beam welding. In order to prevent arising of cold cracks in welded joints of titanium aluminide specimens of different thickness, the following postweld local heat treatment using an electron beam was performed. The mentioned method of treatment is one of the most attractive to improve the structure of ingot and reduce the level of residual welding stresses, which, in its turn, significantly increases mechanical properties of the alloy. Static tensile tests were performed to evaluate the strength of welded joints. The specimens fractured throughout the base material. The paper presents histograms showing the values of tensile strength (σ_t) of welded joints produced during tensile tests for the specimens of different thickness with and without the use of local heat treatment (LHT). It is shown that the use of local heat treatment increases tensile strength of the specimens of 3 and 10 mm thickness, as compared to the specimens produced without LHT. In addition, the values of this index for welded joints of different thicknesses, which are produced using this technique, are quite uniform. Comparative analysis of the results of tensile tests and the results of microhardness studies was performed, which showed that fracture of the specimens took place in the zone of lowering mechanical properties. The nature of fractures of different parts of welded joint was studied, which confirmed that fracture occurs in the zone of brittle part of the specimen. It is known that mechanical properties of welded joint are closely related to its structural state. During local heat treatment, an additional β_0 (B2) phase appears in the structure, which increases the ductility of the weld material, 14 Ref., 2 Tables, 9 Figures.

Keywords: intermetallic alloy of TiAl system, electron beam welding, local heat treatment, mechanical tensile tests, tensile strength, structural state, microhardness

Intermetallics are used to manufacture a wide range of products for aircrafts. In the manufacture of a number of assemblies of high and low pressure turbines, it is advisable to use welding [1].

One of the most important problems of modern metals science is to increase the level of mechanical properties of titanium alloys, as well as welded joints and assemblies, which are now widely used for manufacture of parts of gas turbine engine (GTE).

Thus, optimization of properties and development of technologies for welding structural intermetallic of the titanium-aluminium system for the further use is quite relevant.

One of the most suitable ways to produce high-quality intermetallic joint is electron beam welding (EBW), which allows welding products of different geometric shapes, producing welds of different length, as well as intermittent welds. As compared to other types of fusion welding, electron beam welding also has advantages: first, because it is carried out in a high vacuum, it provides a protection of such active material as titanium; secondly, during EBW a narrow weld and a very negligible heat-affected zone are formed that, in turn, should lead to minimum deformations of a welded joint [2, 3].

While producing welded joints of intermetallics of TiAl system applying EBW method, their significant defect is cold cracks, arising at the temperatures below 700 °C, when the material changes from tough to brittle state [4, 5]. A low ductility of welded joint at the state after welding, in turn, is determined by the unfavourable structure of welded joint and, with an increase in welding stresses during cooling, it leads to the appearance of cold cracks [6–8].

In order to struggle cracks, it is necessary to provide a slow cooling rate [9]. At the same time the temperature gradient and, accordingly, the level of stressed state are reduced, which is an important factor in struggling crack formation. At the same time, the ductility of welded joint is improved as a result of favourable structural transformations.

L.M. Lobanov — https://orcid.org/0000-0001-9296-2335, E.A. Asnis — https://orcid.org/-0000-0002-4697-8202,
N.V. Piskun — https://orcid.org/-0000-0003-1459-2310, E.L. Vrzhyzhevskyi — https://orcid.org/0000-0001-8651-8510

The most important task of increasing reliability of aircraft and gas turbine engines is to prevent danger of fracture of the most critical structural elements. The rigidity of the requirements to the serviceability of welded structures of critical purpose, manufactured based on titanium alloys, can be satisfied by a high quality of welded joints. The challenging direction of investigation is to increase the mechanical properties of welded joint to the level not lower than the properties of the initial material by preventing the formation of macro- and microcracks, porosity in the weld and near-weld zone.

Electron beam welding with the subsequent local heat treatment. Experiments on EBW and investigations of welded joints of intermetallic alloy Ti–44A1–5Nb–3Cr–1.5Zr (at.%) were carried out on the specimens with a thickness of 3 and 10 mm. The thickness of the specimens for testing welding modes was chosen based on the fact that thicknesses $\delta = 3$ mm can be used in welded assemblies of GTE of high and low pressure, and the choice of 10 mm was justified by the fact that such thicknesses are used for compressor blades of aircraft engines.

The specimens were welded with preheating on the following mode: $T_{preheat} = 450$ °C; $U_{acc} = 60$ kV; $V_w = 7$ mm/s; $P = 5\cdot10^{-3}$; $I_b = 35$ mA (for a thickness $\delta = 3$ mm) and $I_b = 90$ mA (for a thickness $\delta = 10$ mm). The produced specimens had transverse cracks that passed through the weld.

With the help of calculation methods, the thermal conditions were determined which lead to the formation of cold cracks. Investigations of the stress state of welded joints, as well as the processes of structure formation occurring in EBW were carried out. As a result of generalization of these investigations, it was shown that in addition to preheating, local heat treatment (LHT) should be performed immediately after welding. For this purpose, the most rational is the use of capabilities of the electron beam. Local heat treatment by scanning the beam along the weld immediately after welding will reduce the rate of increase of temporary stresses during welding and the level of residual welding stresses, which will reduce the probability of crack formation.

Technology of EBW of intermetallic Ti–44Al–5Nb–3Cr–1.5Zr (at.%) with the subsequent LHT, which occurs right after the completion of welding process, was developed, providing the rate of cooling welded joint in the range of 0.7–0.9 °C/s. The electron beam is defocused from 2 mm in welding with a diameter of up to 15 mm during heat treatment, and the welding current is reduced by 1/3, which allows maintaining the level of temperature of welded joint at 1000 °C during 5 min. The application of the proposed LHT method allowed reducing the level of residual welding stresses and, due to that, avoiding the formation of cracks in the weld on the material with a thickness of 10 mm [10].

For the plates with a thickness of 3 mm, the modes of controlled cooling were proposed that allow compensating for excessive surface heat transfer. Using this technology, it is recommended to carry out heat treatment with a defocused and deployed electron beam with a gradual decrease in its power and, namely, immediately after the completion of welding, the electron gun should be placed in the middle of the weld and the beam should be deployed to the desired configuration on one and the other side from the middle of the weld to its end with the use of a special computer program. The scanning frequency of the electron beam is 100 Hz, and the welding current is reduced by 1/3. The total time of the specified heat treatment is 10 min. The temperature of the welded joint of 1000 °C is maintained during 5 min. Then, due to a slow (~ 5 min) reduction in current according to a special program, the welded joint is cooled to a temperature of 500 °C [11].

The use of local heat treatment allowed reducing the welding residual stresses by almost 30% - from 225 to 160 MPa. This made it possible to avoid the appearance of cold cracks and produce defect-free joints.

Investigation of mechanical properties of welded joints. To evaluate the strength of welded joints, static tensile tests were performed. The tests were

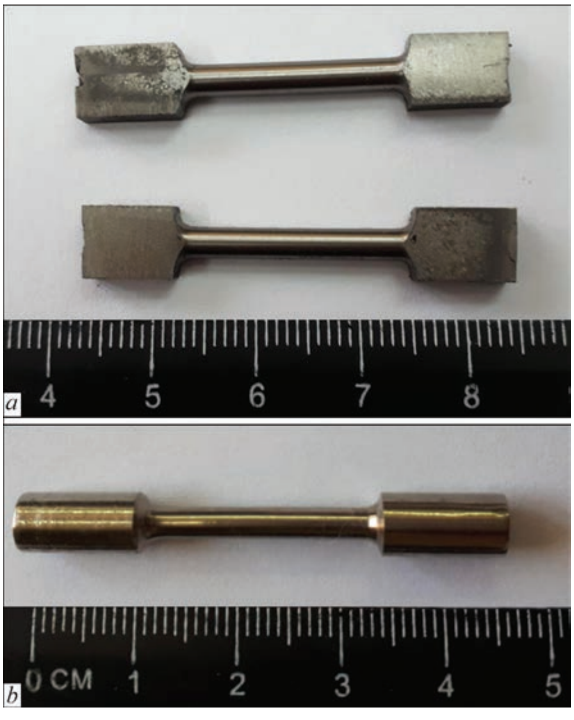

Figure 1. Appearance of intermetallic specimen, made for mechanical tests: *a* — thickness 3; *b* — 10 mm

Figure 2. Intermetallic specimens after tensile test: *a* — thickness 3; *b* — 10 mm

performed according to GOST 1497–84 in the rupture machine ZD-4.

To carry out tests, the specimens MI-12 were prepared.

Figure 1 shows the appearance of the specimens manufactured for tensile tests.

Fracture of the specimens occurred on the base material.

Figure 2 shows the specimens of intermetallic of a cylindrical shape after tensile tests.

Figure 3 shows a typical tensile diagram of a welded joint of intermetallic of 3 and 10 mm thickness, produced by EBW with LHT.

The results of mechanical tests of welded joints of the specimens produced during tensile tests are given in Table 1.

Table 1. Tensile strength of welded joints

Specimen number	Thickness δ, mm	Value σ_t MPa	Place of fracture
1	3	310.9	BM
2	3	319.1	Same
3	10	343.8	»
4	10	337.4	»
5	10	346.6	»
Average value: δ = 3 mm δ = 10 mm		315.0 342.6	

Table 2. Tensile strength of welded joints of intermetallic, produced by EBW method without LHT

Specimen number	Thickness δ, mm	Value σ_t MPa	Place of fracture
1	3	197.8	BM
2	3	152.1	Same
3	3	175.5	»
Average value		175.13	

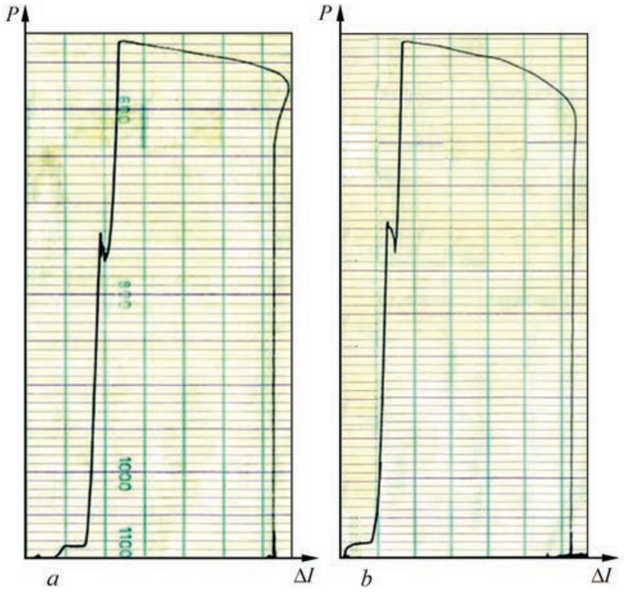

Figure 3. Diagram of tensile tests of welded joints: *a* — thickness 3; *b* — 10 mm

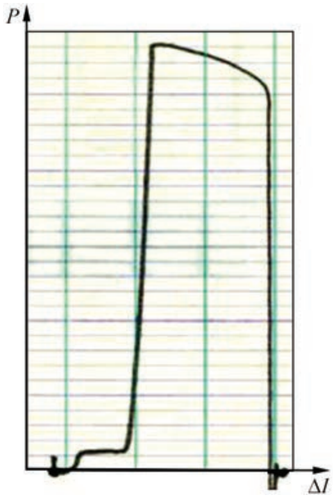

Figure 4. Diagram of tensile tests of 3 mm thick welded joints produced by EBW method without LHT

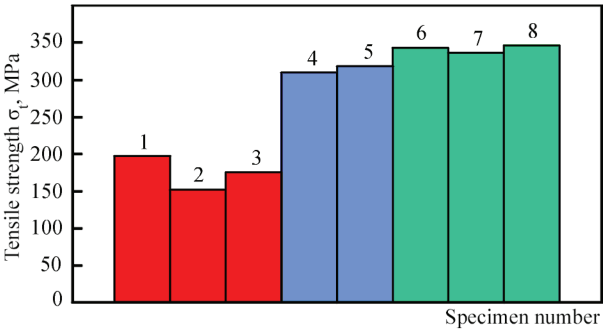

Figure 5. Value of tensile strength of welded joints of intermetallic produced during tensile test: 1–3 — produced by EBW without LHT (δ = 3 mm); 4, 5 — produced by EBW with the subsequent LHT (δ = 3 mm); 6–8 — produced by EBW with the subsequent LHT (δ = 10 mm)

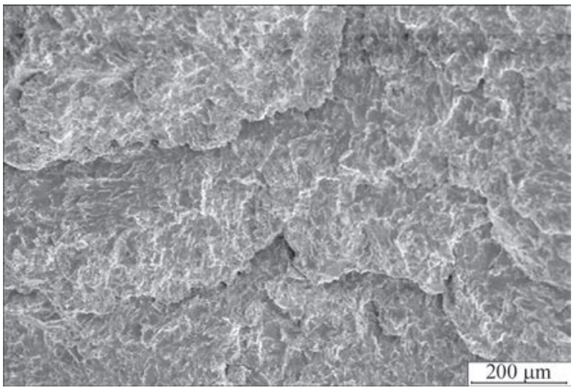

Figure 6. Fractogram of fracture surface of initial metal of titanium intermetallic of TiAl system using LHT

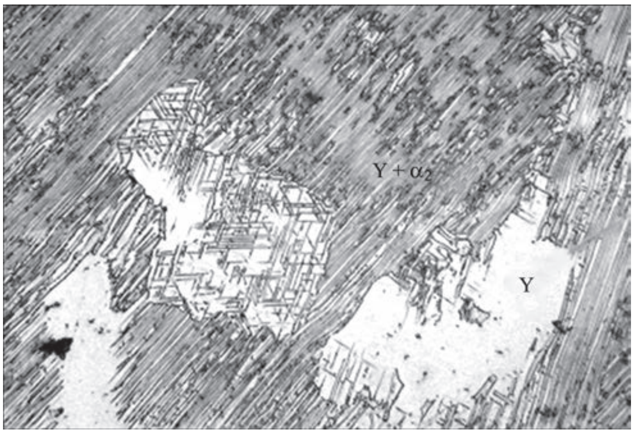

Figure 8. Microstructure (×500) of weld, produced without LHT

For comparison, mechanical tests of welded joints of the specimens produced by EBW without LHT were performed. Table 2 shows the results of tests.

Figure 4 shows a typical tensile diagram of 3 mm thick welded joint of the intermetallic produced by EBW without LHT.

Figure 5 shows histograms with the values of tensile strength (σ_t) of welded joints, produced during tensile tests for the specimens of different thickness with and without LHT.

As is seen from the histograms, the values of tensile strength of the specimens with a thickness of 3 and 10 mm, welded using postweld local heat treatment, is much higher than for the specimens produced without LHT and is sufficiently uniform for the specimens of different thicknesses.

Measurements of microhardness of welded joints showed that in the area of the base metal a decrease in microhardness to 3570 MPa occurs as compared to the weld having a microhardness of about 5430 and HAZ, which has a microhardness of 4810 MPa.

Thus, the results of measurements of microhardness of welded specimens correlate with the results of strength of the welded joint after the fracture of all specimens — the fracture of the specimens occurred approximately in the zone of reduction of mechanical properties.

The nature of fractures of different parts of the welded joint was studied. Figure 6 shows a fractogram of the fracture surface of the welded joint in the area of the base material. It is seen that step fracture is observed in the areas of the base material. The steps move in a one direction parallel to each other. This type of fracture is characteristic of brittle fracture.

The fractures of welded joints of titanium aluminide, which were welded using postweld LHT, have a mixed nature of fracture (with ~ 30 % of a tough component).

Fractographic examinations (Figure 7) confirmed that fracture occurs in the area of a brittle part of the specimen.

Analysis of the data obtained during the test showed that the specimens welded with the subsequent LHT have the highest values of tensile strength.

The fracture not along the welded joint is always treated as a sign of a high quality of welding [12–14].

Since mechanical properties of the welded joint are closely related to its structural state, it is necessary to conduct a comparative analysis of metallograph-

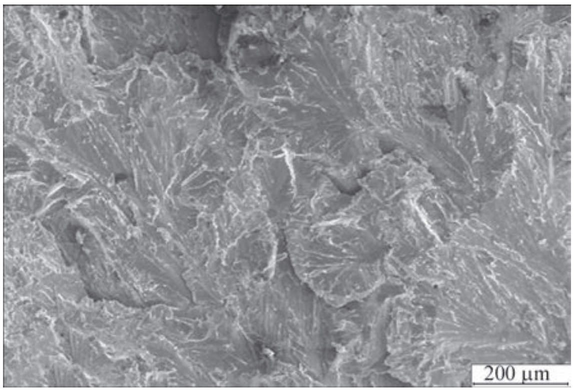

Figure 7. Fractogram of fracture surface of initial metal of titanium intermetallic of TiAl system, area of weld metal (×200)

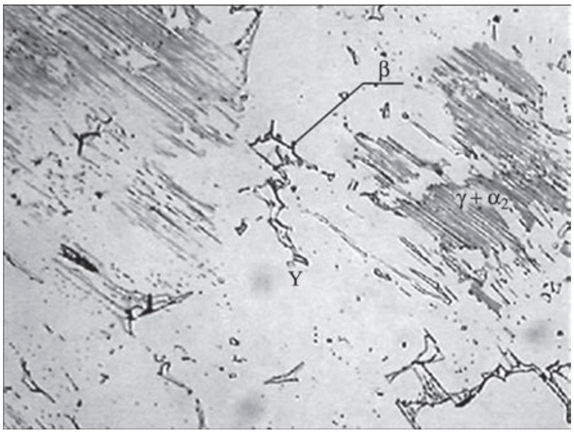

Figure 9. Microstructure (×500) of area of base metal of welded joint of titanium aluminide, produced by EBW with the subsequent LHT

ic examinations with mechanical characteristics. The weld produced by EBW without a further heat treatment has a two-component structure consisting of γ and α_2-phases (Figure 8), and the use of LHT facilitates a reduction in the cooling rate of the weld and the formation of β-phase (Figure 9), which is responsible for increase in the ductility and strength of the welded joint.

This structural difference of welded joints, produced with the subsequent postweld heat treatment, has a positive effect on the level of strength during mechanical tests and, namely, allows increasing the tensile strength of the welded joint on average by about 1.8 times — from 175 to 315 MPa.

Thus, the LHT of the welded joint allows a significant improvement of its quality.

Conclusions

1. Mechanical tensile tests of welded joints showed that fracture of the specimens occurs on the base material. This indicates a high quality of welding.

2. Comparative analysis of the level of strength of welded joints with the results of microhardness measurements, as well as with the results of fractographic examinations showed that fracture of the specimens occurred in the zone of reduction of mechanical properties.

3. With the use of LHT of welded joints during cooling from the temperature of 1000 °C, a phase transformation occurs, during which an additional β_0 (B2) phase appears in the structure, which is located along the colony boundaries and facilitates an increase in the ductility of the material.

4. The use of LHT increases the level of strength of the welded joint by approximately 1.8 times.

1. Appel, F., Paul, J.D.H., Oering, M. (2011) Gamma titanium aluminide alloys. Sci. and Technol., WILEY-VCH, Weinheim.
2. Kuchuk-Yatsenko, S.I., Zyakhor, I.V., Chernobaj, S.V. et al. (2015) Structure of γ-TiAl joints in resistance butt welding with application of interlayers. *The Paton Welding J.*, **9**, 5–12.
3. Patterson, R.A. (1990) Titanium aluminide: Electron beam weldability. *Welding J.*, **1**, 39–44.
4. Pflumma, R., Donchev, A., Mayer, S. et al. (2014) High-temperature oxidation behavior of multi-phase Mo-containing γ-TiAl-based alloys. *Intermetallics*, **53**, 45–55.
5. Kulikovsky, R.A., Pakholka, S.N., Pavlenko, D.V. (2015) Prospects of industrial application of titanium aluminide in aircraft engine construction. Stroitelstvo, Materialovedenie, Mashinostroenie. *Starodubov Lectures*, **80**, 369–372 [in Russian].
6. Xu, Q, Chaturvedi, MC, Richards, NL. (1999) The role of phase transformation in electron-beam welding of TiAl-based alloys. *Metallurg. and Mater. Transact., A*, **30A**, 1717–1726.
7. Liu, J., Dahmen, M., Ventzke, V. et al. (2013)The effect of heat treatment on crack control and grain refinement in laser beam welded beta-solidifying TiAl-based alloy. *Intermetallics*, **40**, 65–70.
8. Zamkov, V.N., Sabokar, I.K., Vrzhizhevsky, E.L. et al. (2005) Electron beam welding of γ-titanium aluminide. In: *Proc. of Int. Conf. on Ti-2005 in CIS*. Kiev, Naukova Dumka, 157–164.
9. Chen, G.Q., Zhang, B.G., Liu, W., Feng, J.C. (2011) Crack formation and control upon the electron beam welding of TiAl-based alloys. *Intermetallics*, **19**, 1857–1863.
10. Lobanov, L.M., Asnis, E.A., Piskun, N.V. et al. (2019) Investigation of stress-strain state of welded joints of the system TiAl intermetallics. *The Paton Welding J.*, **11**, 8–11.
11. Velikoivanenko, E.A., Milenin, A.S., Rozynka, G.F. et al. (2019) Prediction of cold cracking susceptibility of welded joints of γ-titanium aluminide based alloy in electron beam welding. *Tekhnologicheskie Sistemy*, **3**, 59–66.
12. Pukhalskaya, G.V., Markov, I.B. (2016) Determination of mechanical properties in different zones of welded joints of titanium alloy VT3-1. *Vestnik Dvigatelestroeniya*, **1**, 89–91 [in Russian].
13. Medvedev, A.Yu., Pavlini, S.P. (2012) Tensile tests of welded joints of titanium alloys performed by linear friction welding. *Vestnik UGATY*, 16(**7**), 52, 68–71 [in Russian].
14. Nochovnaya, N.A., Panin, P.V. (2014) Analysis of residual macrostresses in welded joints of titanium alloys of different classes. *Trudy VIAM*, **5**, 2 [in Russian].

Received 29.07.2020

https://doi.org/10.37434/tpwj2020.09.05

RESIDUAL STRESSES IN THIN-SHEET GALVANIZED STEEL JOINTS AFTER ARC WELDING AND PLASMA BRAZING

S.V. Maksymova[1], **I.V. Zvolinskyy**[1], **V.V. Yurkiv**[1], **S.M. Minakov**[2] and **V.V. Lysak**[2]
[1]E.O. Paton Electric Welding Institute of the NAS of Ukraine
11 Kazymyr Malevych Str., 03150, Kyiv, Ukraine. E-mail: office@paton.kiev.ua
[2]National Technical University of Ukraine «Igor Sikorsky Kyiv Polytechnic Institute»
37 Peremohy Prosp., 03056, Kyiv, Ukraine

In the manufacture of thin-walled structures by welding, residual stresses appear in them, which negatively affect the geometric parameters and quality of the obtained products. The paper presents the results of evaluation of residual stresses on simulators-samples made of galvanized steel 08ps (semi-killed) after MAG welding, plasma brazing using constant and modulated current. Reduction of residual stresses and avoidance of brazing filler metal spattering are promoted by reduction of heat input, when making permanent joints. One of the ways contributing to it is application of plasma brazing, which provides the ability setting the current, independently of filler material feed rate. Determination of the magnitude of residual stresses in the joints was performed by magnetoelastic method. It is shown that in plasma brazing with constant current the dimensions of the plastic strain zone are much smaller than in MAG welding, which is associated with a decrease in the amount of thermal energy applied to the metal. Plasma brazing with constant current allows lowering residual stresses from 149, which is obtained in welding to 119 MPa. Further reduction of residual stresses (up to 85 MPa) during plasma brazing of joints of galvanized steel 08ps is possible due to the use of modulated current. 18 Ref., 6 Figures.

Keywords: MAG welding, plasma brazing, modulated current, residual stresses, shrinkage force, plastic deformation, elastic deformation, heat input, galvanized steel, magnetoelastic method

In fabrication of thin-walled structures, for instance, car bodies, with application of welding, residual stresses arise in them, which have a negative effect on the geometric parameters and quality of the manufactured products. Residual stresses always develop, their magnitude in the weld area reaching values, equal to the yield limit. Violation of the geometric parameters leads to distortion of the shape of individual parts and requires application of labour-consuming operations of fitting-up in the connection points. Moreover, distortion of the shape of structure elements may lead to inadmissible violations in operation and can cause overstress in individual intersections of structural elements. Therefore, when designing such structures, it is necessary to take measures to prevent formation or reduction of the magnitude of residual stresses that can be achieved by the appropriate welding method or by application of alternative joining methods [1–3].

Effective methods of lowering the negative impact of residual welding stresses and strains in permanent joints is heat removal with application of heat-concentrated pastes; and reduction of heat input into the structure being welded. Used for this purpose are highly-dissipating heat sources (electron beam, plasma, pulsed-arc), as well as modes of welding with a low heat input and high speed of heat source movement (bare electrode over a layer of flux, etc.). By energy density the plasma heat source is in an intermediate position between the electric arc and beam (electron beam and laser) heat sources. It allows achieving a higher density of the heat flow in the treated product, compared to arc sources, despite being inferior to the beam sources by energy concentration, but it is much less expensive and more accessible by its engineering implementation [4, 5].

Galvanized steel is widely used in manufacture of car bodies. In a number of cases producing permanent joints from this material runs into considerable difficulties. Zinc starts melting at the temperature of 419.58 °C, and at 907 °C it evaporates. In MAG welding, when the temperature of base material edges exceeds that of zinc boiling, zinc coating burns from both sides. In order to ensure the corrosion resistance, the destroyed zinc layer has to be restored, that leads to additional expenses. Zinc penetration into the weld pool liquid metal leads to formation of porosity, cracks, spatter, incomplete penetration and unstable arcing (Figure 1) [6–8].

S.V. Maksymova — https://orsid.org/0000-0003-0158-5760, I.V. Zvolinskyy — https://orsid.org/0000-0003-1442-7980,
V.V. Yurkiv — https://orsid.org/0000-0001-8440-0391, V.V. Yurkiv — https://orsid.org/0000-0001-8607-4120,
V.V. Lysak — https://orsid/org/0000-0002-6565-2793

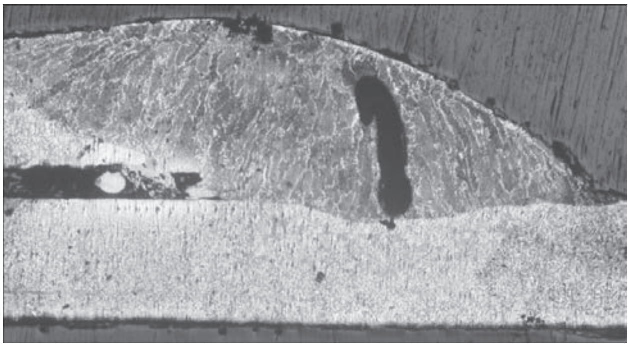

Figure 1. Macrostructure of overlap joint of galvanized steel produced by MAG welding

Plasma brazing is a promising method of joining galvanized steel. An advantage of plasma brazing is the ability to set the current, irrespective of the filler material feed rate, that allows reducing residual stresses by lowering the current and producing sound joints with preservation of zinc coating integrity. Different methods are used to determine the residual stresses [5, 9].

The objective of the work is determination of the magnitude of residual stresses which appear in permanent joints of galvanized steel 08ps in MAG welding, plasma brazing by constant and modulated current and their dependence on the heat input.

Input energy q_p is an important factor that affects the residual stresses and allows for the heat impact per a unit of length [10]. Input energy is the ratio of arc power q to welding or brazing speed:

$$q_{\mathrm{p}} = \frac{q}{V} = \frac{IU_{\mathrm{a}}\eta_{\mathrm{e}}}{V}, \qquad (1)$$

where q is the arc power, J/s; V is the brazing and welding speed, cm/s; I is the brazing and welding current, A; U_a is the arc voltage, V; η_e is the effective arc efficiency.

It was determined empirically that in MAG welding of galvanized steel the input energy is equal to 380 J/cm. Application of plasma brazing by constant direct current allowed reducing the heat input to 324 J/cm. Further lowering of the heat input to 273 J/cm is achieved due to application of plasma brazing by modulated current.

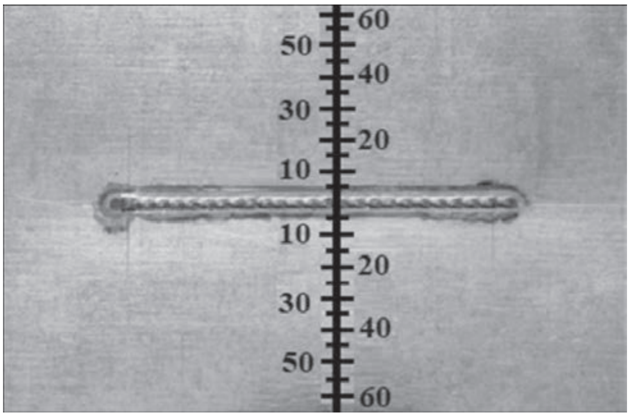

Figure 2. Sample from galvanized steel with brazed seam

Measurement of residual stresses was conducted by magnetoelastic method using MESTR-411 instrument on witness samples of 300×200×0.7 mm size.

Instrument graduation was performed at uniaxial tension. A flat sample made from galvanized steel 08ps was used for instrument graduation. Sample dimensions were equal to 500×50×0.7 mm. Rolling direction was along the longer side. The sample was fastened in the clamps of tensile-testing machine R-10. An electromagnetic transducer oriented along the direction of applied loading, was placed on the sample. The sample was loaded up to appearance of stresses on the level of 80 % of the yield limit, as further loading of the sample can cause plastic strains in it. Acting stresses were determined as the ratio of loading force to the sample cross-sectional area. During loading, instrument readings were recorded at each increase of stresses by 0.1 of the yield limit.

Graduation results were used to determine graduation coefficient T as the average stress increment per a unit of instrument readings by the following relationship

$$T = \frac{1}{N}\sum_{i=1}^{N}\frac{\Delta\sigma_i}{\Delta A_i}, \qquad (2)$$

where ΔA_i is the increment of instrument readings, corresponding to increase of stresses readings $\Delta\sigma_i$, N is the number of measurements at loading.

When any physical methods of measurement of mechanical stresses are used, obtained results are affected by deformation of metal grains in the direction of plate rolling, i.e. by the texture. In order to move away from the effect of the texture, it is necessary to determine the initial readings of the instrument for this type of structures from the given steel grade.

At determination of the initial readings of the instrument, the electromagnetic transducer was installed on the surface of galvanized steel plates, and it was oriented along the rolling direction. Rotating the transducer around its longitudinal axis clockwise and counterclockwise in a sector of approximately 30°, the largest reading of the instrument, A_0, was determined. Measurements were repeated in 10–15 points and the average value was determined. This value is the initial reading of the instrument for this type of structures from this steel grade [11, 12].

In order to measure residual stresses on welded and brazed samples, the electromagnetic transducer was installed on the sample surface along the weld and brazed seam. Measurements were conducted in the mid-section of the weld and brazed seam with 5 mm step on both sides from the weld on witness-samples of 300×200×0.7 mm size in the cross-section on the face and reverse sides with further averaging of the obtained values (Figure 2).

Acting mechanical stresses were determined by the following relationship

$$\sigma = T(A - A_0), \quad (3)$$

where T is the graduation coefficient; A_0 is the initial reading of the instrument.

Results of measurement of the residual stresses on samples produced by consumable electrode welding (MAG welding) and plasma brazing, are shown in Figure 3.

As one can see from the Figure, the nature of residual stress distribution in the welded and brazed samples is identical and corresponds to the classical one [13, 14]. So, in the welded sample tensile stresses occur in the weld zone, their maximum value reaching 149 MPa on the weld axis (Figure 3).

Magnitude of residual stresses on the weld axis is a little smaller than the base metal yield limit (175 MPa). The residual stress magnitude decreases smoothly with greater distance from the weld axis. At the distance of 10–12 mm from the joint axis tensile stresses become equal to zero, then they change their sign and transform into compressive stresses. Compressive stresses first increase, then decrease and are equalized.

Residual stresses in brazed samples are distributed similarly (Figure 3). In this case, the magnitude of maximum tensile stresses on the joint axis decreases to 119 MPa.

Presence of residual stresses in the joints can be regarded as the action of the shrinkage force [13, 15, 16] that causes distortion of the shape (deformation) of the welded and brazed samples.

Magnitude of such a shrinkage force is defined by expression (4) [13, 15]

$$P_{sh} = (|\sigma_t| + |\sigma_{com}|)b_{pl}\delta, \quad (4)$$

where σ_t is the magnitude of active residual tensile stresses, MPa; σ_{com} is the magnitude of reactive residual compressive stresses, MPa; b_{pl} is the width of plastic deformation zone, mm; δ is the thickness of welded and brazed samples, mm.

Indeed, for sheet structures with low rigidity, presence of such a shrinkage force, and, hence, of residual stresses, is an important factor, both from the viewpoint of structure performance, and from the viewpoint of its appearance.

In view of the above-said, let us analyze the quantitative characteristics of residual stresses in welded and brazed samples.

As one can see from the experimental results, maximum value of residual active tensile stresses of welded and brazed samples is on the level of 149 and 119 MPa, respectively. Such an experimental result can be explained in terms of the mechanism of residual stress formation at nonuniform heating of the middle band of the model of welded and brazed samples — a plate with slots for the general case, when the dimensions of the heated zone are smaller than those of the plate proper, i.e. $F_{mid} < F_{edge}$ (Figure 4) [15].

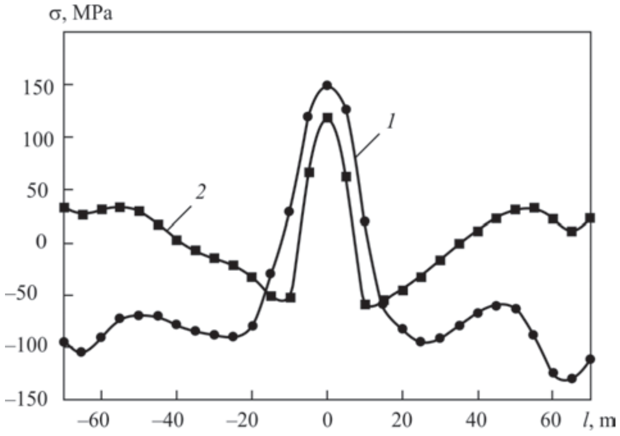

Figure 3. Distribution of residual longitudinal stresses in mid-section of brazed sample, compared to welded sample: *1* — MAG welding; *2* — plasma brazing by constant current

At heating of the middle band it develops temperature deformations $e_t = \alpha T$.

Impossibility of realization of the arising temperature deformations by the middle band, because of the bonds between the middle band and the unheated

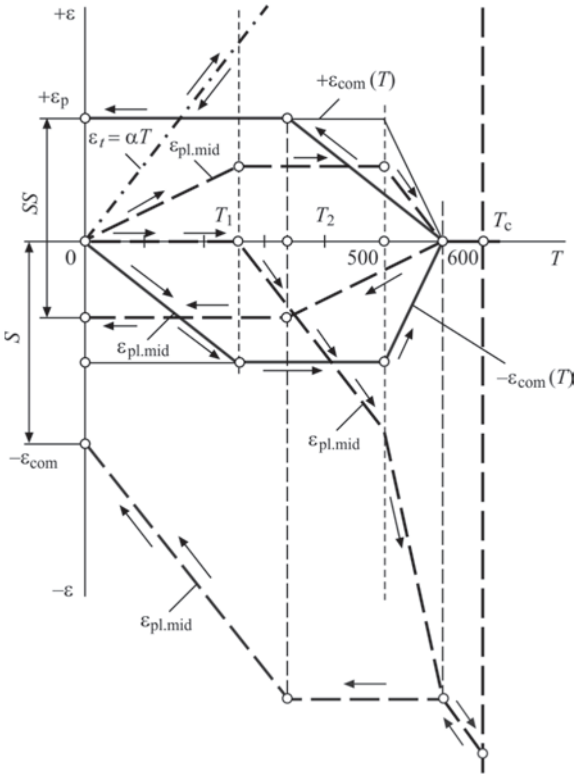

Figure 4. Scheme of strain development in a slotted steel plate at $F_{mid} > F_{cr}$ [15]

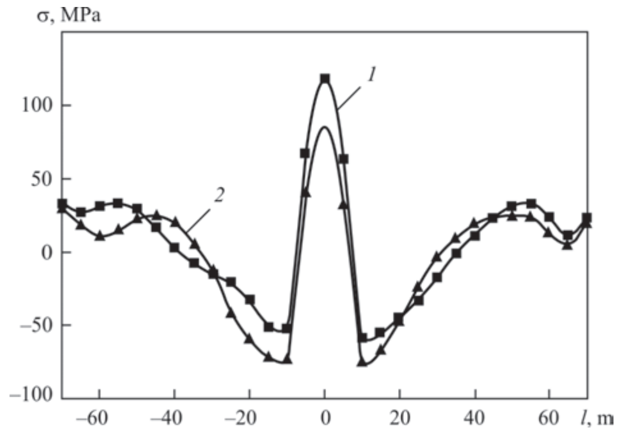

Figure 5. Distribution of longitudinal stresses in brazed samples produced using plasma heating with application of direct constant and modulated current: *1* — plasma brazing by constant current; *2* — plasma brazing by modulated current

edge zones, causes elastic shrinkage strains (compressive stresses) in the middle zone.

By the condition of equilibrium, tensile elastic strains (stresses) develop in the extreme bands. At T_1 temperature elastic shrinkage strains of the middle band reach its maximum value, which is followed by development of plastic shrinkage strains $-\varepsilon_{\text{pl. mid}}$ in the middle band (Figure 4).

At further heating, elastic strains of the middle band remain on the level of $-\varepsilon_{\text{pl. mid}}$, and starting from temperature T_1 plastic shrinkage strains develop in the middle band.

In the temperature range from 500 to 600 °C, elastic strains of the middle zone decrease to zero. At the same time, plastic strains of the middle band dramatically increase their growth rate.

At the cooling stage, thermal deformation processes proceed with opposite signs. At the same time, as follows from Figure 4, complete compensation of plastic strains accumulated at heating does not take place. As a result, a nonuniform distribution of residual plastic strains in the plate cross-section is found in the slotted plate (they are present in the middle band, but absent in the extreme ones) that is exactly what causes development of residual stresses in the welded and brazed joints.

In this case, if the metal was heated to temperature above 600 °C, the magnitude of residual tensile stresses forms on the level of the yield limit. Depending on the ratio of areas, where residual active tensile stresses and reactive compressive stresses arise, residual compressive stresses $-\sigma_{\text{com}} = \varepsilon_{\text{el}}E$ form in the reactive zone, according to the equilibrium condition. Considering that the technology of making the brazed joints envisages compulsory melting of the filler metal, i.e. heating above 600 °C, the magnitude of maximum tensile stresses on the weld axis for the welded and brazed joints should be close that is confirmed by experimental results (Figure 3). In the zone of reactive compressive stresses, depending on their formation mechanism, reactive compressive stresses form (in the extreme zone of the plate). Their magnitude is determined by the condition of equilibrium of forces in the zones of residual active tensile stresses and reactive compressive stresses of the welded and brazed joints [14]:

$$\sigma_{\text{t}} b_n \delta = -\sigma_{\text{com}}(h - \delta_n)\,\delta, \tag{5}$$

$$\sigma_{\text{com}} = -\frac{\sigma_{\text{t}} b_n \delta}{(h - b_n)\delta}, \tag{6}$$

where *h* is the considered joint width.

As one can see from Figure 3, the magnitude of residual compressive stresses is smaller in brazed joints than in welded joints. Reduction of the value of residual reactive compressive stresses, in keeping with expression (6), is attributable to reduction of the width of plastic strain zone.

It is obvious that such a reduction of the magnitude of reactive and active stresses will lead to a considerable reduction of shrinkage force, and, therefore, also to reduction of residual strains of the structure.

Studying the precise dimensions of the width of plastic strain zone requires performance of special studies with involvement of specific investigation procedures. Therefore, in this work we limited ourselves to qualitative assessment of comparison of the values of the width of plastic strain zone in welded and brazed samples. Various approaches to determination of the width of plastic strain zone are described in publications [13, 17].

Analyzing the dimensions of plastic strain zone (Figure 3) with application of the procedure of [17], we can see that this zone does not exceed 30–35 mm in brazed joints, while the width of plastic strain zone in welded joints reaches 50–60 mm. Such a considerable reduction of plastic strain zone in brazed joints is explained by, firstly, a smaller amount of thermal energy introduced into the metal. Moreover, at plasma brazing the heat is introduced into the metal by a highly concentrated source that also promotes a reduction of the width of the heated zones and leads to narrowing of plastic strain zone.

An essential factor of reducing the heat input into the joint in plasma brazing also is heat introduction using modulated current [18]. This can be confirmed by the results of measurement of residual stresses in brazed samples that were made with application of constant and modulated current (Figure 5).

As one can see from Figure 5, the magnitude of maximum tensile stresses on the weld axis at modulated current application, decreases to 85 MPa, compared to the seam brazed at direct constant current. Such a reduction of tensile stresses in the sample is explained by that the sample was brazed in the mode with modulated current at maximum value of the process duty cycle, i.e. minimum value of pulse time ($\tau_i = 0.05$ s), which causes a significant reduction of the heat input into the base metal. This provides confirmation of the statement that heat introduction into the product using modulated current ensures lowering of residual stresses.

Conclusions

1. Studies performed by magnetoelastic method revealed that residual stresses arise in MAG welding of galvanized steel, the magnitude of which is equal to 149 MPa at the heat input of 380 J/cm.

Application of plasma brazing by constant current allows reducing the heat input to 324 J/cm and residual stresses to 119 MPa.

Further reduction of the heat input to 273 J/cm, and, the resulting reduction of residual stresses to 85 MPa, is ensured by application of modulated current in plasma brazing of galvanized steel 08ps.

1. Kozlov, S.V., Kirillov, Yu.V. (2009) Application of plasma welding as the method for lowering of residual strains and stresses in steel welded structures. In: *Collect. of V.M. Shimanovsky Ukrniiproektstalkonstruktsiya*, **3**, 102–107 [in Russian].
2. Monfared, A.Kh., Panteleenko, A.F. (2011) Mathematical modeling of welding deformations in thin plates. *Vestnik BNTU*, **5**, 19–25 [in Russian].
3. William, N. (2008) *Sringer handbook of experimental solid mechanics*: Refer. Book. Springer US. https://doi.org/10.1007/978-0-387-30877-7
4. Paton, B.E. (2000) Plasma technology at the turn of the century. *The Paton Welding J.*, **12**, 3–5.
5. Sitnikov, B.V. (2012) Influence of pulsed-arc welding parameters on distribution of residual stresses in AMg6 joints. *Energosberezhenie, Energetika, Energoaudit*, 102(**8**), 69–74 [in Russian].
6. Robert, K. (2005) Plasma brazing — Advantages and disadvantages compared with MIG brazing. *Welding and Cutting*, 4(**3**), 147–149.
7. *Pavol Sejc* (2010) MAG zvaranie pozinkovanych plechov v ochrannom plyne CO_2 a Ar + 18 % CO_2. *Zvarac*, VII, **3**, 8–13.
8. *Pavol Sejc* (2002) Oblukove zvaranie MAG ocelovych plechov pokrytych protikoroznym naterrom na baze zinku. *Zvaranie-Svarovani*, 3(**4**), 71–73.
9. Shonin, V.A., Mashin, V.S., Khaskin, V.Yu., Nedej, T.N. (2006) Residual stresses in butt joints of thin sheets from alloy AMg6 after arc and laser-arc welding. *The Paton Welding J.*, **9**, 20–24.
10. Makhnenko, O.V, Muzhichenko, A.F., Prudky, I.I. (2013) Mathematical modelling of stress-strain state of welded panels from titanium alloy VT20. *Ibid.*, **2**, 13–19.
11. Mekhontsev, Yu.Ya. (1986) *Sensor of magnetic anisotropy*. USSR author's cert. Int. Cl. 2 G01N27/86 [in Russian].
12. Minakov, S.M. (2012) *Determination of state of main pipelines by magnetoanisotropic method*: Syn. of Thesis for Cand. of Techn. Sci. Degree. Kyiv [in Russian].
13. Trochun, I.P. (1964) *Internal forces and deformations in welding*. Moscow, Mashgiz [in Russian].
14. Vinokurov, V.A. (1968) *Welding strains and stresses*. Moscow, Mashinostroenie [in Russian].
15. Kasatkin, B.S., Prokhorenko, O.V., Chertov, I.M. (1987) *Strains and stresses in welding*. Kiev, Vyshcha Shkola [in Russian].
16. Prokhorenko, V.M., Prokhorenko, O.M. (2009) *Stresses and strains in welded joints and structures: Manual*. Kyiv, NTU [in Ukrainian].
17. Nikolaev, G.A., Kurkin, S.A., Vinokurov, V.A. (1982) *Welded structures. Strength of welded joints and deformations of structures: Manual*. Book 1. Moscow, Vysshaya Shkola [in Russian].
18. Nurguzhin, M., Danenova, G., Akhmetzhanov, T. (2019) Computer modeling of residual stresses and strains at arc welding by modulated current. In: *Proc. of 4th Inter. Conf. on Industrial Engineering*. ICIE 2018. Lecture Notes in Mechanical Engineering. Springer, https://doi.org/10.1007/978-3-319-95630-5_265

Received 07.08.2020

https://doi.org/10.37434/tpwj2020.09.06

DOUBLE HEAT TREATMENT OF WELDED BUTT JOINTS OF RAILWAY RAILS

Ye.O. Panteleimonov
E.O. Paton Electric Welding Institute of the NAS of Ukraine
11 Kazymyr Malevych Str., 03150, Kyiv, Ukraine. E-mail: office@paton.kiev.ua

The paper presents the results of heat treatment of butt welded joints of R65 rails from K76F steel, produced by flash-butt welding. It is shown that after pre-annealing of butt welded joints with further accelerated heating up to the temperature of heat treatment and quenching of the rail rolling surface by compressed air, the microstructure of butt welded joint metal changes, grain size is considerably refined, hardness along the HAZ width is increased, and deviation of metal hardness along the joint line from base metal level becomes smaller. 12 Ref., 1 Table, 5 Figures.

Keywords: rails, welded butt joints, heat treatment, microstructure, hardness

Butt welded joints of railway rails should have a high complex of mechanical properties that is due to significant axial loads and freight train speeds. This is related, mainly, to high strength of the metal of butt welded joints which forms to a sufficient depth of the working part of the head, in combination with the high ductility and toughness of the web and foot metal. Welded joints of the rails made by flash-butt welding are subjected to heat treatment (HT). HT impact is aimed at achievement of structural zonal homogeneity in the HAZ and elimination of unfavourable diagram of the internal residual stresses [1, 2]. Modern technology and equipment for HT performance include heating of the butt joints to the temperature of 850–950 °C by high-frequency currents and surface quenching of the head by compressed air [3, 4]. However, the technology of such single HT of butt joints of rails from low-alloyed steel does not allow fully obtaining the complex of high mechanical properties. In this connection, it is necessary to search for new components of HT technology.

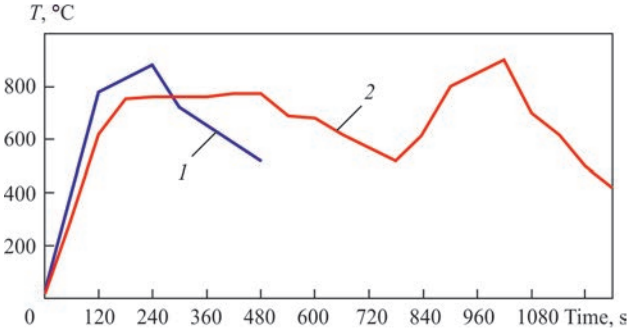

Figure 1. Time dependencies of the head heating temperature at the depth of 25 mm from the rolling surface at single (*1*) and double (*2*) HT

It is known that after quenching of steel with the initial fine-grained structure, it has higher wear resistance and contact-fatigue strength [5–7]. Annealing belongs to widely accepted technological operations, applied to form a fine-grained structure of a lower hardness, high ductility and toughness. It is rational to use the properties of pre-annealing as a component of the technology of HT of rail butt welded joints. In this case, the technology of such double HT will include pre-annealing, further accelerated heating up to HT temperature and surface hardening of the rail head in the butt joint.

This work gives the results of studying the impact of double HT on the properties of welded butt joints of R65 rails from K76F steel. Microstructure and hardness of butt joint metal along the HAZ width in the rail head, web and foot was analyzed. Properties of butt joints after welding, after single and double HT were compared. The model of PWI portable module was used to perform HT of welded butt joints [8, 9]. The butt joints were heated by inductors with magnet cores [10–12]. Current frequency was 2.4 Hz. HAZ width in the butt joints after single and double HT was greater than in the butt joints after welding. This is due to the features of the portable module structure.

Comparisons of heating modes and properties of butt welded joints given in the work predominantly concern the rail head at 25 mm depth from the rolling surface. This allowed ignoring the impact of quench cooling. At single HT of butt welded joints the rate of head heating at such a depth up to the temperature of magnetic transformation point was equal to 6.5 °C/s (Figure 1). The heating rate after the metal has lost its magnetic properties decreased to 1 °C/s. HT temperature at the end of heating reached 890–900 °C. Total heating time was 240 s. At the moment heating was stopped, the temperature gradient between the head

Metal grain size number along the joint line (JL) at 5–8 mm from the joint line (5–8 mm from JL) and in incomplete recrystallization zone (IRC)

Rail element	Grain size number after welding			Grain size number after single HT			Grain size number after double HT			Base metal
	JL	5–8 mm from JL	IRC zone	JL	5–8 mm from JL	IRC zone	JL	5–8 mm from JL	IRC zone	
Head (25 mm from the rolling surface)	2–3	4–5	6–7	7–9	8–9	9	10	9–10	8–9	5–8
Web (center)	3	5	7	7–9	7–8	9	9–10	8–9	9	7–8
Foot (10 mm from the base)	3	5	7	8–9	8	10	9–10	10	10	5–6

rolling surface and layer at the depth of 25 mm was not more than 50 °C. At double HT the butt welded joints were heated to the temperature of 750 °C at the rate of 5 °C/s. The temperature was maintained for 300 s and the butt joints were cooled to the temperature of 510 °C in calm air. Then the butt joints were heated up to the temperature of 890–900 °C. Reheating time was equal to 230–240 s. At the moment of heating interruption, the temperature gradient between the head rolling surface and layer at 25 mm depth was less than 40 °C. Quenching of the head rolling surface was performed by forced blowing by compressed air. Quenching time was 240 s, and pressure in air feeding system was 0.5 MPa.

Longitudinal samples were used to study the structure of metal of butt welded joints of rails. Sample surface coincided with the rail axis of symmetry, included the HAZ and adjacent regions of base metal. The size of metal grain was determined by GOST 5639–82. For instance, in the rail head at 25 mm depth from the rolling surface, in the butt joints after welding the grain size number in decarbonized metal band along the joint line was 2–3 (Table). Metal structure is sorbite with narrow ferrite fringes along the large grain boundaries (Figure 2, *a*). At 5–8 mm distance from the joint line, the structure consists of sorbite with grain size number of 4–5 (Figure 2, *b*). In incomplete recrystallization (IRC) zone, at 18 mm distance from the joint line, the structure consists of fine sorbite with grain size number of 6–7. The base metal had regions with grain size number from 5–6 to 7–8. After single HT of the butt joints, the metal microstructure is much finer. Along the joint line in the sorbite structure the grain size number increased from 2–3 to 7–9 (Figure 2, *c*). At 5–8 mm distance from the joint line, in the structure of sorbite with troostite regions the grain size number increased from 4–5 up to 8–9 (Figure 2, *d*). In IRC zone at 28 mm distance from the joint line, grain size number is 9. At the distance of 18–20 mm from the joint line, where IRC zone was located after welding, grain size number increased up to 7–9. After double HT of butt joints, the grain became even finer. Along the joint line the grain is fine and uniform with fragmented ferrite boundaries

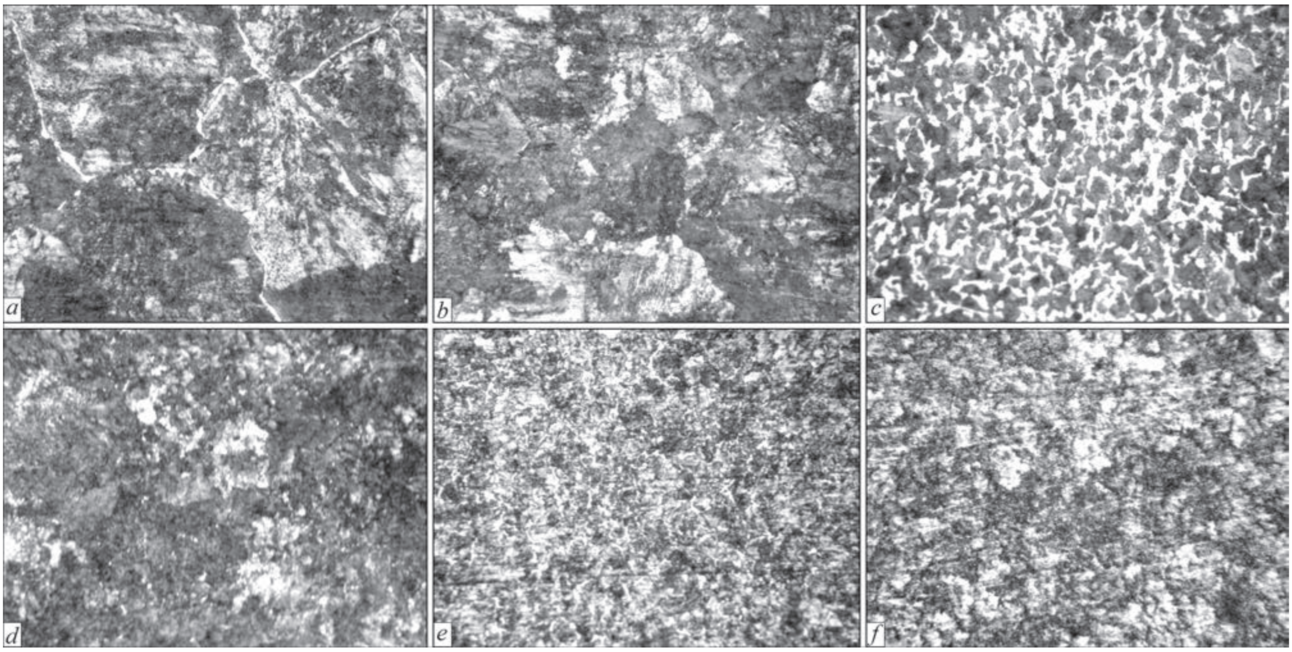

Figure 2. Microstructure (×500) of the metal of butt welded joints in the rail head at 25 mm depth from the rolling surface: joint line (*a*, *c*, *e*); 5–8 mm from the joint line (*b*, *d*, *f*), as-welded (*a*, *b*); after single HT (*c*, *d*); after double HT (*e*, *f*)

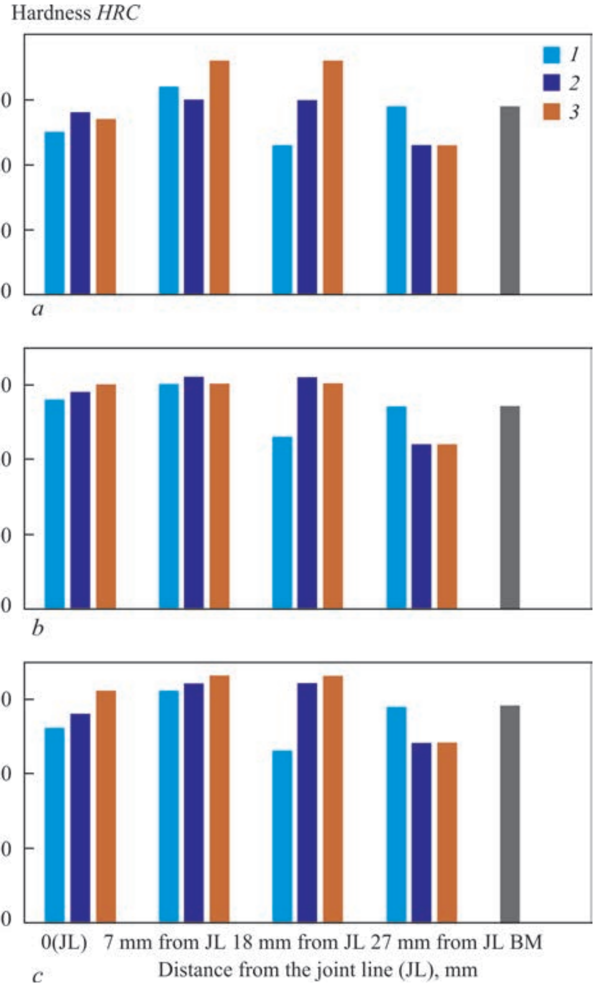

Figure 3. Distribution of *HRC* hardness along the HAZ width of butt welded joints of rails in the head at 25 mm depth from the rolling surface (*a*); in the web center (*b*) and in the foot at 10 mm distance from the base (*c*), after single HT (*2*) and after double HT (*3*)

(Figure 2, *e*), the grain size number increased to 10. At 5–8 mm distance from the joint line, the structure is fine uniform sorbite (Figure 2, *f*). Grain size is 9–10.

Integral hardness *HRC* of the metal of butt welded joints was measured in TK-2M hardness meter at 150 kg load. As shown in Figure 3, the hardness along the joint line (JL) in butt joints after welding was *HRC* 25 at 25 mm depth from the rolling surface, in the web center it was *HRC* 28, and at 10 mm distance from the foot base it was *HRC* 26. At 7 mm distance from the joint line (7 mm from JL) hardness in the head and foot was *HRC* 31–32, and in the web it was *HRC* 30. Metal in IRC zone at 18 mm distance from the joint line (18 mm from JL) had low hardness of *HRC* 22–23. After single HT, hardness along the joint line increased to *HRC* 28 in the head, in the web to *HRC* 29 and in the foot to *HRC* 28. After double HT, hardness along the joint line was equal to *HRC* 27, it increased to *HRC* 30 in the web, and to *HRC* 31 in the foot. From the joint line to IRC zone hardness in the head increased to *HRC* 36, and in the foot to *HRC* 33. In IRC zone at 27 mm distance from the joint line, hardness was *HRC* 22–24. Such a distribution of hardness by the HAZ width is also characteristic for regions of the head transition to the web, and of the web to the foot. Hardness distribution in the zone of quench cooling was somewhat different (Figure 4). After double HT, the hardness at 5 mm depth from the head rolling surface and 7 mm distance from the joint line increased to *HRC* 40. This is more than in the initial rails, where hardness is *HRC* 37–38.

Histograms given in Figure 5 characterize the deviation of *HRC* hardness along the width of the HAZ of rail butt joints relative to the hardness of base metal of the respective rail elements. In the butt joints after welding the hardness in the head along the joint line (JL) is smaller than that of the base metal by 14 %, at the distance of 7 mm from the joint line it is higher by 10 %, and in IRC zone it is by 21% smaller. In the web center hardness along the joint line is higher by 3 %, in IRC zone it is lower by 15 %. Significant deviation of hardness is characteristic for the rail foot. Here, hardness lowering reached 10 % along the joint line and 18 % in IRC zone. After single HT, it can be noted that hardness along the joint line and at 7 mm distance from the joint line in the rail head and foot became close to that of the base metal. In particular, hardness deviation along the joint line is not more

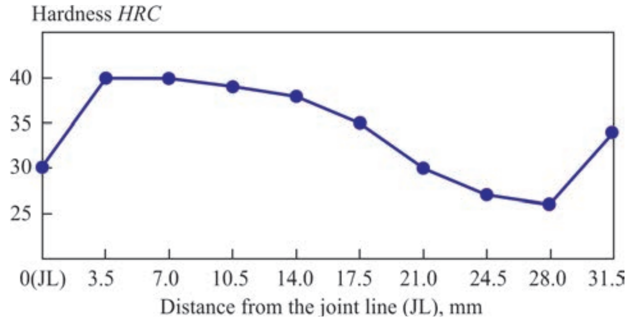

Figure 4. Distribution of *HRC* hardness along the HAZ width of rail butt welded joints in the zone of quench cooling at 5 mm depth from the head rolling surface after double HT

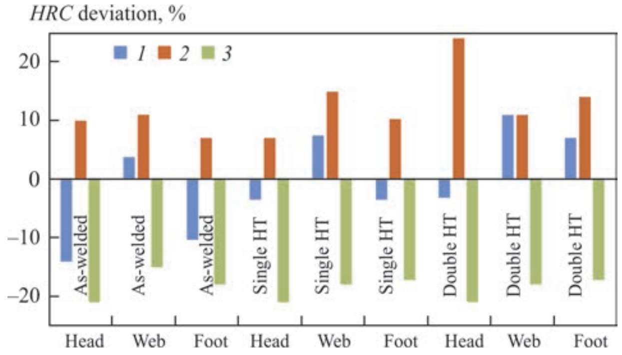

Figure 5. Deviation of *HRC* hardness of rail butt welded joints from base metal hardness along the joint line (JL) (*1*), at 7 mm distance from the joint line (7 mm from JL) (*2*) and in incomplete recrystallization zone (IRC) (*3*) after welding, after single HT and after double HT

than 3 %. It is indicative of the mechanical properties of butt welded joints becoming closer to base metal level. In the butt joints after double HT the hardness in the head along the joint line also decreased by 3 % from the base metal level, and in the web and foot it increased by 11 and 7 % respectively. At 7 mm distance from the joint line, the hardness increased considerably, by 24 % in the head and by 14 % in the foot.

Conclusions

1. Single HT of welded butt joints of R65 rails from K76F steel, after accelerated heating to the temperature of 890–900 °C, and quenching of the rolling surface in the butt joint zone, results in the mechanical properties of the welded butt joints becoming close to the level of the rail base metal.

2. Double HT of butt welded joints of rails which includes pre-annealing at the temperature of 750 °C, its further accelerated heating up to the temperature of 890–900 °C and quenching of the rail rolling surface in the butt joint zone, led to a change of the metal microstructure, grain refinement to size number 8–10 along the entire HAZ width. Hardness in the head along the joint line became close to base metal level and increased in the web and foot. Hardness along the HAZ width became much higher in the direction from the joint line to incomplete recrystallization zone.

3. Hardness in the zone of quench cooling of the head after double HT and quenching of the rolling surface was higher than the initial rail hardness.

4. Impact of single and double HT on the structure and hardness of butt welded joints of rails, made by flash-butt welding, allows recommending application of such technologies to increase the reliability of butt joints, particularly under hard operating conditions of the rail track.

1. Genkin, I.Z. (2003) Heat treatment of rail welded joints in induction units. *The Paton Welding J.*, **9**, 38–41.
2. Nesterov, D.K., Sapozhkov, B.E., Levchenko, N.F. et al. (1990) Heat treatment of rail steel using induction heating. *Metallovedenie i Termich. Obrab. Metallov*, **8**, 30–34 [in Russian].
3. Feshchukov, A.N. (2016) *Unit for heat treatment of rail welded joints in the field.* RF, Pat. 57752, Int. C. E01B31/18 [in Russian].
4. Rezanov, V.A., Fedin, V.M., Bashlykov, A.V. (2013) Differential quenching of rail welded joints. *Vestnik NII Zheleznodorozhnogo Transporta*, **2**, 28–33 [in Russian].
5. Skoblo, T.S., Sapozhkov, V.E., Aleksandrova, N.M., Sidashenko, A.I. (2014) *Quality of thermally-hardened rails and bases. Examinations. Theory. Equipment. Technology. Operation.* Ed. by T.S. Skoblo. Kharkov, LLC «Shchedra Sadyba Plus» [in Russian].
6. Stalinsky, D.V., Rudyuk A.S., Sapozhkov, V.E., Nesterov D.K. (2007) Spheroidizing of carbide phase in hypereutectoid steel and its influence on rail properties. *Metallurg. i Gornorud. Promyshlennost*, **2**, 48–54 [in Russian].
7. Ostrovsky, G.A., Sarrak, S.I., Shepelyakovsky K.Z. (1967) Influence of austenitic grain change on properties of carbon steels after low-temperature tempering. *Metallovedenie i Termich. Obrab. Metallov*, **6**, 56–62 [in Russian].
8. Panteleimonov, E.O. (2017) *Complex for heat treatment of rail welded joints in the field.* Ukraine, Pat. on utility model 114593, Int. Cl. E01B31/18 [in Ukrainian].
9. Pantelejmonov, E.O. (2020) *Module for heat treatment of rail welded joints*. Ukraine, Pat. on utility model 143908, Int. Cl. E01B 31/18 (2006.01), C21D 1/10 (2006.01) [in Ukrainian].
10. Pantelejmonov, E.O. (2016) *Induction device for rail welded joints*. Ukraine, Pat. on utility model 109123, Int. Cl. C21D 1/10 (2006.01) [in Ukrainian].
11. Pantelejmonov, E.A., Gubatyuk, R.S. (2016) Induction device for heat treatment of welded joints of railway rails. *The Paton Welding J.*, **10**, 41–43.
12. Panteleymonov, E.A. (2018) On the problem of heat treatment of welded joints of railway rails. *Ibid*., **3**, 36–39.

Received 26.05.2020

https://doi.org/10.37434/tpwj2020.09.07

WELDING OF POLYMER FILMS BY LOW POWER LASERS

M.G. Korab, M.V. Yurzhenko, A.V. Vashchuk and **M.G. Menzheres**
E.O. Paton Electric Welding Institute of the NAS of Ukraine
11 Kazymyr Malevych Str., 03150, Kyiv, Ukraine. E-mail: korab_nikolay@ukr.net

The technology of laser welding by a transmission method allows welding overlapping polymeric films and sheets of various thickness. Welding of polyvinyl chloride films using a solid-state diode-pumped laser (DPSS) of 10 W power, which generates green radiation with wavelength of 532 nm, was performed in the developed experimental equipment. Application of this method made it possible to weld transparent multilayer medical films Wipak. Experiments have shown that with the help of such a laser it is possible to form a high-quality joint of Wipak medical film with paper. 9 Ref., 5 Figures.

Keywords: welded joints, polymer films, transmission laser welding, diode lasers

Versatility and adaptability to environmental conditions allows laser welding to be used even in the field conditions, where the question of welding fabrication productivity is the most relevant. More over, high intensity and monochromatic nature of the laser beam allow reaching high values of power and density of the energy flow that makes it fundamentally different from other heat sources in the welding technology. As laser radiation is an inertialess object, the time of the beam switching on and off, the change of its energy properties, as well as the direction of its movement relative to the treated part, are determined exclusively by the speed of laser radiation source, and the system of radiation transport and radiation control devices. The thermal cycle is determined by the accepted welding mode, which depends on radiation power, welding speed, conditions of beam position relative to the part being welded, cooling conditions, as well as thermophysical properties of the material. Thus, application of laser radiation and high productivity of laser welding at correct weld formation enable reaching a high level of welding process automation.

Laser welding is a radiation welding process with heating of the surfaces that are joined due to conversion of electromagnetic radiation energy into heat [1]. Laser designs can be divided into four main types (Figure 1), differing by radiation wave length and other parameters, and they can be used for welding of plastics [2, 3].

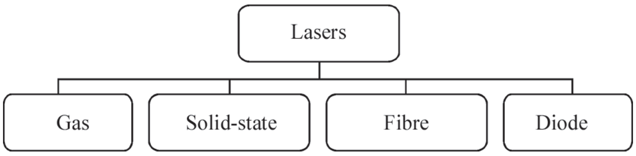

Figure 1. Laser types

Carbon dioxide (CO_2) gas laser generates continuous radiation with wave length of 10.6 μm. As such an IR radiation is readily absorbed by practically all kinds of plastics, powerful CO_2 lasers are applied for cutting and welding of polymer materials [4].

An active medium of solid-state lasers are dielectric crystals, activated by ions of rare-earth elements [5]. The most powerful of the solid-state devices is yttrium-aluminium neodymium laser (Nd:YAG), which generates radiation with 1.064 μm wavelength in the pulsed mode with the periodicity of less than a nanosecond. Such lasers are widely used in medicine and for treatment of engineering materials, in particular welding of plastics.

Fibre lasers use optical wave guide with fibres, alloyed by rare-earth elements, as active media. They form a sharply directed beam, which can be easily focused into a spot of very small dimensions. This laser type is convenient by that it can be readily combined with fibre optic lines for radiation transmission [6].

Diode (semiconductor) lasers are also solid-state ones, but unlike the above-mentioned lasers they have a different operation principle. An active medium in such lasers are semi-conductors, based on gallium and indium. Power of semiconductor lasers is smaller, but they are simple and compact, and can generate radiation in the optical, near and middle IR range. Therefore, semiconductor lasers are extensively used for treatment and welding of polymer materials [7, 8].

Development and mass industrial production of solid-state lasers greatly expanded the technological capabilities of laser welding of plastics. The most ex-

M.G. Korab — https://orcid.org/0000-0001-8030-1468, M.V. Yurzhenko — http://orcid.org/0000-0002-5535-731X,
A.V. Vashchuk — http://orcid.org/0000-0002-4524-4311

tensively used now is overlap laser welding of sheet polymer materials by the transmission method. In this case, laser radiation of optical and near IR range passes through the transparent upper part of the welded joints, and is absorbed with heat evolution on the contact surface of parts. Such a method is often used to weld polymer films or sheet billets, which are semitransparent for laser radiation. Therefore, a possible variant is when the radiation is partially absorbed by both the billets, heating the welding zone [9].

Laser welding is believed to be costly from the view point of capital costs. At application of low power inexpensive lasers, however, this welding method can be more convenient, compared to other methods in manufacture of products from polymers films. It is believed that practically all the thermoplastics, such as polyethylene, polyvinylchloride, polypropylene, polystyrene, polycarbonate, ABS, polyamides, polymethyl methacrylate, as well as thermoplastic elastomers, are suitable for laser welding.

In our previous works we showed that 1 W laser is enough for film welding in the thickness range of 0.015–0.1 mm. A more powerful energy source is required for welding thicker material. Moreover, application of slides often does not allow accurately guiding the laser beam to the joint line, and following the progress of welding. Therefore, in this work a series of technology studies was conducted, using a more powerful long-focus source.

In this work, a 10 W diode-pumped solid-state laser was mounted on a carriage with regulated electromechanical drive (Figure 2). This laser uses a powerful diode with radiation wavelength of 808 nm, which is subjected to a series of transformations and eventually a green-coloured laser beam with 532 nm wavelength forms at the output. This radiation passes readily through transparent polymer materials, is less reflected from their surface and is readily absorbed by darkened materials. The laser is fitted with a system of lenses to form the beam, which allows focusing the radiation at 120 mm distance from the front edge of the case, or defocusing it to reduce energy concentration in the heated spot. Minimum diameter of laser radiation spot was 1.1 mm.

Laser case was fastened in a metal cylinder, which was able to move along a vertical guide with fixing at different distances from the plane of the parts being welded. During experiments, laser power remained unchanged, specific radiation energy was varied by adjustment of welding speed and distance from the laser to the part. Increase of laser power enabled welding thicker films from PVC. In welding the film was fixed by glass plates to ensure the required pressure and prevent joint deformation.

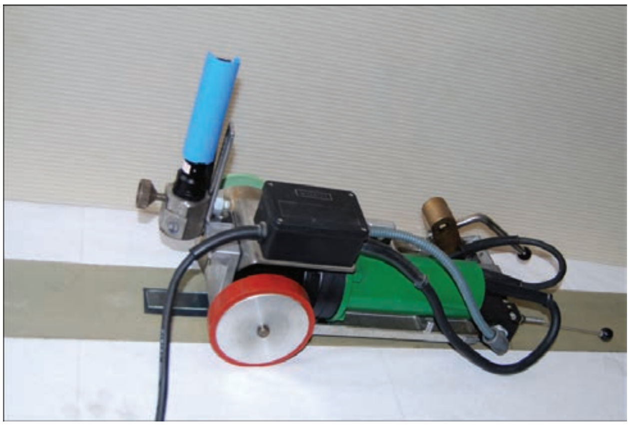

Figure 2. Experimental equipment for transmission laser welding of polymer film by a long-focus laser

Figure 3 shows the transverse section of an overlap weld of two PVC films 0.1 and 0.3 mm thick. At optimally selected welding mode, due to sufficient preheating of the lower film material, the upper film melts more than by half of its thickness that promotes formation of a sound welded joint.

Also studied was the weldability of special multilayer polymer film for medical packaging of Wipak Company. The widest application of this film is for manufacturing flat bags for medical instruments, where the film is bonded around the outer perimeter to a sheet of special paper by thermal welding. The film is completely transparent, so it poorly absorbs the laser radiation. Experiments showed that laser application enables forming a joint of the film with paper. For this purpose, it is necessary to apply additional pressure to the weld zone by special loading of the glass plate. In this case, adhesion of the film lower layers to the paper is achieved by heating the paper (Figure 4).

On the whole, for sufficient heating of the transparent polymer film, it is necessary to add to the weld zone dyes of black or dark colours, which promote active absorption of laser radiation and do not lower the mechanical characteristics of the joint material. Such dyes can be the traditional soot or graphite or fine polyethylene powder.

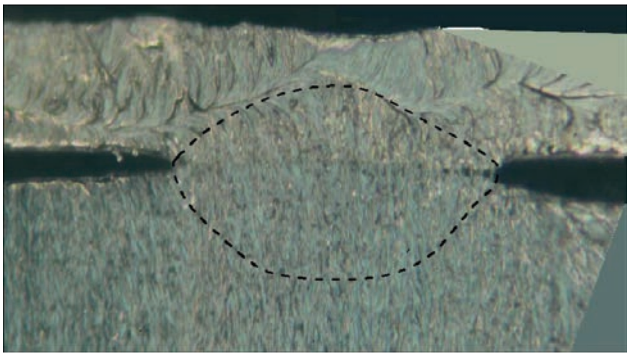

Figure 3. Transverse section of PVC film joint made by transmission laser welding. Dashed line marks the weld contours (×200)

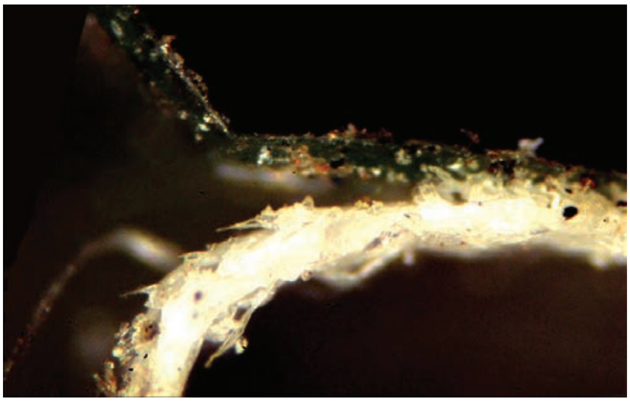

Figure 4. Joint of Wipak multilayer film to paper (×100)

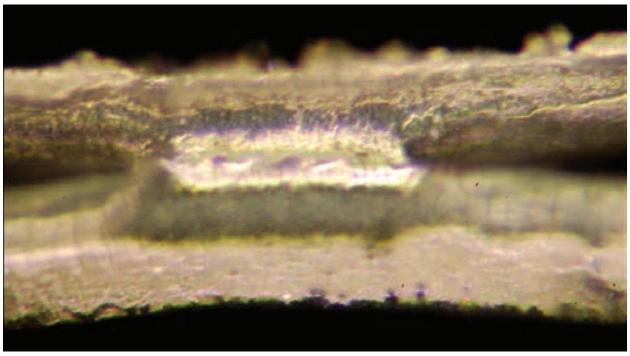

Figure 5. Optimum shape of the weld of polyethylene film 0.1 and 0.15 mm thick made by transmission laser welding (×200)

As a result of technological studies, the optimum parameters of transmission laser welding of polymer films were determined by the results of assessment of the weld appearance, studying their transverse sections under the microscope, as well as by the results of mechanical testing of film weld samples, in keeping with the requirements of the valid normative documents. At optimum parameters of the welding mode pores, blowholes, cracks or other defects are absent on the weld outer surface, on the weld transverse section uniform penetration is observed (Figure 5), which is somewhat increased for the lower film. Mechanical strength of such welds is on base material level. Investigation results were the base for development of recommendations on transmission laser welding of polymer films of different kinds, using low-power lasers of optical range.

Conclusions

Experimental studies of the impact of the main parameters of laser welding process on the morphology and service properties of the joints of polymer films and sheets were conducted. Rationality of application of low-power solid-state (diode) lasers of optical range was substantiated. Experimental equipment for laser transmission welding of polymer films was developed and manufactured. Technological recommendations were elaborated on laser welding of thin polymer materials that can be an alternative for joining polymer films by a heated tool.

1. Korab, G.N., Shestopal, A.N., Komarov, G.V. et al. (1988) *Dictionary and reference book on welding and gluing of plastics*. Ed. by B.E. Paton. Kiev, Naukova Dumka [in Russian].
2. Moskvitin, G.V., Polyakov, A.N., Birger, E.M. (2012) Laser welding of plastics (Review). *Svarochn. Proizvodstvo*, **9**, 21–33 [in Russian].
3. Klein, R. (2011) *Laser welding of plastics*. Wiley-VCH, Verlag GmbH & Co.
4. Briger, E.M., Moskvitin, G.V., Polyakov, A.N. (2012) Application of laser welding methods in modern industrial production. *Svarochn. Proizvodstvo*, **6**, 36–47 [in Russian].
5. Zvelto, O. (1990) *Principles of lasers*. Moscow, Mir [in Russian].
6. Greff, G. *Laser welding of plastics. New chemical technologies*. http://www.newchemistry.ru/letter.php?n_id=750
7. Kondilenko, I.I., Korotkov, P.A., Khizhnyak, A.I. (1984) *Physics of lasers*. Kiev, Vyshcha Shkola [in Russian].
8. *Plastics joining with high-power diode lasers*. http:www.limo.de/ru/limo-produ-kte/kundenreferenzen/kunststoffschweissen/
9. *Laser transmission (penetration) welding of thermoplastics*. BASF Aktiengesellschaft Company. Maintenance of thermoplastics. http://www.basf.ru/

Received 27.07.2020

https://doi.org/10.37434/tpwj2020.09.08

PROCESSES OCCURRING AT EXCITATION OF THE WELDING ARC (Review)

N.M. Makhlin
SC «REC Welding and Control in Nuclear Power of the E.O. Paton Electric Welding Institute»
11 Kazymyr Malevych Str., 03150, Kyiv, Ukraine. E-mail: electro@paton.kiev.ua

In view of the fact that a complete theory of the process of welding arc excitation, which could provide a convincing explanation of the entire totality of the known facts is absent so far, some important theoretical and experimental data of different authors are considered as regards the processes of initial excitation of the welding arc in arc and plasma welding which is important for designing electronic boosting devices, generating pulses of high and higher voltage that are injected into the interelectrode gap to ensure contactless initial and repeated excitations of the welding arc. Requirements to pulse parameters that are generated by these devices are given, which are obtained on the base of many investigations (including theoretical studies), experience in designing and application of boosting devices. Analytical expressions are proposed to create the theory of the process of DC welding arc excitation. 15 Ref.

Keywords: welding arc excitation in arc and plasma welding, glowing, spark and arc discharges, initial ignition voltage, repeated excitations of AC arc, combined devices - exciters-stabilizers, energy, amplitude, pulse duration

Contactless welding arc excitation is one of the most important stages in the welding cycle, which in most cases is carried out by a high-voltage breakdown of the interelectrode gap due to the use of a spark discharge. Despite a significant interest of researchers in the spark discharge, the theory of this process is still absent. According to the established concepts of modern electrophysics, the spark discharge (as a result of which excitation of the welding arc is carried out) refers to a nonindependent anomalous glowing discharge, which at the time of its completion should pass to a constant arc one [1, 2]. According to these concepts, temperature and gas pressure in the spark channel, the temperature of gas in this channel can reach 10000 K, which causes the probability of thermal ionization, and the phenomena that occur during a spark discharge, are explained in the theory of streamers (plasma channels threading from the anode to the cathode of the gas gap) [1]. As is noted in [1, 2], when an electric field is applied to a gas interelectrode gap, the charged particles present in this gap are accelerated by this electric field, and it should be noted that since the mass of ions significantly exceeds the mass of electrons, the main role in their interaction belongs to the electrons. If the electrons energy is sufficient for the gas ionization, a number of charged particles will increase, and in the direction from the cathode to the anode electron avalanches will move, leaving a positive spatial bulk charge and at the same time random electrons and the electrons formed in the gas during photoionization as a result of the radiation of atoms and molecules excited by electrons, will be drawn into the zone of spatial charge, creating new daughter avalanches on its way [1].

The first condition for the streamers formation is:

$$\frac{\alpha}{p}e^{\frac{\alpha}{p}pd} = 2{,}19\cdot 10^{8}\frac{E_{\mathrm{g}}}{p}\sqrt{\left(\frac{d}{pd}\right)}\cdot d, \qquad (1)$$

where α is the volume ionization coefficient, m^{-1}; ρ is the gas pressure, Pa; d is the distance between the electrodes, m; E_{g} is the intensity of electric field between the electrodes.

Using the expression (1), it is possible to find the value of the spark breakdown voltage U_{g} by the expression:

$$U_{\mathrm{g}} = E_{\mathrm{g}}d, \qquad (2)$$

However, the values, calculated by this expression coincide well with the experimental ones only in the cases when $pd \geq 250$ MPa, which is almost nonexistent in arc or plasma welding.

The second condition for the streamer formation is the formula

$$n_i \geq 7\cdot 10^{20}\ \mathrm{ion/m^2}, \qquad (3)$$

where n_{i} is the concentration of ions in the avalanche head.

For relatively short spark gaps (which is characteristic of arc and plasma welding), the condition (3) is always realized in case, if the condition (1) is realized.

The approximate theory of the spark discharge is usually based on Toepler's hypothesis, according to which the conductivity of the spark channel is proportional to the charge passed through the interelectrode gap:

$$G = k\int_0^t i\,dt, \qquad (4)$$

where G is the conductivity of the spark channel, Ohm^{-1}; k is the coefficient of proportionality, which depends on the composition, temperature and pressure of the gas

N.M. Makhlin — https://orcid.org/0000-0001-5235-6242

in the spark channel. Or the hypothesis of Weizel and Rompe, according to which all the energy released in the spark channel is spent to increase the internal energy of the plasma and is proportional to the conductivity of the spark channel and in this case [1]:

$$G = k\left(\int_0^t i^2 dt\right)^{1/2}. \qquad (5)$$

However, it should be noted that both mentioned hypotheses (4) and (5) describe the initial stage of the spark discharge process and do not take into account the decrease in the conductivity of the spark channel at the final stage of the process.

In turn, the hydrodynamic theory at a pulse energy, which is characteristic of spark ignition of the welding arc, leads to the following dependence of conductivity on the voltage at the interelectrode gap:

$$G = kCl^{-7/3}\left(U^2 - u^2\right)^{3/2} \times$$
$$\times\left[6U^4 \ln\frac{U}{u} - \frac{3}{2}\left(U^2 - u^2\right)\left(3U^2 - u^2\right)\right]^{-1/6}, \qquad (6)$$

where C is the capacitance directly connected to the spark gap, F; l is the length of the spark gap, m; U is the initial voltage on this gap, which is approximately equal to the breakdown voltage, V [1].

The longitudinal electric field strength in the spark, which precedes the formation of a constant arc discharge, characterized by relatively large values of current (up to 10^4 A) and current density at the cathode (up to 10^{10} A/m^2) at a relatively low arc voltage (from several units to tens of V), amounts to several kV/cm [1–4].

Thus, it was established [1–3, 5–7] that a streamer can be formed in a gas plasma, in which usually the chaotic movement of charged particles is dominated over their directional movement under the action of electric field or as a result of diffusion. Here the following equality should be realized

$$U = U_c + U_P + U_a, \qquad (7)$$

i.e., the streamer formation depends not only on the composition, temperature and pressure of the gas in the interelectrode gap, but also on the state and phenomena occurring in the near-electrode regions and the welding arc column.

The distribution of the electric potential along the length of the interelectrode gap is given in [1–6, 8, 9], and in [9] the phenomena at the anode and in the column of a multicurrent welding arc are analyzed in detail and comprehensively, and mathematical models based on the basis of this analysis, as a result of which the author assumes that the plasma potential of the arc column at the boundary with the anode layer is inhomogeneous, i.e. depends on the coordinate along the specified boundary. This causes the appearance of the component of the gradient of the electric potential and, accordingly, the components of the current density along the boundary of the anode layer, which largely determines the picture of the flow of electric current between the arc plasma and the anode.

To describe the plasma adjacent to the anode surface, the author of [9] conventionally divides the near-anode plasma into several zones. The first of them, which is directly adjacent to the anode surface, is the sheath, where the condition of the plasma quasineutrality is violated and a part of the potential drop between the plasma and the anode is formed. However, this can be neglected, taking into account that at a pressure close to the atmospheric one, and at the values of plasma temperature close to 1 eV, typical for arc or plasma welding conditions, the thickness of this layer is commensurable with the Debye radius, which amounts approximately to 10^{-8} m, which is significantly less than the free path lengths of the particles of the near-anode plasma, which range approximately from 10^{-7} to 10^{-4} m.

The second zone, the ionization layer or presheath, is a region of nonisothermal quasineutral multicomponent plasma, where charged particles are generated by ionizing plasma electrons of gas atoms desorbed from the anode surface and by the atoms of the anode metal which is evaporated. The ions formed in this zone, are accelerated in the direction of the anode surface by the electric field generated by more mobile electrons and recombine near this surface and thus, within the presheath, the conditions of a local ionization equilibrium are violated, i.e. the concentration of charged particles $n_e = n_i$ differ from the equilibrium concentration nSa, calculated using the Saha equations. In addition, here a noticeable drop in the potential of the near-anode plasma occurs, which can be much larger than its changes in the sheath.

According to the opinion of the author of [9], the outer boundary of the anode layer passes at a distance from the anode surface equal to several free path lengths of heavy plasma particles, beyond which the region of arc column begins, where a local thermodynamic equilibrium is established. In turn, the mentioned area can also be divided into two zones. The first of these zones is a layer of nonisothermal ionization equilibrium plasma, within which an equalization of the temperature of the electrons T_e and the temperature of the heavy particles T_h with the temperature in the arc column T occurs.

The other zone is actually an arc column (temperatures are measured in K). Moreover, the author of [9] assumes that the surface of the anode is flat and this fact allows him constructing a one-dimensional mathematical model of the anode layer of a high-current arc that burns in an inert gas medium of the atmospheric pressure. This statement is quite true if the welding current is $6 \cdot 10^2$ A or higher, but taking into account the fact that streamers formation occurs at very low currents and the breakdown voltage depends on the curvature of the electric field, the use of this statement is not possible. In [2] the author provides a generalized expression for the breakdown voltage U_{br} in most plasmatrons and torches for welding in an inert gas environment

$$U_{\text{br}} = \left(K'_{1\,\text{surf}} - K'_{2\,\text{surf}} \frac{p}{p_0}\right)\left[1 - k \cdot \lg \frac{f}{f_{\text{cr}}}\left(\frac{p}{p_0}\right)^{\frac{1}{3}}\right] \times$$
$$\times \left[1 + \left(\frac{\tau_0}{t_{\text{p}}} \cdot \frac{p_0 h_o}{ph}\right)^{\frac{1}{3}}\right] U_{\text{st}}, \tag{8}$$

where $K'_{1\,\text{surf}}$, $K'_{2\,\text{surf}}$ and k are the coefficients, which depend on the surface finish of the electrode of the plasmatron or torch in an inert gas medium: coefficient τ_0 is the duration of the discharge delay at p_0h_0 also depends on the surface finish of the electrode of the plasmatron or torch $\tau_0 = \tau'_0 K^{-1}_{2\,\text{surf}}$.

It should be noted that the coefficient $K^{-1}_{2\,\text{surf}}$ can also be determined experimentally because of the fact, that the expression (8) requires a lot of experimental welding operations and is not very suitable for engineering calculations. It should also be noted that the solution of the problem of electrical breakdown is possible by building a one-dimensional or multidimensional model. The advantages of the one-dimensional problem of electric breakdown consist in the fact that such a model makes it possible to analyze formulas and graphs, but at the same time it does not guarantee a complete coincidence with the results of experiments.

The experience and numerous experiments convincingly prove that the calculated and actual values of breakdown voltage coincide with (8) by at most 50 % and depend on a number of factors, and therefore, to provide contact-free initial excitation of the welding arc, the developers of pulsed welding oscillators or electronic high-voltage pulsed generators are forced to use devices that generate pulses with an amplitude from 4.0 to 10.0 kV. Since the theory of a multidimensional model of electric breakdown does not yet exist, it is possible to assume that this model is more applicable for the analysis of the phenomena associated with repeated excitations at alternating welding current. In the case of direct welding current, a one-dimensional model is more applicable.

According to a number of authors [1–6, 8–10], the main gas-dynamic process in a spark discharge channel is its expansion under the action of a shock wave, which allows accepting homogeneous model of this discharge with a dense shell and a discharge plasma considered as thermodynamically equilibrium, which is characterized by a temperature T. Moreover, the pressure in the channel can be considered constant, equal to the pressure of the unexcited gas. The author of [2] also states that, in any case, this nature of the shock wave has a maximum current.

In [2], it is shown that the influence of the initial conditions on the conductivity of the interelectrode gap at the end of the spark discharge process, as well as the inductance of the discharging circuit (which mainly affects the initial stage of the process), is insignificant. The process of development of the spark channel ends at the moment when the voltage on the interelectrode gap becomes equal to the open-circuit voltage of the welding current source.

The formation of a current-conducting spark channel provides a sudden increase in the conductivity of the interelectrode gap, and if the welding power source connected to this gap, has a sufficient power, the electric spark can turn into a long nonstationary arc discharge with its inherent cathode and anode spots.

Having performed a number of experimental works, G.I. Leskov and V.P. Lugin came to the conclusions important for the construction of pulse devices designed for the initial contactless excitation of welding arc [11]. These researchers proved that other conditions being equal, the material of welding electrodes, the composition of their coating and the gas flow rates usual for welding have almost no effect on the value of the breakdown voltage. Also, no noticeable effect of the direction frequency (in the range from 100 to 3000 Hz) and the shape of high-voltage pulses entering the interelectrode gap were detected. It was established that the main factors determining the value of the breakdown voltage (i.e. the streamer formation) are the gas composition in the interelectrode gap, the length of this gap and the degree of inhomogeneity of the electric field. Moreover, the main molecular-kinetic characteristic of gas, on which the value of the breakdown voltage depends, is the Ramsauer cross-section of atoms or gas molecules.

Analysis of the results of [11] and experimental works of other researchers allowed obtaining empirical expressions for determining the approximate averaged values of the electric breakdown voltage (U_{br}) in some gaseous media of technologically motivated interelectrode gaps [12]. Regarding the duration of the delay, which occurs when electric breakdown voltage is applied to the interelectrode gap, this duration is determined mainly by the time interval before the appearance of the first electron, which can cause avalanche formation (streamer formation), i.e. the statistical interval of time delay, which depends on the concentration of molecules in the gas volume of this interval and on the excess of the voltage value over the value of the voltage of the electric breakdown in a static field. In real welding installations, the delay time usually does not exceed a few microseconds and the volt-second characteristic, i.e. the dependence of the breakdown voltage on the pulse duration applied to the interelectrode gap, can be determined according to the data of Cooper or Ritz or with the use of Paschen curves. When a probability of electric breakdown is 50 % for the conditions that exist in arc and plasma welding, according to [1], the volt-second characteristic can be calculated with a large approximation by the expression

$$U_{\mathrm{br}} = \left(1 + \sqrt[3]{\frac{a}{t_{\mathrm{p}} pd}}\right) U_{\mathrm{br.st}}, \tag{9}$$

where α is a constant that depends on the type of gas in the interelectrode gap; t_{p} is the duration of the voltage pulse applied to the interelectrode gap C; $U_{\mathrm{br.st}}$ is the voltage of electric breakdown in a homogeneous static field, V.

If at a set value d (length of the interelectrode gap) the energy W_{p} of the voltage pulse applied to it is sufficient, then immediately after the electric breakdown of the gap, a spark discharge occurs, which, as established in VNIIESO [1], the initial stage of the spark discharge is accompanied by a significant increase in the conductivity of the interelectrode gap, and in the final stage of the spark discharge — by its drop [1, 2]. Depending on the conditions in the interelectrode gap and the properties of the welding power source connected to it, upon completion of the spark discharge, either complete attenuation of this discharge or the occurrence of a glowing or arc discharge is possible. The studies showed [1] that the arc in the interelectrode gap arises only in the case, when the resistance R_{c} of the conductive channel formed by the spark discharge is less than some threshold value R_{thr}, which depends on the current input rate of the welding power source in the channel, the arc time constant, the voltage in the interval $u(t)$ and other factors. For a DC welding arc, the approximate value R_{thr} can be determined by the expression:

$$R_{\mathrm{thr}} \approx \left(\frac{n\theta \left.\frac{di}{dt}\right|_{t=0} U_{\mathrm{o.\text{-}c}}^{\frac{n+3}{n-1}} a^{\frac{n+1}{n-1}}}{2 + n\theta \left.\frac{di}{dt}\right|_{t=0} U_{\mathrm{o.\text{-}c}}^{\frac{n+1}{n-1}} a^{\frac{n}{n-1}}} \right)^{n}, \tag{10}$$

where n is the value of the approximation degree; θ is the arc time constant, s; di/dt is the rate of increase in the arc supply current at the initial moment (at $t = 0$), A/s; $U_{\mathrm{o.\text{-}c}} = u(0)$ is the open-circuit voltage of the welding power source, V.

Fulfilment of the condition $R_{\mathrm{c}} < R_{\mathrm{thr}}$ depends not only on the level of U_{thr}, but also on the level of power of the voltage pulses, which cause a spark discharge in the interelectrode gap. Since the duration of these pulses is determined by the reactive parameters and the quality factor of the forming circuits of the generators of overvoltage pulses (GVP) of the boosting devices and the power source circuits of the arc, it is much more convenient to operate with such a parameter of pulses as their energy W_{p} (in J). Also, since in the vast majority of cases during the formation of pulses produced by GVP, the energy of preliminary charged capacitive storages is consumed, it can be assumed that $W_{\mathrm{p}} = CU_{\mathrm{c}}^2/2$, where C is the capacitance of the capacitor (capacitors), F; U_{c} is the constant charge voltage of the capacitance, V. In [12] the values of W_{p} are given, which are recommended for different gaseous media and technologically motivated interelectrode gaps and obtained experimentally and confirmed by the experience in designing and application of electronic boosting devices.

The streamers formation also depends on the cathode phenomena [1, 4, 8], but it should be noted that their theory is not fully developed, as well as the theory of the AC arc excitation.

Because of a high mobility of electrons, an uncompensated bulk charge is formed near the cathode, due to which a cathode drop of the U_{c} potential exists. Moreover, near the cathode, there is an area of transition from the arc column to the narrowed area — such that is subjected to contraction — cathode region [1]. Here the electric field strength is much higher than in the arc column. In the area of the cathode potential drop, electrons and positive ions undergo acceleration, due to which electrons can carry out shock ionization, and ions can carry a much larger fraction of current as compared to the column plasma [1].

The energy obtained by the cathode from ions that bring their neutralization energy and kinetic energy of movement and which comes from the plasma of the column (due to thermal conductivity and radiation), is spent on compensating the electron output, thermal conductivity and cathode radiation, on its melting and evaporation and on the dissociation of molecular gases [1, 4, 8]. The share of all these components is different and depends on the conditions in which the arc burns. Among these conditions, the main role belongs to the cathode material [1]. There are two types of cathodes: «non-fusible» or hot cathodes of tungsten or carbon, and «fusible» or cold electrodes of low-melting materials. On refractory cathodes, which are mainly used in arc and plasma welding, a stationary spot is formed, which radiates quite strongly. At the same time with an increase in temperature of the cathode to some critical value, the spot by a jump disappears, and narrowing of the column near the cathode is absent [1].

The volt-ampere dependence of the near-cathode region of the arc column at low currents is falling [1, 2, 4, 8, 9].

The temperature of the cathode is close to the melting point of the welded metal, and the current densities per cathode, which are measured by the spot area, range from 10^9 A/m^2 in the arcs with a spot to 10^7 A/m^2 in the arcs without a spot A/m^2. Since the theory that explains all the factual material regarding cathode phenomena is still absent, the theory of thermoelectron arc, according to which the current from the cathode is provided by thermoelectrons and ions.

The density of thermoelectric current is determined by the Richardson–Dushman formula or by the formula, that takes into account the distortion of the potential barrier. The energy required to create thermoelectrons is supplied to the cathode by ions, and in this case the fraction of ionic current J_p is

$$\frac{J_p}{J} = \frac{U_{out}}{U_c + U_{neut}}. \qquad (11)$$

For different conditions, this value ranges from 0.15 to 0.35, and at lower values of the fraction of ionic current, in order to explain the required heating of the cathode, the heat transfer from the plasma should be taken into account [1].

It should be noted that thermoelectronic theory is not able to explain the phenomena at the cathode of low-melting materials, because in this case to form a spatial charge the current density at the cathode should be at least 10^{11} A/m^2. Taking into account the presence of thermoelectrons, this value decreases to the actual value of 10^9 A/m^2. According to the autoelectronic theory $J_p << i_e$, the current is transferred by electrons, which carry out step ionization in the zone of a cathode potential drop.

When calculating the autoelectronic current density, in addition to taking into account the presence of a dielectric film on the cathode surface, the presence of microroughnesses on its surface should also be taken into account, due to which the effective field strength can be several times increased [1]. But, despite these specifications, the autoelectronic theory is also not able to explain the whole set of processes at the cold cathode.

As far as for arc and plasma welding, alternating current mainly of industrial frequency and the frequencies close to it is used (from 50 to 400 Hz), there is every reason to believe that the condition $R_c < R_{thr}$ is valid in the case of alternating current, here R_{thr} is also determined by the expression (10), which determines the requirements characteristic of alternating current until the start of the generation of pulses, exciting the welding arc.

The excitation of the arc discharge largely depends on the value of the voltage applied to the interelectrode gap. Therefore, the pulse that excites the welding arc should begin to be injected into the interelectrode gap near the maximum of this voltage (near the amplitude of the open-circuit voltage of the welding source). Numerous investigations found that in the sinusoidal waveform arc current, the phase of the beginning of generating the pulse, exciting the arc, should be (75–80) electr. deg. relative to the zero phase of the open-circuit voltage of the welding power source, while the condition of a sufficiently high rate of increase in the arc discharge current should be met. The highest efficiency of the initial excitation of the AC arc is achieved when the phase of the beginning of the generation of the pulse exciting the welding arc coincides with the moment of transition of the constant welding current of the arc through the zero value. In addition, electrophysical conditions of emission from the electrodes are important for contactless initial excitation of the arc, which can be very different for the AC arc depending on the electrode material and the fact, whether the electrode is an anode or cathode at the moment of the initial arc excitation. This is especially characteristic of TIG welding of aluminium and its alloys, in which the initial excitation of the arc almost always occurs during the time intervals, when the cathode is a product to be welded. It seems that this can be explained by the fact, that during excitation of the welding arc, nonconsumable (tungsten) electrode is characterized by thermoemission, the formation of which is associated with the need of heating the electrode to the emission temperature, and this process is inertial. At the same time, at a cathode formation on a welded product of aluminium and its alloys (especially if the outer surface of a product is covered with an oxide film Al_2O_3) an almost noninertial autoelectron emission occurs [1, 2, 10, 13].

The problems of stability of the AC welding arc attracted attention over the past century and continue to attract the attention of researchers and specialists in the field of electrical technologies and in the field of electrical engineering. As a result of many years of extensive theoretical and experimental investigations, generalized, for example, in [1, 9–15], a considerable experience has been accumulated, which allows explaining a number of phenomena and features of the AC arc, as well as formulating the main conditions of constancy of the arc discharge, including application of analytical methods.

The AC welding arc periodically changes its polarity and, as a result, the same electrode alternately is either the cathode or the anode. The change in the polarity of the electrodes causes changes in the intensity and direction of gas flows in the arc and reorientation of charged particles in its column. It was established that the processes in the arc column have a decisive influence on the behaviour of the welding arc and its characteristics during almost the entire duration of each half-cycle of alternating current, except for short intervals near the current transition through zero, during which the arc discharge is absent and at best, it is glowing in the residual plasma [1, 5, 7, 9, 10, 12–15].

The presence of pauses in the existence of the arc discharge in the interelectrode gap near the current transition through the zero value is the main characteristic feature of the AC welding arc, at the end of each half-period of which before and after the arc discharge attenuation, the gas temperature in the arc decreases significantly and accordingly, the conductivity of the interelectrode gap is significantly reduced and at the same time the temperature of the anode and cathode spots drops [1, 9, 10, 12–14].

This and other features of the AC welding arc are considered in detail in the works [1, 4, 10, 12].

Conclusions

1. For better explanation of the whole set of processes associated with the initial and repeated excitations of the welding arc, including alternating current arc, as well as to develop engineering procedures for calculating the combined devices-exciters-stabilizers, the further theoretical and experimental investigations, especially in the direction of studying near-cathode phenomena are required.

2. As a result of consideration and generalization of features of contactless initial and repeated excitations of welding arc performed on the basis of the use of the known literary sources, theoretical and experimental works of different authors and available experience of development and application of means of realization of these processes, it was established that in the mode of initial excitation (ignition) of the arc depending on the conditions in the interelectrode gap (its length, type and pressure of gas in it, the shape and purity of the working end of the welding electrode and a product to be welded, the basic parameters of the output high-voltage pulses, which are generated by the combined exciters-stabilizers, should have the following values: pulse energy — from 0.01 to 0.50 J, pulse amplitude — from 3.5 to 10.0 kV, duration (at the level of 0.05 of amplitude value) — from 3 to 20 μs.

It was also established that in the mode of stabilization of the AC welding arc (i.e. at repeated excitations) depending on the degree of deionization and the associated decrease in the conductivity of the interelectrode gap at each change in the polarity of the arc current, the basic parameters of the output high-voltage pulses generated by combined exciters-stabilizers, should be: pulse energy — from 0.2 to 1.0 J, pulse amplitude — from 400 to 950 V, duration (at the level of 0.05 amplitude value) — from 50 to 100 μs, and in some cases (for example, during welding with a fusible electrode in the CO_2 environment) — from 0.2 to 1.0 ms.

3. To solve the problem of determining the required parameters of the pulses of the initial and repeated excitations of the welding arc, both one-dimensional as well as multidimensional models can be used (however, the theory of a multidimensional model still does not exist). To solve the problem of determining the optimal parameters of the pulses of the initial excitation of the DC arc, one-dimensional model is the most applicable and common, which provides the ability to analyze formulas and graphs, but does not guarantee a complete coincidence with the experiments. When solving the problems of repeated excitations of the AC welding arc, multidimensional model can also find applicability (despite the absence of a complete theory). In this case, it becomes necessary to introduce a correction coefficient K_C for each parameter, which is equal to the ratio at each point of the experimental value. In the future, everything depends on the results of the obtained experimental correction curves.

4. Creation of combined exciters-stabilizers is possible only under the condition if their construction involves a series connection of the output circuits of these devices in the circuit of the welding or auxiliary (pilot) arc.

1. (1986) *Equipment for arc welding*: Refer. Book. Ed. by V.V. Smirnov. Leningrad, Energoatomizdat [in Russian].
2. Temkin, B.Ya. (1981) *Theory and calculation of welding arc exciters*: Syn. of Thesis for Cand. of Tech. Sci. Degree. Leningrad [in Russian].
3. Rajzer, Yu.P. (1987) *Physics of gas discharge*. Moscow, Nauka [in Russian].
4. Gvozdetsky, V.S. (1969) To the theory of cathode processes in electric arc. *Avtomatich. Svarka*, **1** (Pt 1), 33–37; **6**, (Pt 2), 1–4 [in Russian].
5. (1980) *Electrotechnical reference book*. In: 3 Vol., Vol. 1: General problems. Electrotechnical materials. Ed. by V.G. Gerasimov, P.G. Grudinsky, L.A. Zhukova, et al. 6st Ed. Moscow, Energiya [in Russian].
6. Paton, B.E., Zaruba, I.I., Dymenko, V.V., Shatan, A.F. (2007) *Welding power sources with pulsed stabilization of arc burning*. Kiev, Ekotekhnologiya [in Russian].
7. Farson, D., Courardy, C., Talkington, J.et al. (1998) Arc initiation in gas metal arc welding. *Welding Res. Supl.*, **8**, 315–321.
8. Kesaev, I.G. (1968) *Cathode processes in welding arcs*. Moscow, Nauka [in Russian].
9. Krivtsun, I.V. (2018) Anode processes in welding arcs. *The Paton Welding J.*, **11–12**, 91–104.
10. Leskov, G.I. (1970) *Electric welding arc*. Moscow, Mashinostroenie [in Russian].
11. Leskov, G.I., Lugin, V.P. (1971) Investigation of voltage breakdown of gaps between welding electrodes. *Svarochn. Proizvodstvo*, **2**, 10–11 [in Russian].
12. Makhlin, N.M. (2015) Peculiarities of contactless ignitions of alternating current arc. *The Paton Welding J.*, **10**, 29–35.
13. Weinshehk, H.E., Schellhase, M. (1971) Wiederzundugscharacteristiken von Schweißlichtbogen mit abschmelzen der Elektrode. *ZIS-Mitt.*, 13**(12)**, 1706–1720.
14. Korotynskyi, O.E. (2007) *High-efficient power sources for arc welding on the base of inductive-capacitive transducers*: Syn. of Thesis for Dr. of Tech. Sci. Degree. Kyiv [in Ukrainian].
15. Pokhodnya, I.K. (1967) *Electrode melting and interaction of metal with gases in arc welding*: Syn. of Thesis for Dr. of Tech. Sci. Degree. Kiev [in Russian].

Received 10.08.2020